

# Contents

<b>1</b>	<b>Introduction</b>	<b>11</b>
1.1	Crystal growth	11
1.2	Surface and interface structure	12
1.3	Impurities in crystal growth	14
1.3.1	Habit modification	14
1.3.2	Surfactants	15
1.4	Methods	16
1.4.1	Crystal growth techniques	16
1.4.2	Surface X-ray diffraction	17
<b>2</b>	<b>Surface atomic structure of the <math>(\sqrt{3} \times \sqrt{3})R30^\circ</math>-Sb reconstructions of Ag(111) and Cu(111)</b>	<b>21</b>
2.1	Introduction	21
2.2	Experimental	23
2.3	Results	26
2.3.1	Ag(111) $(\sqrt{3} \times \sqrt{3})R30^\circ$ -Sb	26
2.3.2	Cu(111) $(\sqrt{3} \times \sqrt{3})R30^\circ$ -Sb	32
2.4	Discussion	35
<b>3</b>	<b>Floating stacking fault during homoepitaxial growth of Ag(111)</b>	<b>39</b>
3.1	Introduction	39
3.2	Experimental	40
3.3	Results	41
3.4	Discussion and Conclusions	45
<b>4</b>	<b>Phase transition of a Pb monolayer on Ge(111)</b>	<b>47</b>
4.1	Introduction	47
4.2	Experimental	50
4.3	Results and discussion	51
4.3.1	Saturation coverage of the $\beta$ phase	51
4.3.2	Atomic structure of the $\beta$ phase	53
4.3.3	$1 \times 1$ phase: a two-dimensional solid or liquid?	57

4.4	Conclusions	63
<b>5</b>	<b>Surface atomic structure of KDP crystals in aqueous solution: an explanation of the growth shape</b>	<b>65</b>
5.1	Introduction	65
5.2	KDP	66
5.3	Experimental	68
5.4	Results	69
5.5	Discussion and Conclusions	70
<b>6</b>	<b>X-ray diffraction studies of KDP crystal surfaces</b>	<b>73</b>
6.1	Introduction	73
6.2	Experimental	75
6.3	In situ set up	77
6.4	Ex situ results	82
6.5	In situ results	84
6.5.1	Atomic structure in equilibrium	84
6.5.2	Specular reflectivity	87
6.5.3	Impurities and growth	89
6.6	Conclusions	92
	<b>References</b>	<b>95</b>
	<b>Summary</b>	<b>107</b>
	<b>Samenvatting</b>	<b>109</b>
	<b>Dank</b>	<b>115</b>
	<b>Curriculum Vitae</b>	<b>117</b>



# I

## Introduction

### 1.1 Crystal growth

Crystals have intrigued mankind since ancient times. The main applications of crystals till the 19th century were as precious stones in jewellery, in medical prescriptions and in mysticism because of the belief in special virtues of gemstones — a superstition still existing in modern times. Only in the 17th-18th centuries, when the principle laws governing crystal habits were found, crystallography became an independent branch of science. First it was connected with mineralogy, whose most perfect objects of investigation were crystals. Later it became more associated with chemistry, because it was apparent that the habit depends directly on the composition of crystals and can only be explained on the basis of atomic-molecular concepts. In the 20th century crystallography became more oriented towards physics, and an increasing number of new optical, electrical, mechanical and magnetic phenomena inherent to crystals were found. Mathematical methods began to be used, particularly the theory of symmetry, which achieved its completion in the classical space-group theory at the end of the 19th century. The discovery of X-ray diffraction by crystals early this century, caused a complete change in crystallography and in the whole science of the atomic structure of matter.

Single crystals, epitaxial layers, and multilayer structures have become the basis for research in solid-state sciences and for numerous modern technologies. Crystallization and crystal growth are important for the purification, separation and definition of solid compounds. Mass crystallization for magnetic media, for luminescent powders, catalysts, inorganic and organic pigment dyes, and for such commonplace products as salt and sugar is still continuously perfected. The preparation of large, defect free, single crystals of, e.g., silicon has been the prerequisite for its exploitation in semiconductor device technology.

A crystalline solid is defined as an ordered array of entities (atoms, ions, molecules etc.) where the degree of ordering proceeds in three dimensions. If this three-dimensional order extends to the full macroscopic dimensions of the material

## CHAPTER I

we have a single crystal. If this is not the case, we have polycrystalline material. A crystal growth system consists of at least a mother phase, be it gas, liquid, or solid, a crystalline phase and an interface separating the two phases. The potential barrier that a system must overcome to create a crystalline nucleus in an ideally homogeneous mother phase and which determines the rate of nucleation is defined by the interface energy and the supersaturation.

Atomic structure models form one extreme in the description of the growth of crystals. Since crystal growth is a highly collective process, atomic scale properties are decisive for the macroscopic morphology of crystals. The other extreme is the macroscopic description in terms of statistical thermodynamics and transport theories. Crystal growth and decrystallization (evaporation, melting, dissolution, etching etc.) take place under the influence of a thermodynamic driving force determined by deviations in temperature, pressure and concentration. This thesis is concerned with the first description. By determining the atomic structure of the interface we try to understand the kinetic and thermodynamic processes involved in growth. An important theme in this thesis is the influence of impurities on the growth mechanism and morphology of the crystals.

Although most crystals are grown from the liquid phase, the atomic structure of the growing interface is hardly studied because of a lack of suitable techniques. For crystal growth from the vapour phase this is different. The first part of this thesis is concerned with crystals and their growth in an ultra-high vacuum (UHV) environment, where the conditions of the surface can be controlled very well. In chapter 4 we study a model solid-liquid interface, where a two-dimensional liquid is in contact with a crystalline substrate. In the last two chapters of this thesis we describe experiments on crystal surfaces in their growth solution. From the atomic structure of the crystal interface, we are able to make the connection to the macroscopic growth morphology found for these crystals.

### **1.2 Surface and interface structure**

For many applications the shape of crystals is very important. For example, in industrial mass crystallization the crystal morphology determines the properties of the filtration process needed to separate the crystals from the mother phase from which they have been grown. In metallurgy the mechanical properties of solidified metals are strongly influenced by the size and morphology of the grains which form the polycrystalline solid. At equilibrium, the crystal shape is determined by the dependence of the surface free energy on the orientation of the surface with respect to the crystal lattice. Recent results in crystal growth from solution start to bring the role of the interface structure into the picture and it is clear that modifications

## INTRODUCTION

are needed in the equilibrium theory to describe the growth form [1]. The quality of crystals is to a large extent determined by the surface structure and dynamics during growth. Growth of many crystals is poorly understood due to complications introduced by the presence of impurities, defects, surface reconstructions or an adsorption layer that can strongly modify the crystal morphology.

Physical surface properties can be quite different from macroscopic crystal properties. In the past decades surface scientists have studied the atomic geometry and morphology of surfaces in order to gain an understanding of their physical, chemical and electronic properties. The surfaces studied are usually “free”, i.e. in a UHV environment. Over the years a variety of techniques, such as ion scattering, low-energy electron diffraction, X-ray diffraction and scanning tunneling microscopy have been developed to investigate surface structures, surface roughening and melting, and thin films.

The abrupt change caused by terminating the solid at a surface will often result in new equilibrium positions for the surface atoms, because of the absence of the bonding force of nearest neighbours on the vacuum side of the atoms. On many surfaces the structural rearrangement of the atoms results in an ordered periodic structure with a different symmetry than the bulk. This phenomenon is called reconstruction. New reconstructed unit cells are formed, the size of each cell being a multiple ( $n \times m$ ) of that of a bulk unit cell. In practice, reconstructions are periodic only over a finite length. There will be translational and rotational domains, separated by defects such as steps and domain walls. In chapters 2 and 4 of this thesis the determination of the atomic structure of a reconstruction is presented, involving the adsorption of a (sub)monolayer of a different species.

Surfaces in contact with another medium are much less studied. In particular the interface between solid and liquid has received little attention, largely for lack of a structure probe by which the interface can be accessed. Most surface science techniques need a UHV environment and cannot be applied to surfaces in a fluid. An important exception to this is surface X-ray diffraction, the technique used for the experiments described in this thesis. Solid-liquid interfaces are omnipresent in nature and technology, not only in crystal growth from melts and solutions, but also in melting and freezing phenomena and electrolytic cells, for example.

Whereas many liquids can be undercooled quite easily below the thermodynamic freezing transition, the superheating of solids is very difficult to achieve. The idea that a solid may have a thin layer of liquid at its surface was already proposed by Faraday who suggested that the slippery nature of ice arises from an outer layer of surface water. The prevention of superheating of solids by surface melting has been found first for a (110) surface of Pb [2]. Surface melting has thereafter been observed for a broad range of crystal faces with the aid of vari-

ous experimental techniques [3]. An interesting point is whether the converse of surface-induced melting also exists: surface-induced freezing (or crystallization). When a liquid is in contact with a single-crystal solid at temperatures near the bulk freezing point, will the interface act as a nucleation site for solidification of the bulk liquid? Density-functional theories indicate that in the interface region a liquid is strongly modulated by the solid and that the order decays rapidly away from the solid-liquid interface [4]. The liquid, on the other hand, will also influence the structure of the solid surface. A surface that is reconstructed in vacuum, may obtain a different structure when covered by a liquid. It is therefore interesting to investigate *both* sides of the solid-liquid interface.

The growth front in liquid phase epitaxy (see section 1.4.1 below), where a liquid metal is in contact with a semiconductor surface, is a solid-liquid interface. As a model system we have studied in chapter 4 a monolayer of Pb on Ge(111) close to the bulk melting point of Pb. For any overlayer-substrate system one may ask the question whether the two-dimensional overlayer displays liquid-like properties or “feels” the presence of the substrate strongly enough to order along the substrate lattice. For Pb on Ge(111) a phase transition occurs in which a  $(\sqrt{3} \times \sqrt{3})R30^\circ$  reconstruction disappears. We have confirmed that the Pb layer gives rise to a ring of diffuse X-ray scattering indicative of a two-dimensional liquid. However, we also found that the Pb atoms are still laterally ordered by the underlying Ge substrate potential.

For the system of a Ga droplet on diamond(111), Huisman *et al.* found evidence for a layerwise ordering of the liquid metal against the hard diamond surface [5]. In the case of Pb on Ge(111) we also tried to study the growth at a substrate temperature where bulk Pb is melted. However, in this case the Pb desorbs rapidly when more than one monolayer is deposited. The first layer has a certain amount of order induced by the solid substrate, but whether this order decreases or increases with thicker layers remains unsolved. For (sub)monolayer Ga coverages on diamond(111) no evidence is found for ordering of the adatoms. Ga forms three-dimensional clusters in coexistence with a two-dimensional gas of adatoms [6].

### 1.3 Impurities in crystal growth

#### 1.3.1 Habit modification

Crystal growth strongly depends on active impurities present in a crystallizing system, even in amounts which do not influence the properties of the bulk. On the other hand, many of these properties depend on the amount of impurities or point defects in the grown crystal. Thus the manner in which impurities are trapped by

## INTRODUCTION

growing crystals is one of the most important characteristics of growth technology.

The fact that adsorbates produce certain growth characteristics of crystals grown from liquid solutions has been known for a long time (see for example [7] and references therein). Romé de Lisle found already in 1783 that common salt forms octahedra instead of cubes when grown from brines containing urea [8]. The reason for this modification is still not established. Probably the urea, which is a highly polar molecule, affects the surface free energies of the different surface planes [9]. Since the discovery of Romé de Lisle, the effect of trace additives on the growth of crystals from solution has been studied quite extensively and it is known that the growth can be influenced in desirable and *undesirable* ways by impurities.

The presence of impurities effects the growth kinetics, composition and morphology of the growing crystal. Only in simple and extremely pure systems most surface steps are monomolecular and straight or at most smoothly curved. Adsorption of impurities immediately leads to irregular macrosteps. A low concentration of immobile impurities blocks the advancement of steps at low supersaturations, leading to a “dead supersaturation zone” where no growth occurs [10]. Below a critical supersaturation the advancement of steps is completely stopped. Above this critical supersaturation the step velocity increases with supersaturation. Impurities also affect the anisotropy in step velocities, and thus the shape of growth spirals. Reversely, step growth strongly affects the incorporation of impurities.

Most of what is known about crystal growth from solution has been discovered by optical microscopy. Hardly any atomic-scale experimental data exist, but X-ray diffraction using the latest synchrotron radiation facilities allows such data to be collected for the first time. In the last two chapters of this thesis we therefore describe X-ray diffraction measurements on the inorganic crystal KDP ( $\text{KH}_2\text{PO}_4$ ). It is known that when impurities are present, the crystal habit is elongated in the direction of one of the two natural existing faces. From the atomic structure that we determined of these faces in solution, an explanation can be given for the influence of the impurities on the macroscopic growth morphology of the crystals.

### 1.3.2 *Surfactants*

In recent years numerous experiments have been done to examine whether in the epitaxial growth of semiconductors and metals under UHV conditions analogous effects to produce desirable growth characteristics can be found [11]. In homoepitaxial growth of Ag(111) it was shown that by adding a “surfactant” the growth mode can be changed from three-dimensional to layer-by-layer [12]. The literal meaning of surfactant is “surface-active agent”, and in crystal growth the name surfactant is used for additives which are present at the surface and affect the growth



mode. This can occur by decreasing the surface energy, thereby increasing the wetting properties [13], or by changing the kinetics of the growth. The surfactant has to float very efficiently to the surface during growth to remain active. For Ag(111) Sb is found to have this property. In chapter 2 of this thesis the surface atomic structure determination of the  $(\sqrt{3} \times \sqrt{3})R30^\circ$ -Sb reconstructions of 1/3 monolayer Sb on Ag(111) and Cu(111) is presented. The Ag(111) $(\sqrt{3} \times \sqrt{3})R30^\circ$ -Sb reconstruction plays an important role in the formation of stacking faults during homoepitaxial Ag growth. This is described in chapter 3.

Also in heteroepitaxial growth we have started to investigate whether layer-by-layer growth can be promoted by surfactants for the case of Ag/Fe(100) multilayers. Magnetic multilayers, consisting of many alternating metal layers with a thickness of only a few interatomic distances, display interesting and useful magnetic properties like a large perpendicular magnetic anisotropy and a giant magneto-resistance. These layers can be used for magnetic recording media. The desired properties of these magnetic multilayers are dependent on the smoothness, the sharpness, and the structure of the interfaces. Often it is not possible to go to high substrate temperatures to achieve smooth layers because of interdiffusion of the deposit into the substrate.

When Fe is deposited on Ag(100) initially three-dimensional islands grow. From our experimental results it appears that the Fe exchanges with the Ag to produce a structure that is intermixed in the top few layers. The driving force for this exchange is the much lower free energy of Ag. Both the surface-free-energy balance and the presence of strain energy (because of the lattice mismatch between Fe and Ag) can explain why three-dimensional islands lower the total free energy. A surfactant can thus be expected to change this behaviour, but our preliminary results do not show any evidence for an effect of predepositing a surfactant like Sb or Pb for the Fe/Ag(100) system.

## 1.4 Methods

### 1.4.1 Crystal growth techniques

The growth of crystals having a relevant size proceeds in nearly all cases from a fluid phase. Compared with liquids (melts, aqueous and other solutions) the species have the highest mobility in the gas, but their volume concentrations are low. Under certain circumstances, crystals can be grown at considerable lower temperatures from a gas phase than from a melt, thus allowing crystallization of compounds with restricted high temperature stability.

Crystals are often grown from solution by the temperature decrease method. Seed crystals are rotated in a stirred and temperature-stabilized saturated solution.

## INTRODUCTION

By lowering the temperature a supersaturation is created and the crystals start to grow. Another early and simple growth technique is liquid phase epitaxy (LPE) [14] that combines solution growth and epitaxy. LPE is the deposition from a liquid solution of epitaxial layers on a crystalline substrate that may consist of some of the elements that exist in the liquid phase. An example is the heteroepitaxy of SiGe on Si substrates from solutions consisting of a solvent like Bi, In, or Sn [15]. The Pb/Ge(111) system described in chapter 4 serves as a model for such growth environments.

In addition to growth techniques from solution or melt, there are several vapour growth techniques of which chemical vapour deposition and metalorganic vapour phase epitaxy are the most important. These vapour growth techniques take place at pressures between 20 mbar and atmospheric pressure. An ultra-high vacuum vapour growth technique is molecular beam epitaxy (MBE). During MBE elemental source materials are heated in effusion cells and evaporated. The atomic thermal beams are directed towards the substrate, where they adsorb at the surface. Each source is provided with an individual shutter, which permits rapid changing of the beam species. Since the shutter operation is faster than the time needed for the growth of one monolayer, atomically abrupt interfaces can be realized. Very high purity layers can be obtained in this way. The ultra-high vacuum conditions are also advantageous for *in situ* monitoring techniques such as reflection high-energy electron diffraction and X-ray diffraction. MBE is used in the experiments described in chapters 2-4.

### 1.4.2 Surface X-ray diffraction

The wavelength of X-rays ( $\sim 0.5\text{-}10 \text{ \AA}$ ) closely matches the length scales typical for interatomic distances in solid materials. X-radiation is therefore an optimal characterization technique capable of examining the structure of crystalline materials on an atomic length scale. X-rays are non-destructive and enable crystal growth processes to be examined *in situ* [16]. X-ray diffraction has been used for many years to study the structural properties of bulk crystalline and amorphous materials on an atomic scale. Since the last 15 years X-ray diffraction is widely applied to the study of surfaces (for reviews see [17–20]). This is very much stimulated by the availability of synchrotron radiation sources, which provide more intense beams than those generated by conventional rotating anode sources. This high intensity is needed because of the low scattering cross-section of X-rays; the scattered intensity from a surface is some five orders of magnitude less than that from a bulk crystal. Because of this low cross-section, single scattering (kinematical) theory is applicable, which makes data interpretation straightforward.

## CHAPTER I

Surface sensitivity is obtained by avoiding the bulk Bragg peaks that are located at points in reciprocal space (denoted by integer values  $(hkl)$  of the Miller indices). The two-dimensional nature of an interface gives rise to rods of diffracted intensity which contain surface sensitive information. These are the so-called crystal truncation rods (CTRs) [21, 22], arising from the termination of the crystal at the interface and that are denoted by integer values of  $(hk)$ . The intensity along a CTR is given by the interference sum of the substrate and the surface layer. In addition, a reconstructed surface or an overlayer with periodicity different from the bulk gives rise to diffracted intensity for fractional values for  $h$  and  $k$  that are forbidden for the bulk crystal, and therefore originate solely from the surface. Another way of becoming surface sensitive is to measure at glancing angles, thereby limiting the penetration depth of the X-rays.

X-ray diffraction is a powerful tool to investigate epitaxial crystal growth *in situ*. Sensitivity to the growth mode and surface roughness evolution is obtained by observing the diffracted intensity at so-called anti-Bragg positions in reciprocal space. These are reflections where the scattered intensity from an island is out-of-phase with that scattered from a terrace. An equivalent way of saying this is that these reflections are on positions on the CTR that are exactly in-between two bulk Bragg peaks. One particular important quality of X-ray diffraction is that one can select the type of features one is sensitive to, by choosing an appropriate position in reciprocal space. In the specular beam, one is only sensitive to the structure perpendicular to the surface, while anti-Bragg positions on other CTRs will in addition yield information of the in-plane crystalline quality. In chapters 2 and 3 we show that by an appropriate choice of reflection we become sensitive to the formation of stacking faults and the concomitant formation of twin crystallites.

In an X-ray scattering experiment scans are made in reciprocal space by rotating the crystal and/or the detector. The integrated intensities of scans through diffraction peaks yield the so-called structure factors, which are the quantities needed to deduce the structure at the interface. The basic structure factor calculations and geometrical corrections needed for the measured integrated intensities are given in chapter 2.

The experimental method for studying solid-liquid interfaces is similar to the way surfaces in vacuum are investigated. Because of the large penetration depth of X-rays in matter, the technique of X-ray diffraction can be applied to studies of buried interfaces. To minimize the attenuation of the X-rays in the liquid, a high flux of high-energy photons is needed and therefore these experiments are best performed using undulator radiation from a third-generation synchrotron source like the European Synchrotron Radiation Facility (ESRF) in Grenoble. The overruling difficulty in these studies is the increase in background due to

## INTRODUCTION

the scattering from the liquid, which can easily drown the weak signal from the interface region. Because of the high energy used also a macroscopic part of the bulk crystal will be illuminated which gives rise to a substantial background of undesirable bulk Compton and thermal diffuse scattering. The background level, and especially the signal-to-background ratio, ultimately determines the feasibility of these studies. In the last chapters of this thesis we show that X-ray diffraction can now successfully be applied to the study of crystal surfaces in their growth solution.



## II

### Surface atomic structure of the $(\sqrt{3} \times \sqrt{3})R30^\circ$ -Sb reconstructions of Ag(111) and Cu(111)

*We present an X-ray diffraction structure analysis of the  $(\sqrt{3} \times \sqrt{3})R30^\circ$  reconstructions of Ag(111)-Sb and Cu(111)-Sb surfaces. We find these structures to be very similar. Contrary to previous reports we find that all top layer atoms reside at stacking fault positions. Each  $(\sqrt{3} \times \sqrt{3})R30^\circ$  surface unit cell contains one substitutional Sb atom. We determined the out-of-plane relaxations of the top layer atoms and the in-plane distortions in the second layer. For coverages below 1/3 monolayer, the Sb atoms are embedded randomly at fcc positions in the top surface layer.*

#### 2.1 Introduction

Interest in homoepitaxial metal growth has increased enormously in recent years. Egelhoff and Jacob [23] showed that metal layers can grow layer-by-layer at unexpectedly low temperatures. Another interesting observation was made by Kunkel *et al.* [24], who discovered re-entrant layer-by-layer growth at low temperatures in the growth of Pt on Pt(111). Van der Vegt *et al.* [12] were the first to show that surfactants can be used to induce layer-by-layer metal growth.

In homoepitaxy, simple kinetic processes influencing epitaxial growth can be studied without complicating effects such as lattice mismatch or differences in surface energy. It has been known for some time that epitaxial growth of metals can be influenced by a variety of adsorbed gases [9, 25–27], but only recently has it been shown that for a number of metals smooth homoepitaxial growth can be stimulated by using surfactants like Sb, O<sub>2</sub> and In [12, 28–30]. Understanding the origin of the various phenomena occurring in homoepitaxy is important for deriving conclusions applicable to the more complex heteroepitaxial systems, like metallic multilayers, which are interesting as magnetic materials.

Sb is widely used as a surfactant because of its low surface energy. Sub-monolayer coverages of Sb change the growth mode of Ag(111) from multilayer

(3D) growth to layer-by-layer (2D) growth [12]. Very recently we have found that during Ag growth, predeposition of Sb may lead to a top layer with the wrong stacking [31]. The surfactant effect of Sb is closely related to its strong tendency to segregate, but despite the increased interest in the use of surfactants in metal growth, the microscopic mechanisms of dissolution and segregation of Sb are at present not fully understood [32]. The surfactant effect is dependent on the coverage, and the occurrence of a  $(\sqrt{3} \times \sqrt{3})R30^\circ$  reconstruction may also play a role [33, 34]. Prerequisite for a better understanding of these phenomena is knowing the surface atomic structure. There has been, however, relatively little published on the structure of submonolayer coverages of Sb on clean metal surfaces.

For Ag(111), ab initio calculations [35] predict that for coverages up to 1/3 monolayer (ML) Sb is embedded in the top surface layer at substitutional sites. A  $(\sqrt{3} \times \sqrt{3})R30^\circ$  reconstruction is formed at 1/3 ML. These predictions are confirmed by experimental studies [32, 36–38]. At approximately double the Sb coverage a  $(2\sqrt{3} \times 2\sqrt{3})R30^\circ$  reconstruction is reported for annealing temperatures between 100 and 200°C [37]. No exact atomic coordinates have been derived from these studies.

After deposition of 1 ML of Sb on Cu(111) at 400°C dissolution in the bulk leaves behind a surface concentration of 1/3 ML with a  $(\sqrt{3} \times \sqrt{3})R30^\circ$  reconstruction [39, 40]. The segregation kinetics at the same temperature of Sb to the surface of a Cu(Sb)(111) solid solution (0.45 at%) similarly gives rise to this  $(\sqrt{3} \times \sqrt{3})R30^\circ$  reconstruction at the same surface Sb concentration. The dissolution and segregation kinetics are thus closely linked to the equilibrium surface segregation. Since the  $(\sqrt{3} \times \sqrt{3})R30^\circ$  reconstruction can be formed by either segregation or dissolution, we conclude that this must be an equilibrium structure.

On Au(111), also a noble metal, no  $(\sqrt{3} \times \sqrt{3})R30^\circ$  reconstruction is observed, but rather a  $(2\sqrt{3} \times 2\sqrt{3})R30^\circ$  structure forms, which is proposed to be a surface alloy of AuSb<sub>2</sub> stoichiometry, where the Sb atoms again occupy substitutional sites [41].

In this chapter, we present an X-ray diffraction structure determination of the Ag(111) $(\sqrt{3} \times \sqrt{3})R30^\circ$ -Sb and Cu(111) $(\sqrt{3} \times \sqrt{3})R30^\circ$ -Sb surfaces. Surface X-ray diffraction has proved to be an excellent technique for determining atomic positions with a high degree of accuracy [19]. Our analysis is based upon comparison of calculated model structure factors with the distribution of diffracted intensities along rods of scattering perpendicular to the surface. These so-called crystal truncation rods (CTRs) originate from the abrupt truncation of the crystal lattice at the surface [21, 22] and are diffuse tails whose intensity is given by the interference between bulk and surface atomic structure. We also measured fractional order reflections which are caused by the reconstruction and yield information about the

## $(\sqrt{3} \times \sqrt{3})R30^\circ$ -Sb RECONSTRUCTIONS OF Ag(111) AND Cu(111)

atomic arrangement in the surface unit cell only. For both reconstructions, we find a similar atomic structure. A model featuring a top layer with one Sb atom and two Ag (or Cu) atoms in the surface unit cell at stacking fault positions describes our data best. This position has not been considered in the studies mentioned above.

### 2.2 Experimental

The measurements were performed at the surface X-ray diffraction station 9.4 of the 5 T wiggler beam line at the Synchrotron Radiation Source, Daresbury Laboratory, United Kingdom [42]. X-rays with a wavelength  $\lambda$  of 0.9 Å (13.8 keV) were selected using a channel-cut Si(111) monochromator. The set-up consists of an ultra-high vacuum chamber [43] coupled to a diffractometer. A Knudsen effusion cell was used for the Sb deposition at a rate of  $\sim 0.002$  ML/sec. The deposition rate was estimated by assuming Poisson growth during deposition at low substrate temperatures. To prepare the surface reconstructions, Sb was deposited at elevated temperatures, but both structure determinations were carried out at room temperature. The diffractometer, on which the sample was mounted with the surface normal lying in the horizontal plane, was operated in six-circle mode with the out-of-plane detector angle fixed at  $0^\circ$  or  $15^\circ$  [44, 45].

We used round crystals with a diameter of 10 mm polished within  $\sim 0.3^\circ$  of the crystallographic (111) plane. In order to remove the surface damage from the polishing treatment both samples were first annealed to temperatures sufficient for significant sublimation to occur. The Ag(111) sample was annealed for 3.5 h at  $700^\circ\text{C}$ , reducing the surface mosaicity from  $2^\circ$  to  $0.10^\circ$  full width at half maximum (FWHM). After that, the sample was cleaned by repeated cycles of sputtering (600 eV  $\text{Ar}^+$  at  $300^\circ\text{C}$  for 20 min) and annealing ( $600^\circ\text{C}$  for 10 min). For Cu(111) an anneal treatment for 20 min at  $900^\circ\text{C}$  reduced the surface mosaicity from  $1.1^\circ$  to  $0.08^\circ$  FWHM. Thereafter the sample was cleaned by repeated cycles of sputtering at room temperature and annealing at  $700^\circ\text{C}$ .

The fcc crystals have an ABC stacking along the  $\langle 111 \rangle$  direction. A hexagonal unit cell is employed to label the reflections  $(hkl)$ . The lattice vectors  $\{\mathbf{a}_i\}$  are expressed in terms of the conventional cubic lattice vectors by

$$\mathbf{a}_1 = \frac{1}{2} [1\ 0\ \bar{1}]_{\text{cubic}}, \quad \mathbf{a}_2 = \frac{1}{2} [\bar{1}\ 1\ 0]_{\text{cubic}}, \quad \mathbf{a}_3 = [1\ 1\ 1]_{\text{cubic}}, \quad (2.1)$$

with

$$|\mathbf{a}_1| = |\mathbf{a}_2| = \frac{1}{2}\sqrt{2}a_0, \quad |\mathbf{a}_3| = \sqrt{3}a_0,$$

and  $a_0$  the lattice constant of Ag (4.09 Å) or Cu (3.61 Å). The corresponding reciprocal lattice vectors  $\{\mathbf{b}_i\}$  are defined by  $\mathbf{a}_i \cdot \mathbf{b}_j = 2\pi\delta_{ij}$ .



## CHAPTER II

The momentum transfer vector  $\mathbf{Q}$  is the difference between the outgoing wavevector  $\mathbf{k}_{\text{out}}$  and the incoming wavevector  $\mathbf{k}_{\text{in}}$  ( $|\mathbf{k}_{\text{out}}| = |\mathbf{k}_{\text{in}}| = 2\pi/\lambda$ ) and is denoted by diffraction indices  $(hkl)$  in reciprocal space:

$$\mathbf{Q} = h\mathbf{b}_1 + k\mathbf{b}_2 + l\mathbf{b}_3 . \quad (2.2)$$

Here the diffraction index pair  $(hk)$  refers to the in-plane component and the index  $l$  to the perpendicular component of  $\mathbf{Q}$ . For CTRs, which are labeled by  $(hk)$ , the indices  $h$  and  $k$  have integer values, whereas  $l$  is unconstrained. The perpendicular momentum transfer along the rods was varied by changing the incoming angle  $\beta_{\text{in}}$ , keeping the exit angle  $\beta_{\text{out}}$  fixed at  $1^\circ$ . In-plane data were collected using small incidence and exit angles ( $\beta_{\text{in}} = \beta_{\text{out}} < 1^\circ$ ) corresponding to small values of perpendicular momentum transfer ( $l = 0.2$ ). Slits in front of the Ge solid-state detector fixed the angular acceptance at  $0.26^\circ$  in the in-plane and  $0.43^\circ$  in the out-of-plane direction. These correspond to momentum resolutions of  $\Delta Q = 0.03 \text{ \AA}^{-1}$  and  $0.05 \text{ \AA}^{-1}$ , respectively.

Integrated intensities at various values of  $l$  along a non-specular diffraction rod are determined by rotating the crystal about the surface normal and measuring the number of diffracted photons. For a specific reflection  $(hkl)$ , the integrated intensity is given by [46]

$$I_{hkl}^{\text{int}} = \left( \frac{r_e^2 I_0 \lambda^2 \Delta\gamma}{\omega A_u^2} \right) C |F_{hkl}|^2 , \quad (2.3)$$

where  $r_e$  is the classical electron radius,  $I_0$  is the intensity of the incoming beam,  $\Delta\gamma$  is the opening angle of the detector in the out-of-plane direction,  $\omega$  is the angular scanning speed, and  $A_u$  is the surface unit cell area. This part of  $I_{hkl}^{\text{int}}$  is constant for all reflections.  $F_{hkl}$  is the structure factor. The correction factor  $C = L \cdot P \cdot A$  comprises the Lorentz factor  $L$ , the polarization factor  $P$ , and the area correction  $A$ . The Lorentz factor  $L$  is given by [46]

$$L = (\cos \beta_{\text{in}} \sin \delta \cos \gamma)^{-1} , \quad (2.4)$$

where  $\delta$  is the in-plane and  $\gamma$  the out-of-plane detector angle. Since the polarization of synchrotron radiation is almost completely in the horizontal plane, we may ignore the vertical component of the electric field vector. The polarization factor  $P$  may then be written as

$$P = 1 - (\sin \alpha \cos \delta \cos \gamma + \cos \alpha \sin \gamma)^2 , \quad (2.5)$$

where  $\alpha$  is the joint rotation angle of sample and detector [44]. The area correction  $A$  is calculated numerically [46] by taking a grid in the sample surface plane and

( $\sqrt{3} \times \sqrt{3}$ )R30°-SB RECONSTRUCTIONS OF AG(111) AND CU(111)

calculate for each point in the grid (i) whether it lies on the sample, (ii) whether it is visible from the detector, and (iii) the incoming beam intensity (normalized to the peak value). For the beam profile we took a Gaussian line shape with a FWHM of 2 mm in the horizontal and 0.6 mm in the vertical direction.

The specular reflected intensity distribution along the  $(hk) = (00)$  rod is measured in a different way, namely using a “ridge” scan, in which the incident and exit angles are symmetrically incremented (keeping  $\beta_{\text{in}} = \beta_{\text{out}}$ ). The intensity at different  $l$  values is measured by counting the scattered photons within the angular acceptance of the detector. The structure factor is then obtained by dividing the measured intensity by the correction factors  $L$ ,  $P$ , and  $A$ , and taking the square root.  $A$  is again numerically calculated and  $L$  and  $P$  are given by [46]

$$L = (\sin \beta_{\text{in}})^{-1}, \quad P = (\cos 2\beta_{\text{in}})^2. \quad (2.6)$$

We start our analysis with model structure factors calculated for a given atomic arrangement in the unit cell. To calculate the contribution arising from the bulk of the crystal,  $F_{hkl}^{\text{bulk}}$ , we describe the crystal by slicing it in columns perpendicular to the surface having a  $(1 \times 1)$  periodicity. Subsequently, we section the columns into (111) layers and sum over all the layers. Each layer contains only one atom and the structure factor for a single layer is

$$F_{hkl}^{\text{layer}} = f^{hkl} \exp\left(\frac{-BQ^2}{16\pi^2}\right), \quad (2.7)$$

where  $f^{hkl}$  is the atomic form factor and  $B$  is the isotropic Debye-Waller parameter. Throughout we assume the value of  $B$  to be equal to the room-temperature bulk value of  $0.66 \text{ \AA}^2$  for Ag and  $0.55 \text{ \AA}^2$  for Cu [47]. Each layer is shifted over a translation vector  $\mathbf{r}^{\text{layer}} = \frac{2}{3}\mathbf{a}_1 + \frac{1}{3}\mathbf{a}_2 + \frac{1}{3}\mathbf{a}_3$ . For the  $n$ th layer this results in a phase shift  $\exp(i n \psi_{hkl})$  with

$$\psi_{hkl} = \mathbf{Q} \cdot \mathbf{r}^{\text{layer}} = 2\pi \left( \frac{2}{3}h + \frac{1}{3}k + \frac{1}{3}l \right). \quad (2.8)$$

The resultant structure factor  $F_{hkl}^{\text{bulk}}$  is obtained by summing over all layers which make up the truncated crystal:

$$\begin{aligned} F_{hkl}^{\text{bulk}} &= \sum_{n=-\infty}^0 F_{hkl}^{\text{layer}} \exp(i n \psi_{hkl}) \exp(n\mu) \\ &= \frac{F_{hkl}^{\text{layer}}}{1 - \exp(-i\psi_{hkl}) \exp(-\mu)}, \end{aligned} \quad (2.9)$$

## CHAPTER II

with  $\mu$  an attenuation parameter that can be neglected in practice.

The semi-infinite columns of bulk unit cells are covered by  $(\sqrt{3} \times \sqrt{3})R30^\circ$  reconstructed surface unit cells, giving rise to fractional order reflections. For fractional order reflections there is no contribution from the bulk and the structure factor  $F_{hkl}^{\text{sur}}$  for the surface unit cell can be written as

$$F_{hkl}^{\text{sur}} = \sum_j f_j^{hkl} \exp\left(\frac{-B_j Q^2}{16\pi^2}\right) \exp[2\pi i (hx_j + ky_j + lz_j)], \quad (2.10)$$

where the summation extends over all atoms  $j$  with atomic coordinates  $x_j$ ,  $y_j$ , and  $z_j$  in the surface unit cell. For the integer order rods the square of the total structure factor is computed as follows:

$$|F_{hkl}|^2 = (1 - \theta) |F_{hkl}^{\text{bulk}}|^2 + \theta |3 F_{hkl}^{\text{bulk}} + F_{hkl}^{\text{sur}}|^2. \quad (2.11)$$

$\theta$  is the fraction of the surface that adopts the model surface structure. The factor three accounts for the difference in area between the bulk and surface unit cells, since there are three bulk unit cells within every surface unit cell. The atomic positions in the surface unit cell are fitted to the experimentally determined structure factors using a  $\chi^2$  minimization method.

### 2.3 Results

#### 2.3.1 $\text{Ag}(111)(\sqrt{3} \times \sqrt{3})R30^\circ\text{-Sb}$

First we investigate the deposition of Sb on Ag(111) close to equilibrium. In Fig. 2.1 the intensity of the  $(hkl) = (0\ 1\ 0.3)$  reflection is shown during deposition at a substrate temperature of 250°C. This reflection is very sensitive to stacking disorder, because atoms which grow at hcp sites interfere mainly constructively with the bulk, while atoms at the correct fcc sites interfere largely destructively. We can illustrate this with Eq. (2.8), where we find for this reflection for the correct fcc stacking a phase  $\psi_{010.3} = 0.87\pi$ . A layer of atoms at hcp sites is shifted with respect to the bulk over a translation vector  $\mathbf{r}^{\text{stackingfault}} = \frac{1}{3}\mathbf{a}_1 + \frac{2}{3}\mathbf{a}_2 + \frac{1}{3}\mathbf{a}_3$ . Then Eq. (2.8) becomes

$$\psi_{hkl} = \mathbf{Q} \cdot \mathbf{r}^{\text{stackingfault}} = 2\pi \left( \frac{1}{3}h + \frac{2}{3}k + \frac{1}{3}l \right), \quad (2.12)$$

which gives  $\psi_{010.3} = 1.53\pi$ . The difference in intensity can be calculated by comparing the squared structure factor amplitudes for these situations:

$(\sqrt{3} \times \sqrt{3})R30^\circ$ -Sb RECONSTRUCTIONS OF Ag(111) AND Cu(111)

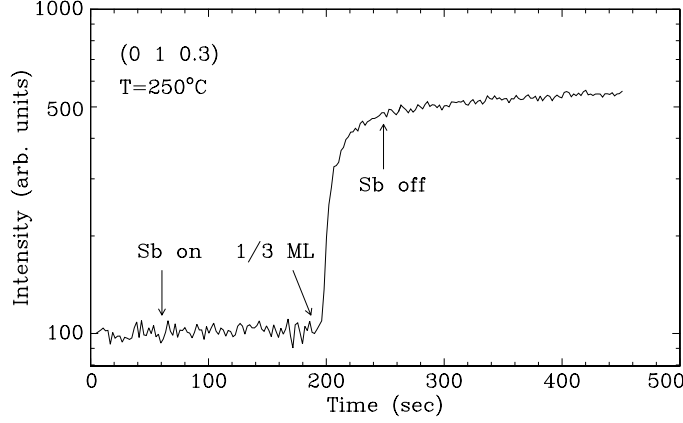


**Figure 2.1:** The  $(0\ 1\ 0.3)$  reflection during Sb deposition at a Ag(111) substrate temperature of 250°C. After 1/3 ML the  $(\sqrt{3} \times \sqrt{3})R30^\circ$  reconstruction is formed.

$$\frac{|F_{010.3}^{\text{stackingfault}}|^2}{|F_{010.3}^{\text{bulk}}|^2} = 6. \quad (2.13)$$

After starting the deposition, first the intensity remains constant, indicating that the surface remains smooth. Therefore, the Sb atoms must dissolve in the top layer, as was also observed using Scanning Tunneling Microscopy (STM) [34] and predicted by theoretical calculations [35]. After 1/3 ML of Sb deposition, a sudden rise in intensity is seen, indicative of the abrupt formation of stacking faults. The intensity rise is almost the factor 6 calculated above, indicating that *all* top layer atoms, i.e. not only the Sb atoms, occupy hcp sites. This coincides with the formation of the  $(\sqrt{3} \times \sqrt{3})R30^\circ$  reconstruction as was confirmed by measuring the  $(\frac{1}{3}\ \frac{1}{3}\ 0.2)$  reflection. From the measured peak FWHM we derived a correlation length  $L$  of 400 Å, where  $L = 2/\Delta Q_{FWHM}$  [48].

The surface reconstruction was prepared twice, resulting in two data sets. For the first preparation 152 structure factors were measured, of which 106 were non-equivalent and for the second 104 reflections, of which 65 were non-equivalent. The uncertainty  $\sigma_{hkl}$  of the measured structure factor amplitudes was determined by quadratically summing the statistical and systematic error. The latter was estimated from symmetry equivalent reflections to be 10% for the first data set and 5% for the second. Total structure-factor amplitudes measured along the  $(0\ 1)$ ,  $(0\ 2)$ , and  $(1\ 1)$  CTRs are shown in Fig. 2.2, together with model calculations. These are plotted as function of the diffraction index  $l$ , expressed in reciprocal lattice units (r.l.u.). The

CHAPTER II

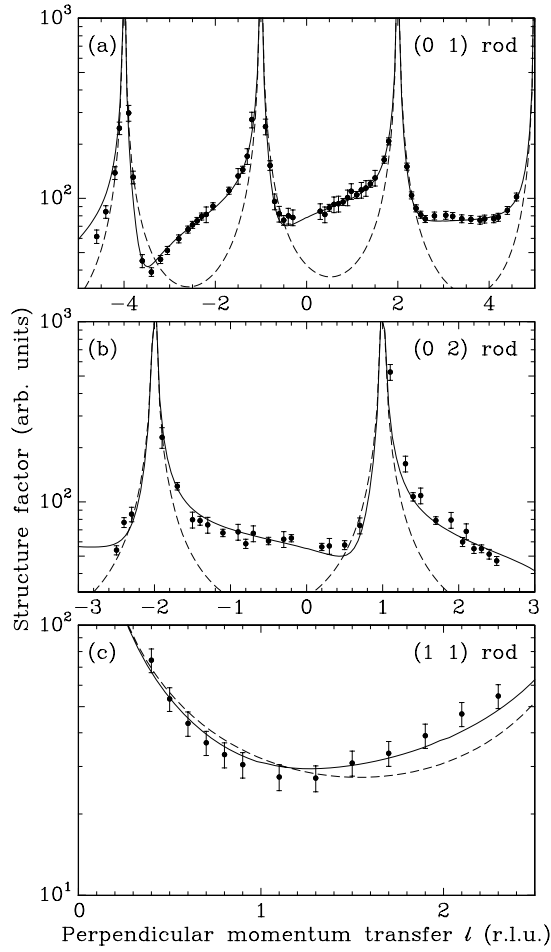


**Figure 2.2:** Structure factor amplitudes  $|F_{hkl}|$  along the  $(01)$ ,  $(02)$ , and  $(11)$  crystal truncation rods measured on  $\text{Ag}(111)(\sqrt{3} \times \sqrt{3})R30^\circ\text{-Sb}$ . Measured structure factors are indicated by filled circles. The dashed curves give calculations for the flat bulk-terminated  $\text{Ag}(111)$  surface and the solid curves represent calculations for our best-fit model.

$(\sqrt{3} \times \sqrt{3})R30^\circ$ -Sb RECONSTRUCTIONS OF Ag(111) AND Cu(111)

negative  $l$  parts of the (0 1) and (0 2) rods were obtained by inverting the structure-factor distribution along the positive (0  $\bar{1}$ ) and (0  $\bar{2}$ ) rods, respectively, through the origin of reciprocal space (Friedel's rule). The solid curves are calculated for our best-fit structural model. Dashed curves show calculations for an ideal, bulk-terminated Ag(111) surface.

A schematic of our model structure is shown in Fig. 2.3. Arrows indicate the allowed relaxation directions in our fit procedure. The total number of free fitting parameters was five, including a global scale factor, the surface fraction parameter  $\theta$ , and three atomic displacement parameters. The starting position of the Sb atoms was a hcp substitutional site, allowed to relax in the out-of-plane direction (parameter  $\Delta z_{\text{Sb}}$ ). The two Ag atoms in the top layer were also situated at hcp positions and allowed to relax out-of-plane (parameter  $\Delta z_{\text{metal}}$ ). The three second layer Ag atoms below the Sb atom were allowed to relax laterally in the direction to (or from) the Sb atom (parameter  $\Delta x$ ).

In Fig. 2.4(a) the specular rod is shown, which is only sensitive to the out-of-plane positions of the atoms. Open circles represent measured data for clean Ag(111) and filled circles for the Sb-covered surface. For both surfaces, no significant surface roughness is found. Since the difference in scattering power between Sb ( $Z = 51$ ) and Ag ( $Z = 47$ ) is very small and only small relaxations occur, the fractional order reflections are very weak. In Fig. 2.4(b) the fractional order ( $\frac{1}{3} \frac{1}{3}$ ) rod is shown.

The fit parameters and resulting nearest-neighbour distances for the atoms indicated in Fig. 2.3 are listed in Table 2.1. The best-fit atom coordinates are listed in Table 2.2. Our best-fit model has a reduced  $\chi^2$  of 1.3. All top layer atoms have relaxations out of the surface plane. The bulk distance between two (111) planes is 2.36 Å. Relative to this distance the Sb atom relaxes outwards by 0.17 Å and the two Ag atoms by 0.14 Å. The in-plane displacement of the second layer Ag atoms in the direction of the Sb atom is 0.06 Å. The reduced  $\chi^2$  did not improve significantly by allowing these three atoms to relax in the direction perpendicular to the surface plane. Our integer order rods are rather insensitive to the small displacements in the surface plane. In fact, an almost equally good fit ( $\chi^2 = 1.4$ ) is obtained when the in-plane relaxations are in the opposite direction. However, when we use in the fitting procedure only the in-plane part of the data set,  $\chi^2$  goes up from 2.7 (best fit) to 4.2. Without in-plane relaxations  $\chi^2$  becomes 6.4. Ag and Sb atoms have essentially identical "size", as judged from their nearest-neighbour distances in bulk Ag (2.89 Å) and bulk Sb (2.90 Å). In Sb-Ag compounds the distance between Ag and Sb is about 2.97 Å. The nearest-neighbour distances in our model deviate from these values by less than 4%. Even in the surface case, which has more degrees of freedom, almost perfect substitution takes place.

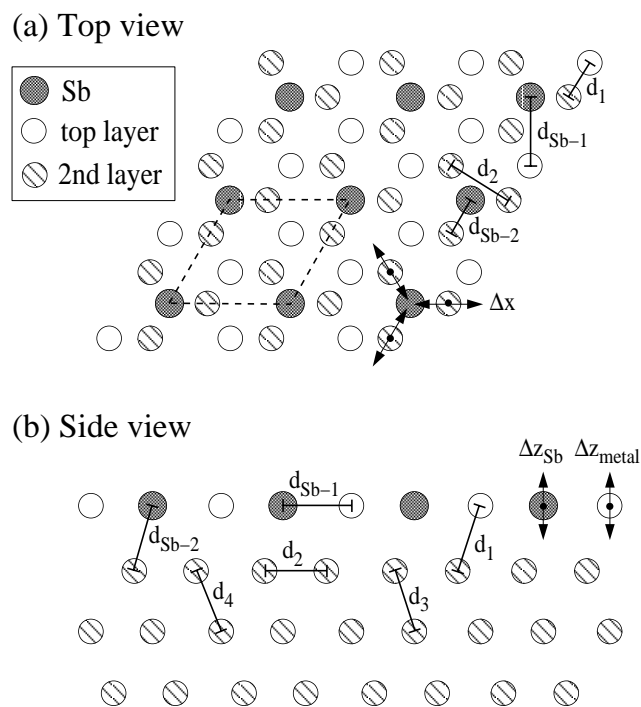


**Figure 2.3:** Schematic projections of our structural starting model for both reconstructions in top view (a) and side view (b). The  $(\sqrt{3} \times \sqrt{3})R30^\circ$  unit cell is indicated by the dashed lines. Arrows indicate the allowed relaxation directions in our fitting procedure. The indicated nearest-neighbour distances as derived from our best-fit model are given in Table 2.1.

$(\sqrt{3} \times \sqrt{3})R30^\circ$ -Sb RECONSTRUCTIONS OF Ag(111) AND Cu(111)

**Table 2.1:** Best-fit parameters and reduced  $\chi^2$  values for the structural models for Ag(111) $(\sqrt{3} \times \sqrt{3})R30^\circ$ -Sb and Cu(111) $(\sqrt{3} \times \sqrt{3})R30^\circ$ -Sb. The resulting nearest-neighbour atomic distances for the surface atoms (see Fig. 2.3) are given as well as the values for the nearest-neighbour distance in bulk Ag and Cu.

Fit parameter	Ag(111)	Cu(111)
$\theta$ surface fraction	0.75(3)	0.71(2)
$\Delta z_{\text{Sb}}$ (Å) Sb out-of-plane	0.17(6)	0.49(2)
$\Delta z_{\text{metal}}$ (Å) top Ag/Cu out-of-plane	0.14(3)	-0.11(2)
$\Delta x$ (Å) second layer Ag/Cu in-plane	0.06(5)	0.012(6)
$\chi^2$	1.3	1.3
Nearest neighbour distances (Å)		
$d_{\text{Sb}-1}$	2.89(1)	2.63(1)
$d_{\text{Sb}-2}$	2.99(8)	2.97(3)
$d_{\text{bulk}}$ (Ag/Cu)	2.89	2.56
$d_1$	3.02(3)	2.47(2)
$d_2$	2.78(8)	2.54(1)
$d_3$	2.85(2)	2.55(1)
$d_4$	2.91(1)	2.56(1)

**Table 2.2:** Structural parameters for the best-fit models of Ag(111) $(\sqrt{3} \times \sqrt{3})R30^\circ$ -Sb and Cu(111) $(\sqrt{3} \times \sqrt{3})R30^\circ$ -Sb (see Fig. 2.3). The atom positions in the surface unit cell are given by  $\mathbf{r} = x\mathbf{a}_1 + y\mathbf{a}_2 + z\mathbf{a}_3$ , with  $\{\mathbf{a}_i\}$  the fundamental translation vectors as defined in Eq. (2.1). Fixed values are indicated by an asterisk (\*). Deeper layers are fixed at bulk positions.

		$x$	$y$	$z$		$x$	$y$	$z$
Top layer	Sb	0.000*	0.000*	0.690	Sb	0.000*	0.000*	0.745
	Ag	0.000*	1.000*	0.686	Cu	0.000*	1.000*	0.649
	Ag	1.000*	1.000*	0.686	Cu	1.000*	1.000*	0.649
Second layer	Ag	0.679	1.358	0.333*	Cu	0.669	1.339	0.333*
	Ag	0.642	0.321	0.333*	Cu	0.661	0.331	0.333*
	Ag	-0.321	0.321	0.333*	Cu	-0.331	0.331	0.333*



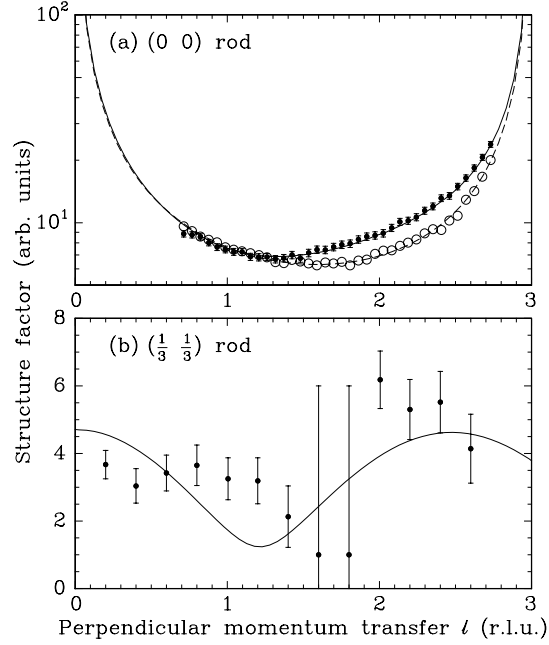


**Figure 2.4:** (a) The specular rod for the clean (open circles) and Sb-covered (filled circles) Ag(111) surface. The dashed curve gives a calculation for bulk-terminated Ag(111) and the solid curve represents our model calculation. (b) Structure-factor amplitudes  $|F_{hki}^{\text{sur}}|$  along the fractional order ( $\frac{1}{3}$   $\frac{1}{3}$ ) rod. Note that here the y-axis has a linear scale.

### 2.3.2 Cu(111)( $\sqrt{3} \times \sqrt{3}$ )R30°-Sb

For Sb on Cu(111) we find similar results as for Ag(111). In Fig. 2.5 the intensity of the (010.9) reflection is shown during Sb deposition on Cu(111) at 450°C. Initially, the intensity increases slowly, after which it steeply rises and levels off to a constant value. The (010.9) reflection is even more sensitive to stacking faults than the (010.3) which was monitored for Ag(111) (Fig. 2.1). Because the scattering power difference between Sb ( $Z = 51$ ) and Cu ( $Z = 29$ ) is rather large, we find for Eq. (2.13) an intensity increase of factor 10 for a complete stacking fault layer with 1/3 ML of Sb. Without the stacking fault, this factor is 2 (because of the difference in  $Z$ , the Sb is observable in this case, unlike for Ag in Fig. 2.1). This explains why first the intensity rises by almost a factor 2 when the coverage comes close to 1/3 ML. Thus, analogous to the case of Ag(111), the Sb atoms dissolve in the top layer. Then the ( $\sqrt{3} \times \sqrt{3}$ )R30° reconstruction is formed with

$(\sqrt{3} \times \sqrt{3})R30^\circ$ -Sb RECONSTRUCTIONS OF Ag(111) AND Cu(111)

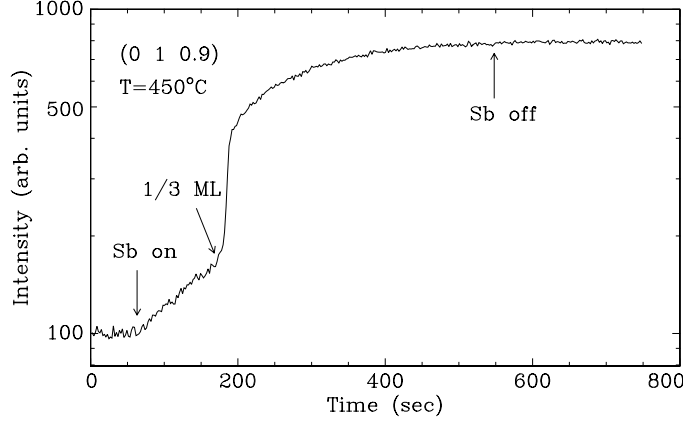


**Figure 2.5:** The  $(0\ 1\ 0.9)$  reflection during Sb deposition on Cu(111) at  $450^\circ\text{C}$ . After  $1/3$  ML the  $(\sqrt{3} \times \sqrt{3})R30^\circ$  reconstruction is formed.

all the top layer atoms at stacking fault positions, resulting in an intensity rise of almost factor 10. During cool down to room temperature, the intensity remained the same. No significant surface roughness is found after deposition. By measuring the fractional order  $(\frac{1}{3}\ \frac{1}{3}\ 0.2)$  reflection, we estimated the correlation length  $L$  to be  $380\ \text{\AA}$ .

In total, 205 structure factors were measured, of which 83 were non-equivalent. The uncertainty for this data set was estimated to be 10%. In Fig. 2.6, the data for the integer-order  $(0\ 1)$  rod, the specular rod, and the fractional order  $(\frac{1}{3}\ \frac{1}{3})$  rod are shown together with our best-fit model calculations (solid curves). The dashed curves show calculations for bulk-terminated Cu(111).

The best-fit model parameters, atom coordinates, and resulting nearest-neighbour distances are listed in Tables 2.1 and 2.2. An important difference with the structure of the  $\text{Ag}(\sqrt{3} \times \sqrt{3})R30^\circ$ -Sb reconstruction is a reversal of the perpendicular relaxation direction of the Cu atoms. We find that the Sb atoms relax outwards by an amount of  $0.49\ \text{\AA}$  but the Cu atoms relax inwards by  $0.11\ \text{\AA}$ . This represents 5% of the bulk (111) interplanar distance of  $2.09\ \text{\AA}$ . The in-plane relaxation of the second layer Cu atoms in the direction of the Sb atoms is estimated to be only  $0.01\ \text{\AA}$ .

A model for which the Sb relaxes inwards and the two top layer Cu atoms outwards gives an equally good fit. However, the distance  $d_{\text{Sb}-1}$  then becomes  $2.42\ \text{\AA}$ , and  $d_1$   $2.94\ \text{\AA}$ . Both these distances are clearly unphysical and can therefore be excluded. In  $\text{Cu}_2\text{Sb}$  the nearest-neighbour distances of Sb and Cu are  $2.63\ \text{\AA}$ ,

CHAPTER II

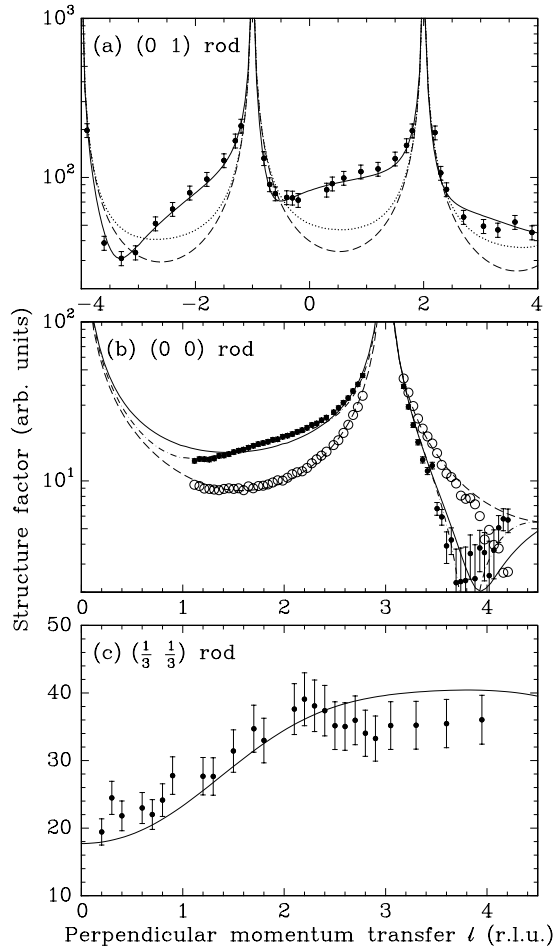


**Figure 2.6:** Structure-factor amplitudes along the  $(01)$ ,  $(00)$ , and  $(\frac{1}{3}\frac{1}{3})$  crystal truncation rods for  $\text{Cu}(111)(\sqrt{3} \times \sqrt{3})R30^\circ\text{-Sb}$ . Measured structure factors are indicated by filled circles. The open circles in (b) are measurements of clean  $\text{Cu}(111)$ . The dashed curves give the calculation for the bulk-terminated  $\text{Cu}(111)$  surface and the solid curves represent best-fit model calculations. In (a) the dotted curve represents a calculation for a structural model where the Sb atom is at a “normal” substitutional fcc site. For the specular rod in (b) the dashed-dotted curve represents a calculation with an extra Sb atom on top of the surface (see text).

## $(\sqrt{3} \times \sqrt{3})R30^\circ$ -Sb RECONSTRUCTIONS OF Ag(111) AND Cu(111)

2.71 Å, and 2.84 Å, which come close to our best-fit result of 2.63 Å and 2.97 Å. The nearest-neighbour Cu-Cu distance  $d_1$  is reduced by 4% compared to the bulk value.

The agreement between our model and the measured specular rod is good, but there are statistically significant deviations that are not explained by the model, particularly in the range  $1 < l < 2$ . Since the specular reflectivity probes the electron density distribution perpendicular to the surface, atoms which do not follow the lateral periodicity on the surface also contribute to the scattering. The deposition of Sb on the surface was stopped at an arbitrary position in time, but definitely past the place where the surface orders. Presumably there are Sb clusters at some parts on the surface. If we assume 0.06 ML of extra Sb atoms at arbitrary fixed positions on top of the surface, we obtain the dashed-dotted curve shown in Fig. 2.6(b). This may not be a physically realistic model, but it shows that a small amount of extra Sb on top can make a large difference in the specular reflectivity.

### 2.4 Discussion

The sudden formation of the  $(\sqrt{3} \times \sqrt{3})R30^\circ$  reconstruction as a function of the Sb coverage, as shown in Figs. 2.1 and 2.5, bears a striking resemblance to the phase transition in the exact solvable hard-hexagon model in statistical mechanics [49]. In this model hexagons can be positioned on three different sites, but may not overlap (hence the name of the model). In our case these hexagons can be associated with the Sb atoms which have three equivalent sites. In the hard hexagon model there is a critical coverage above which the phase orders:  $\rho_c = (5 - \sqrt{5})/10 = 0.28$ . Below this coverage, the three sites are randomly occupied, in agreement with STM [34]. A perfect  $(\sqrt{3} \times \sqrt{3})R30^\circ$  reconstruction would have a coverage of 1/3 ML. The intensity rise depicted in Fig. 2.1 is estimated to be after deposition of 0.31(3) ML Sb. The value of 0.28 is just within our error bar. In our best-fit models we find for the surface fraction parameter  $\theta$  values of 0.75 and 0.71, corresponding to an ordered Sb coverage of 0.25 and 0.23 ML, respectively. Part of the Sb atoms are not involved in the reconstruction. Even though these values are close to the value of 0.28, the difference with the ideal coverage of 1/3 ML may be fully explained by the possibility that not the entire surface is reconstructed. The qualitative agreement with the hard-hexagon model strongly suggests that the main driving force of the  $(\sqrt{3} \times \sqrt{3})R30^\circ$  reconstruction is the repulsive interaction between Sb atoms.

For both reconstructions we find in essence a very similar surface atomic structure. The hcp site for the top layer atoms is energetically favoured for both Ag and Cu. Comparing the fit parameters listed in Table 2.1 we see that differences

occur only in the out-of-plane relaxations. This is a purely geometrical effect. Sb and Ag are similar in size, while Cu is significantly smaller. On the Cu substrate, the Sb atoms therefore need more space and the out-of-plane relaxation of the Sb atoms is much larger than on Ag(111). At the same time, the top layer Cu atoms are pushed towards the surface. This unusual embedded substitutional structure for an adsorbate-metal structure involving larger  $Z$  adatoms was already proposed years ago for Te ( $Z = 52$ , about the same size as Sb) on Cu(111) [50]. For both reconstructions our models result in reasonable distances between the Sb and metal atoms. Because of the relaxation of the Cu atoms towards the surface, the distance between the Cu top and second layer atoms decreases with respect to the bulk nearest-neighbour distance. This is also the case for clean Cu(111), for which a top-layer spacing contraction of 0.7% relative to the layer spacing in the bulk was reported [51]. This corresponds to a nearest neighbour distance  $d_1$  of 2.54 Å.

To distinguish between three possible structural models, Noakes *et al.* [37] have compared coaxial impact collision ion scattering spectroscopy data taken on Ag(111)( $\sqrt{3} \times \sqrt{3}$ )R30°-Sb to hitting probability simulations. Two models assume a simple Sb overlayer, where the Sb atoms can either occupy fcc or hcp sites. A third model involves the substitution of one top layer Ag atom per surface unit cell by an Sb atom. From their measurements they conclude that the correct model of the surface structure is that based on this substitutional adsorption site. From our observation of the growth as depicted in Fig. 2.1, we can conclude that the overlayer models can be ruled out, as was also reported by STM measurements [34] and predicted by theoretical calculations [35]. We can also rule out the substitutional model by looking at the data of e.g. the (0 1) rod. The expected structure factor distribution for this substitutional model is indistinguishable from the calculation for the clean Ag(111) surface (dashed curve in Fig. 2.2(a)). This is because Ag has (almost) the same scattering power. Because Cu has a smaller  $Z$ , we can illustrate the substitutional model better for the Cu(111)( $\sqrt{3} \times \sqrt{3}$ )R30°-Sb case. The dotted curve in Fig. 2.6(a) shows a calculation for this structure. The intensity contribution from the surface (in between the Bragg peaks) is slightly higher because of the additional scattering power from the Sb atoms in the surface layer. The extra interference effect we observe in our data because of the hcp stacking is absent. The ion scattering spectroscopy data of Noakes *et al.* [37] is more sensitive to the fact that the Sb atoms are embedded than to the stacking of the top layer. In that sense this data agrees with our model.

In theoretical calculations [35] as well as in experiments of Cruguel *et al.* [38], another structural model was considered, namely one where the Sb is substituted in the second layer below the surface. On the same grounds as for the top layer substitutional site we can confirm that this is not a correct model. The theoretical

## $(\sqrt{3} \times \sqrt{3})R30^\circ$ -Sb RECONSTRUCTIONS OF Ag(111) AND Cu(111)

calculations [35] have shown that the substitutional site for Sb is considerably more favourable than an overlayer fcc site and than subsurface sites, but the stacking fault adsorption geometry we found was not considered. For the substitutional Sb an outward relaxation was predicted of about 0.25-0.35 Å, which is a rather large value. We have determined the outward Sb relaxation to be 0.17 Å (on the hcp site). In the calculations no outward relaxation of the Ag atoms was taken into account, but here we have shown that these are also significant: 0.14 Å. The difference in height between the Sb and Ag atoms is thus small, which is consistent with STM measurements for the  $(\sqrt{3} \times \sqrt{3})R30^\circ$  reconstruction, as well as for the  $1 \times 1$  phase for Sb coverages below 1/3 ML [33].

Very recently, our model has been corroborated. Medium-energy ion scattering measurements performed on Cu(111) $(\sqrt{3} \times \sqrt{3})R30^\circ$ -Sb are found to be consistent with the stacking fault position we propose [52].

Van der Vegt *et al.* [34] have studied the surfactant effect of Sb as function of coverage up to 0.3 ML. They observed the nucleated island density to increase exponentially with Sb coverage. It is not known, however, what the influence of the  $(\sqrt{3} \times \sqrt{3})R30^\circ$  reconstruction would be on this behavior. In an earlier study we have found that for sufficiently large Sb coverages, the top stacking fault layer described here is formed during Ag growth [31].

In conclusion, we have used the technique of surface X-ray diffraction to determine the structure of the  $(\sqrt{3} \times \sqrt{3})R30^\circ$ -Sb reconstructions of Ag(111) and Cu(111). We find that the top layer atoms reside at stacking fault positions and each surface unit cell contains one substitutional Sb atom. We determined not only the registry of the top layer atoms, but also their out-of-plane relaxations. Furthermore, for the second layer we find small in-plane relaxations towards the Sb atoms.



## III

### Floating stacking fault during homoepitaxial growth of Ag(111)

*We have investigated the influence of Sb on the formation of stacking faults during Ag(111) growth using X-ray scattering. In equilibrium, a predeposition of 1/3 monolayer Sb results in a  $(\sqrt{3} \times \sqrt{3})R30^\circ$  reconstruction in which the top layer is wrongly stacked. Upon continued Ag growth at 100° C, the Sb segregates and the Ag atoms return to the correct stacking, while the new Ag atoms in the top layer again have the wrong stacking. This thus effectively leads to a floating stacking fault. Because of kinetic limitations, the same effect occurs for lower Sb coverages.*

#### 3.1 Introduction

The growth of smooth and defect free metallic layers is important in many technological areas, like metal-semiconductor contacts and magnetic multilayers. Usually, high substrate temperatures are required to grow smooth layers, but this may cause interdiffusion problems. It has been shown for a number of metals that homoepitaxial growth of smooth layers can be stimulated by using surfactants [12, 27, 28, 30]. Surfactants have also been used in the growth of metallic films on Si and sapphire [53–55].

The occurrence of stacking faults is an important factor for the quality of the layers, since it determines whether the film is continuous, twinned or otherwise imperfect. At present, the influence of surfactants on the formation of stacking faults is not well understood. Submonolayer coverages of Sb change the growth mode of Ag(111) from multilayer (3D) growth to layer-by-layer (2D) growth [12], but this may sometimes enhance the formation of stacking faults [56]. On the other hand, the effect of Pb in the growth of Cu/Co superlattices on Cu(111) [11, 57] and the effect of In on the growth of Cu(111) [30] is to *suppress* the formation of stacking faults. For clean Ag(111) growth (without surfactant), Meinel, Klaua, and Bethge [58] observed that Ag(111) grows with stacking faults at room temperature (RT) and that for 2D nucleation the probabilities for incorrect



(hcp) and correct (fcc) atomic stacking are almost equal. Spot-profile analysis of low-energy electron diffraction (SPA-LEED) experiments confirm this conclusion [59, 60]. First principle calculations, on the other hand, show that for adatoms the fcc site is energetically slightly favoured over the hcp site [61].

In this chapter we describe a remarkable, new effect of Sb during Ag(111) homoepitaxial growth. Sb causes the top surface layer to be at stacking fault positions, but during growth the surface *unfaults* so that the grown film is not faulted and the stacking fault floats along with the Sb.

### 3.2 Experimental

We have used *in situ* surface X-ray diffraction for this study. Sensitivity to the growth mode, surface roughness, the formation of stacking faults, and/or the possible concomitant formation of twin crystallites is obtained by observing diffracted intensities at appropriate positions on so-called crystal truncation rods (CTRs) [22]. These CTRs are tails of diffuse intensity originating from the interference between bulk and surface atomic structure. The rods connect the bulk Bragg peaks in the direction perpendicular to the surface. Because of the weak interaction of X-rays with matter the kinematical approximation is valid, which makes data analysis straightforward [19]. The large penetration depth makes it possible to study stacking fault and twin crystal formation at buried interfaces.

The experiments were performed at the surface X-ray diffraction station 9.4 of the wiggler beam line at the Synchrotron Radiation Source, Daresbury Laboratory, United Kingdom [42]. Experimental details are given in chapter 2. A wavelength of 0.9 Å (13.8 keV) was selected using a channel-cut Si(111) monochromator. The setup consists of an ultra-high vacuum chamber [43] coupled to a five-circle diffractometer. The Ag(111) sample (miscut  $\sim 0.2^\circ$ ) was cleaned by repeated cycles of sputtering (600 eV Ar<sup>+</sup> at 300°C for 20 min) and annealing (600°C for 10 min). Knudsen effusion cells were used for Ag and Sb deposition. The Sb deposition rate was  $\sim 0.002$  monolayers (ML) per second and the deposition rate of Ag  $\sim 0.01$  ML per second. The deposited amounts of Sb given below have an error of 10%.

For labelling the reflections we use the surface unit cell as defined in section 2.2. The momentum transfer vector  $\mathbf{Q}$ , which is the difference between the wavevectors of the incident and scattered X-rays, can be denoted by the diffraction indices  $(hkl)$  in reciprocal space. For CTRs, which are labeled by  $(hk)$ , the indices  $h$  and  $k$  have integer values, whereas  $l$  is unconstrained and refers to the component of  $\mathbf{Q}$  perpendicular to the surface. The bulk Bragg peaks occur for integer values of  $l$ . The integrated intensity at each point  $l$  is determined by rotating the crystal about

the surface normal and measuring the number of diffracted photons. From the measured integrated intensities structure factors are derived in a standard fashion [46].

### 3.3 Results

In order to investigate the formation of stacking faults during growth we have measured the  $(hk) = (01)$  CTR. The observed profiles for homoepitaxial growth of Ag(111) without the use of a surfactant are shown in Fig. 3.1 for three different temperatures. For each temperature, the structure factor amplitudes after growth are plotted as a function of  $l$  (in reciprocal lattice units). Negative  $l$  values are obtained by inverting the structure factor distribution along the positive  $(hk) = (0\bar{1})$  rod through the origin of reciprocal space (Friedel's rule). The expected structure factor distribution for the clean flat Ag(111) bulk terminated surface is given by the dashed curve. The bulk Bragg peaks are at  $l = -1$  and  $l = 2$ . At RT (3 ML Ag deposited) and  $-50^\circ\text{C}$  (4 ML Ag deposited) twin crystallites are formed that are rotated  $180^\circ$  with respect to the bulk. The twin Bragg peaks thus lie exactly on the bulk CTR, but at  $l$  values that are the bulk values mirrored in the origin (i.e., at  $l$  equals -2 and 1). The solid curves represent model calculations. At  $-50^\circ\text{C}$  we find that 17% of the surface is covered by twins with a thickness of 4 ML. The RT data are best described taking 8% of the surface to be covered by 3 ML thick twin crystals. These twin crystals grow from a stacking fault formed at the annealed starting surface and then proceed with the 'normal' fcc stacking (ABCbacbac. . .). Presumably, the stacking faults are formed at defects or impurities on the surface. After depositing the first layer these are covered and no new stacking faults are created. At  $T = 100^\circ\text{C}$  (2 ML Ag deposited) no twin crystal formation is observed and the data correspond to the calculation for the ideal, bulk terminated surface of Ag(111).<sup>1</sup> We conclude that at higher temperatures fewer twin crystals are formed. This is caused by two effects. First, for higher temperatures, an increasing fraction of the arriving atoms will attach at step sites where they will reside at the correct stacking. Second, the higher mobility allows incorrectly nucleated islands to find the energetically favourable fcc site.

In chapter 2 we investigated Sb deposition on Ag(111) close to equilibrium. In Fig. 2.1 the intensity of the  $(hkl) = (010.3)$  reflection was shown during Sb deposition at  $250^\circ\text{C}$ . This reflection is very sensitive to the occurrence of stacking faults, because atoms which grow on hcp sites interfere mainly *constructively* with the bulk, whereas atoms on the correct fcc sites interfere largely *destructively*.

---

<sup>1</sup>Apparently, the surface is less rough than measured during specular reflectivity [12]. This is probably due to the fact that only 2 ML were deposited and that some annealing has occurred.

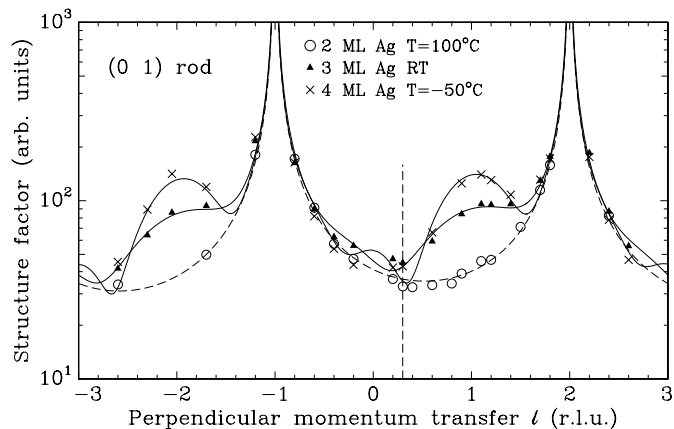


**Figure 3.1:** Structure factors along the  $(hk) = (01)$  CTR after clean Ag growth (no predeposition of Sb) at  $-50^\circ\text{C}$ , RT, and  $100^\circ\text{C}$ . The dashed curve gives the calculation for the bulk terminated Ag(111) surface and the solid curves represent best fits (see text). For the lower temperatures peaks start to appear at  $l = -2$  and  $l = 1$  indicating twin crystal formation. The vertical dashed line marks the position of the  $(hkl) = (010.3)$  reflection which is monitored during deposition in Figs. 2.1 and 3.2.

Note that this is different from specular reflectivity, where one is sensitive only to the out-of-plane position of the atoms, and not to their stacking [12]. In Fig. 2.1 the intensity initially remains constant, indicating that the surface remains smooth. Therefore, the Sb atoms must dissolve in the top layer, as was also found using scanning tunneling microscopy (STM) [34]. After deposition of approximately  $1/3$  ML of Sb a sudden rise in intensity is observed which is indicative of the formation of stacking faults. The intensity increase coincides with the formation of a  $(\sqrt{3} \times \sqrt{3})R30^\circ$  reconstruction. A detailed investigation of the exact atomic structure of this reconstruction was described in chapter 2. We found that in equilibrium all top layer atoms are on stacking fault positions and each surface unit cell contains one substitutional Sb atom [62].

Now we determine the effect of Sb on the growth of Ag. Below RT predeposition of Sb has no significant effect on the formation of twin crystals, although the growth mode changes from 3D to layer-by-layer as reported previously [12]. At  $100^\circ\text{C}$  no stacking faults occur for the clean surface, but predeposition of  $0.3$  ML of Sb has a profound effect on the CTR intensity distribution. In Fig. 3.2(a) the peak intensity of the  $(hkl) = (010.3)$  reflection is shown during deposition

FLOATING STACKING FAULT DURING AG(111) GROWTH

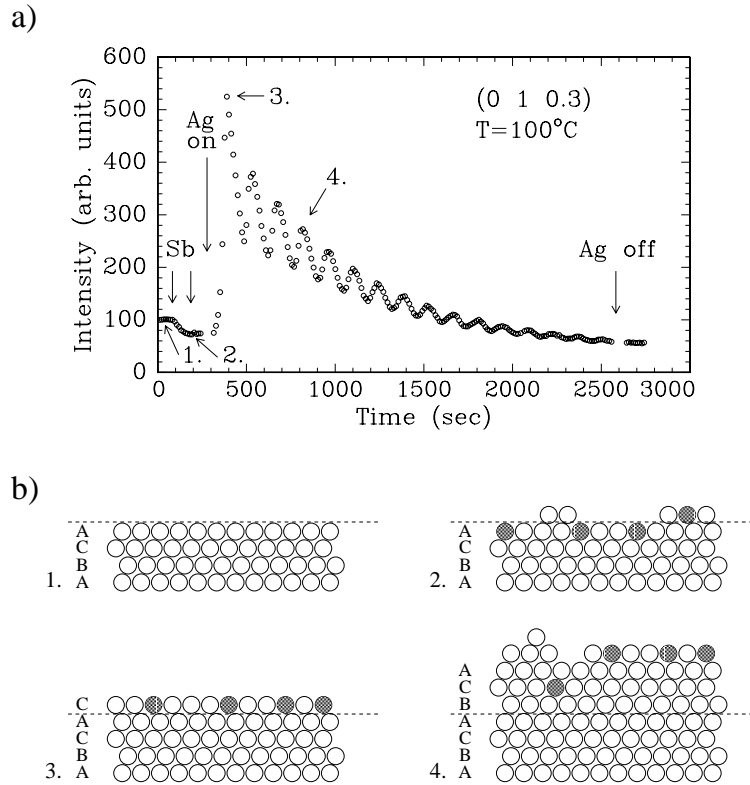


**Figure 3.2:** (a) The  $(hkl) = (010.3)$  reflection during 0.3 ML Sb deposition followed by 16 ML of Ag at 100°C. The numbers assign the different states depicted in (b). (b) Schematic side view of the surface during different stages of deposition. Open circles represent Ag atoms and filled circles represent Sb atoms. On the clean Ag(111) surface (1) 0.3 ML of Sb is deposited. The Sb is either on top or embedded in the top surface layer (2). After a total deposition (Sb+Ag) of 1 ML all atoms are on hcp sites (3). After 4 ML deposition (4) the surface atoms are partly correctly stacked (left) and partly hcp-stacked (right). The starting interface has returned to the correct fcc stacking (ABCAbca...).

## CHAPTER III

at 100°C. Different stages of the growth are schematically depicted in Fig. 3.2(b). First the intensity decreases because of an increase in surface roughness due to the deposition of Sb (note the difference with the near equilibrium situation at  $T = 250^\circ\text{C}$  in Fig. 2.1). On starting the Ag deposition a large increase in the yield is observed. Thereafter, the intensity oscillates with a 1 ML period and decays slowly back to the starting level. The initial increase indicates that all of the Ag (and Sb) atoms in the top layer occupy hcp sites. The increase of more than a factor five is the same as that measured in the transition to the  $(\sqrt{3} \times \sqrt{3})R30^\circ$  reconstruction shown in Fig. 2.1. When the buried Sb atoms segregate towards the surface during deposition, all Ag atoms in lower levels return to energetically favoured fcc sites. So the stacking fault is present only in the top layer and “floats” on the surface. Because the segregation of Sb is incomplete, the total number of atoms at hcp sites slowly decreases during growth, which results in the overall decrease in intensity. After 16 ML we find that 20% of the surface area has a stacking fault. The intensity is also reduced by the increasing surface roughness. During similar depositions the growth was interrupted at various points to measure the full CTR, allowing a detailed evaluation of the surface atomic structure and roughness. From this we know that indeed only the top layer has the hcp stacking and that the buried layers have the normal fcc stacking. No twinning is observed. Note that without the floating stacking fault, the oscillation amplitude would not rise above the starting value.

Surprisingly, a predeposition of less than 1/3 ML of Sb has a similar effect, as illustrated in Fig. 3.3. A deposition at 100°C of 0.2 ML Sb does not directly lead to a stacking fault in the top layer, as we have already concluded from the data in Figs. 2.1 and 3.2. If, however, we deposit on this surface 0.8 ML of Ag, *all* atoms in the top layer are wrongly stacked, while the absence of fractional order reflections indicates that no long range ordered  $(\sqrt{3} \times \sqrt{3})R30^\circ$  reconstruction exists. The solid curve in Fig. 3.3 shows the expected structure factor distribution for a top layer in which all the atoms are on hcp sites. For smaller amounts of Sb the top layer has only partly hcp stacking. This is illustrated for a deposition of 0.1 ML Sb followed by 5 ML of Ag. The stacking fault is still clearly visible in the CTR. The dashed-dotted curve is a calculation for a top layer of which 10% of the atoms are on hcp sites and the remainder on normal fcc positions. The stacking faults at this coverage are only formed due to kinetic limitations. After annealing of the layer, the CTR profile is identical to that of the clean bulk terminated crystal (open circles), meaning that all atoms occupy normal fcc sites.

## FLOATING STACKING FAULT DURING AG(111) GROWTH

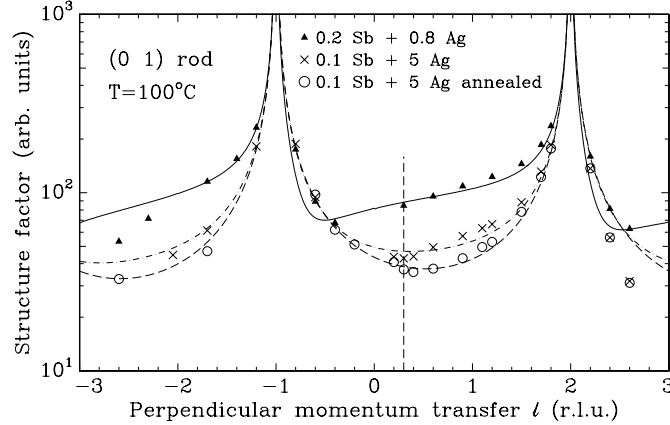


**Figure 3.3:** Structure factors along the (0 1) rod at 100°C. After 0.2 ML Sb plus 0.8 ML Ag deposition all top-layer atoms are on hcp sites (triangles). The solid curve represents a calculation for this. The crosses represent the data for a surface covered with 0.1 ML Sb and 5 ML Ag, which was thereafter annealed (open circles). The dash-dotted curve is a calculation for a state where 10% of the top layer has the hcp stacking and the rest has the normal fcc stacking. The dashed curve is calculated for the bulk terminated clean Ag(111) (data not shown). The vertical dashed line marks the position of the (0 1 0.3) reflection which was monitored during the depositions of Figs. 2.1 and 3.2.

### 3.4 Discussion and Conclusions

Next we explain these observations. STM experiments at RT [33, 34] have shown that after deposition of small amounts of Sb on Ag(111), Sb is present in two states: (1) as single embedded atoms in the top surface layer, and (2) incorporated in small islands with a  $(\sqrt{3} \times \sqrt{3})R30^\circ$  superstructure. It was shown that subsequently deposited Ag atoms attach to these  $(\sqrt{3} \times \sqrt{3})R30^\circ$  islands. From the data in Fig. 3.3 we conclude that these Ag atoms follow the hcp stacking of the  $(\sqrt{3} \times \sqrt{3})R30^\circ$  islands, even when the Sb coverage is less than 1/3 ML. After the first ML is completed, all Sb is embedded in the top layer and no  $(\sqrt{3} \times \sqrt{3})R30^\circ$  islands are present on top [32, 34]. Since we still observe some hcp stacking at higher coverage, a different mechanism must be active in these subsequent layers. This is provided by the fact that continued Ag growth leads to a place-exchange mechanism with embedded Sb [32]. If approximately one out of three arriving Ag atoms ‘releases’ an Sb atom, the effective surface Sb concentration is 1/3 and  $(\sqrt{3} \times \sqrt{3})R30^\circ$  islands can be nucleated. These newly formed islands then act as centers from which the

## CHAPTER III

hcp stacking propagates. Obviously, this is a statistical process. For a low Sb concentration, islands with the proper stacking will also occur. This picture is corroborated by our observation that when a surface covered with 0.2 ML of Sb is annealed prior to Ag deposition, only 40% of the surface has a stacking fault after 1 ML deposition (not shown), while without annealing the full top layer is wrongly stacked (see Fig. 3.3). In the latter case, there are already enough  $(\sqrt{3} \times \sqrt{3})R30^\circ$  islands on top of the surface, while for the annealed case these have to be produced by the exchange mechanism.

Upon continued growth the Ag atoms in the top layer return to fcc stacking positions, meaning that all atoms have to move from hcp to fcc sites. How this occurs is, at present, unclear. It seems likely that this process occurs at the edges of growing islands. A microscopic technique, like low-energy electron microscopy, is needed to clarify this issue. A similar registry shift of a single layer was reported recently for Cu/Co/Cu(111) sandwiches. It was found that thin cobalt films on Cu(111) can change from hcp stacking to fcc stacking when covered with a copper layer [63].

In summary, we have shown that Sb has a remarkable effect on the formation of stacking faults in the homoepitaxial growth of Ag(111). At an Sb coverage above 1/3 ML, thermodynamic equilibrium is achieved by a top layer with hcp stacking and a  $(\sqrt{3} \times \sqrt{3})R30^\circ$  reconstruction. At such an Sb coverage, deposition of Ag leads to a floating stacking fault. However, due to kinetic limitations and due to an exchange process between Sb and Ag atoms, even for lower Sb coverages a floating stacking fault is formed during Ag growth. For growth above 100°C, all lower lying Ag layers return to the correct stacking, and no twin crystallites are formed.

## IV

### Phase transition of a Pb monolayer on Ge(111)

*We present an X-ray diffraction structural analysis of the  $\beta$ -Ge(111)( $\sqrt{3}\times\sqrt{3}$ )R30° - Pb  $\rightarrow$  1 $\times$ 1 phase transition at  $\sim$ 180° C for a Pb coverage of 1.25 monolayer. We have studied the atomic structure below and above the phase transition by measuring the distribution of diffracted intensities along integer order rods of Bragg scattering. Below the phase transition the  $\beta$  phase has a saturation coverage of 4/3 monolayer. We find that above the phase transition the single layer of Pb gives rise to a ring of diffuse scattering indicative of a two-dimensional liquid. However, of all the Pb geometries considered, an ordered layer with high in-plane thermal vibration amplitude is found to provide the best agreement between calculated and measured structure factors. The Pb layer has thus both liquid and solid properties.*

#### 4.1 Introduction

Solid-liquid interfaces are found in many areas, but atomic-scale experimental data is scarce. Ultra-thin liquid boundary layers are thought to affect properties such as flow, lubrication and wear. Little is known about the interaction of liquid metals with solid surfaces in processes such as casting, moulding of steel and alloys, soldering, welding, and sintering. In the process of liquid-phase epitaxial growth, semiconductor surfaces are in contact with liquid metals [64]. Most theoretical predictions on the liquid ordering at solid-liquid interfaces have not been verified experimentally.

Liquid ordering in two dimensions is also of great fundamental interest [65]. Most experiments on two-dimensional systems are not on a free layer of atoms, but consist of a two-dimensional layer supported by a substrate. An important question in these systems is how the periodicity of the adlayer is related to the periodicity of the substrate. The solid-liquid interface that occurs during surface melting [66] is of equal fundamental interest, but also here the precise structure of the liquid remains unknown [67,68].

Pb monolayers adsorbed on Ge surfaces constitute an ideal two-dimensional metal. Since the mutual solid solubilities are negligible over all temperatures for



which lead does not desorb, a well defined interface is formed, without complications due to alloying or dissolution in the bulk. The Pb can be easily removed and deposited again. Like most semiconductor interfaces, the Pb/Ge(111) system shows interesting atomic and electronic structures and it has therefore been the subject of numerous investigations [69–92]. Here we focus on the disordering transition of a  $(\sqrt{3} \times \sqrt{3})R30^\circ$  reconstruction to a  $1 \times 1$  phase at  $\sim 180^\circ\text{C}$ .

Before studying a phase transition of an adsorbed layer, one should know the exact atomic structure of the phases above and below the transition. As a function of coverage there are two different room temperature  $(\sqrt{3} \times \sqrt{3})R30^\circ$  structures on Ge(111): a dilute  $\alpha$  phase and a dense  $\beta$  phase, see Fig. 4.1. The  $\alpha$  phase has a coverage of  $1/3$  monolayer (ML), where 1 ML is defined as one chemisorbed atom per top layer Ge atom of the unreconstructed, ideal Ge(111). The  $\alpha$  phase is well understood and consists of one atom per  $(\sqrt{3} \times \sqrt{3})R30^\circ$  unit cell chemisorbed on a  $T_4$  site on top of the second layer of Ge [72, 74, 75, 79]. The coverage and structure of the dense  $\beta$  phase, however, has been debated for many years.

The main controversy about the  $\beta$  phase is the saturation coverage. From Reflection High Energy Electron Diffraction (RHEED), X-ray scattering, and Low Energy Electron Diffraction (LEED) measurements a structural model has been proposed with a saturation coverage of  $4/3$  ML (four atoms per unit cell) [70–72, 77–79, 89]. This structure is essentially a 1% compressed close-packed Pb(111) layer rotated by  $30^\circ$  with respect to the underlying Ge lattice. Per unit cell, three Pb atoms occupy the bridge sites between  $T_4$  and  $T_1$  sites, with a small displacement to the  $T_1$  sites (therefore also called off-centered (OC)  $T_1$  sites), and one atom occupies an  $H_3$  site. Scanning Tunneling Microscopy (STM) experiments are consistent with a  $4/3$  ML structure, but here the Pb atoms were thought to be on OC  $T_4$  sites [83]. The  $4/3$  ML saturation coverage was also found in a first principles molecular dynamics study, where a “chain” model has been proposed [82].

Other LEED and STM measurements have reported that the saturation coverage for the  $\beta$  phase is 1 ML (three atoms per unit cell) [69, 84, 85]. Hwang and Golovchenko [84] derived this coverage with Rutherford backscattering. They proposed a model consisting of three Pb atoms per unit cell, which are displaced from the  $T_1$  sites to form trimers around the  $H_3$  sites of the Ge substrate. First principle calculations find that this trimer structure at 1 ML coverage is unstable [82]. An overview of the different models proposed is given by Franklin *et al.* [89] from which we can conclude that most evidence points to a  $4/3$  ML saturation coverage.

Using RHEED Ichikawa [70, 71] was the first to derive a phase diagram for Pb/Ge(111). Ichikawa reported that a Pb monolayer on the Ge(111) surface undergoes a solid to liquid phase transition at a temperature which depends critically

Pb ON GE(111)

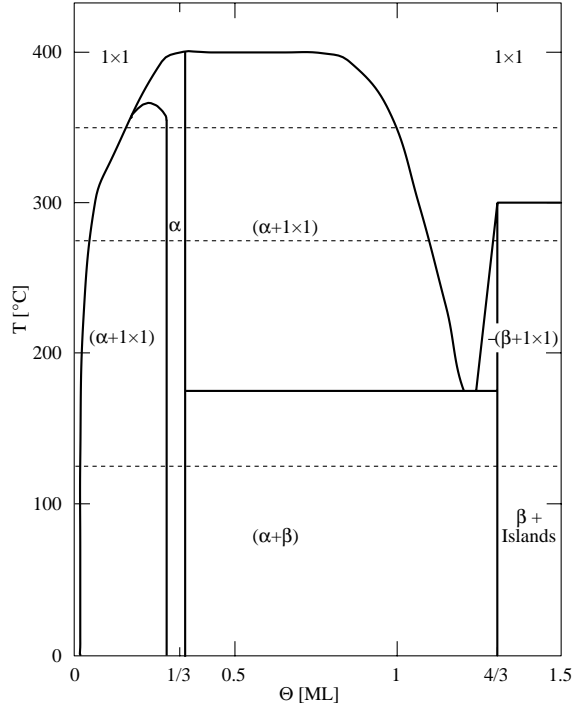


**Figure 4.1:** Phase diagram of Pb/Ge(111) proposed by Grey [76]. The dashed lines mark the different temperatures at which we monitored the fractional order ( $\frac{2}{3} \times \frac{2}{3} 0.1$ ) reflection during Pb deposition (see Fig. 4.2).

on the coverage going from 192°C to 333°C. This phase transition was thought to correspond to the melting of the Pb monolayer. Using LEED, Métois and Le Lay [69] found a reversible  $(\sqrt{3} \times \sqrt{3})R30^\circ$  to  $1 \times 1$  transition at 280°C, which they claimed is not an order-disorder transition, because of the sharpness of their  $1 \times 1$  LEED pattern at 300°C. LEED did not show any rings of diffuse scattering. Therefore, Métois and Le Lay describe it as a solid-solid structure change.

A thorough investigation of the phase diagram has been done by Grey [76], showing that below a coverage of  $4/3$  ML a low-temperature phase transition to the  $1 \times 1$  phase occurs around  $\sim 180^\circ\text{C}$ . Above  $4/3$  ML a high-temperature phase transition occurs around  $\sim 330^\circ\text{C}$ . For convenience, the phase diagram proposed by Grey is shown in Fig. 4.1.

Grey *et al.* [80] studied the phase transition from the  $\beta-(\sqrt{3} \times \sqrt{3})R30^\circ$  phase to the  $1 \times 1$  phase at a temperature of 180°C and a coverage of 1.25 ML. From their

experimental X-ray observation of a diffraction ring they concluded that the Pb forms a two-dimensional, modulated liquid. However, Hwang and Golovchenko [84, 85] proposed an alternative explanation for this phase on the basis of STM observations. They claim that the  $\beta$  phase breaks up into very small domains at the transition temperature of 180°C with the Pb atoms in a state of greatly agitated motion.

In order to resolve this controversy we have measured the intensity along crystal truncation rods (CTRs) [22] above and below the phase transition. These rods are tails of diffuse intensity connecting the bulk Bragg peaks in the direction perpendicular to the surface. The intensity along a CTR is given by the interference sum of the bulk and surface contribution. Such integer-order positions in reciprocal space are insensitive to the anti-phase disorder that Hwang and Golovchenko claim to be the origin of the phase transition at  $\sim 180^\circ\text{C}$ . If at this temperature only the domain size is changing, no change in the CTR intensity is expected. On the other hand, a transition to a two-dimensional liquid should have a profound effect on the CTRs.

## 4.2 Experimental

The conditions of the experiment described here are similar to those reported in chapters 2 and 3. The X-ray diffraction measurements were performed at station 9.4 of the Synchrotron Radiation Source, Daresbury Laboratory, United Kingdom [42]. Monochromatic X-rays with a wavelength  $\lambda$  of 0.92 Å (13.5 keV) were used, with both the primary and the diffracted beam collimated by slits. All data were taken with a constant outgoing angle of  $1^\circ$  and varying incoming angles, thereby keeping the detector resolution constant. The sample was mounted in an ultra-high vacuum chamber [43] coupled to a five-circle diffractometer [93]. A Knudsen effusion cell was used for Pb deposition at a rate of  $\sim 0.003$  ML/sec.

The polished single crystal Ge(111) sample ( $8 \times 8 \times 2$  mm<sup>3</sup>) had a miscut smaller than  $0.1^\circ$ . The sample was cleaned by repeated cycles of sputtering (600 eV Ar<sup>+</sup>, 10  $\mu\text{Amin}$ ) and annealing (700°C for 15 min).

Structure factors are obtained by dividing the measured intensity by the Lorentz factor, the polarization factor, an area correction factor, and taking the square root [46] (see chapter 2). The area correction factor for the variation of the X-ray footprint on the sample is calculated numerically by assuming a Gaussian beam profile with a FWHM of 2.1 mm in the horizontal and 1.6 mm in the vertical direction. The error in the individual structure factors was determined from the counting statistics. Symmetry equivalent reflections were measured as well, from which an estimate for the systematic error was derived [17], varying between 7 and

12% for the different data sets. Throughout this chapter we use the same primitive real-space lattice as in chapter 2, see Eq. 2.1. The germanium bulk lattice constant  $a_0 = 5.658 \text{ \AA}$ . The difference here is that the unit cell as defined by the lattice vectors  $\{\mathbf{a}_i\}$  encloses three bilayers with the ABC stacking of a diamond-type crystal. Each bilayer contains two atoms in a  $(1 \times 1)$  unit cell: at the positions  $\mathbf{r}_1 = 0$  and  $\mathbf{r}_2 = \frac{2}{3}\mathbf{a}_1 + \frac{1}{3}\mathbf{a}_2 + \frac{1}{12}\mathbf{a}_3$ . Each bilayer is shifted over a translation vector  $\mathbf{r} = \frac{2}{3}\mathbf{a}_1 + \frac{1}{3}\mathbf{a}_2 + \frac{1}{3}\mathbf{a}_3$ .

### 4.3 Results and discussion

#### 4.3.1 Saturation coverage of the $\beta$ phase

First we investigate the deposition of Pb on Ge(111). In Fig. 4.2 the intensity of the  $(hkl) = (\frac{2}{3} \frac{2}{3} 0.1)$  fractional order reflection that is sensitive to the  $(\sqrt{3} \times \sqrt{3})R30^\circ$  structure is shown during Pb deposition at three different substrate temperatures. These curves (marked by the dashed lines in Fig. 4.1) beautifully confirm the phase diagram as proposed by Grey [76]. At a substrate temperature of  $125^\circ\text{C}$  (Fig. 4.2(a)), well below the low-temperature phase transition, the intensity rises constantly after starting the Pb deposition. First the  $\alpha$  phase is formed. After a deposition of  $1/3$  ML this phase is completed and the  $\beta$  phase starts to form as well. Both phases have a  $(\sqrt{3} \times \sqrt{3})R30^\circ$  structure and therefore the transition from one to the other is not visible in this scan. Because of both the strong scattering of Pb atoms (compare  $Z_{\text{Pb}} = 82$  and  $Z_{\text{Ge}} = 32$ ) and the increase in domain size, the intensity rises quite dramatically. After the deposition we made a transverse in-plane scan of the  $(\frac{2}{3} \frac{2}{3} 0.1)$  reflection. By measuring the peak full width at half maximum  $\Delta Q_{\text{FWHM}}$  we can derive the correlation length  $L = 2/\Delta Q_{\text{FWHM}}$  [48]. For the deposition at  $125^\circ\text{C}$  we find a correlation length of  $1650 \text{ \AA}$ .

In Fig. 4.2(b), the same experiment is shown for a substrate temperature of  $275^\circ\text{C}$ , which is well above the low-temperature phase transition. From the intensity it is clear at which moment the  $\alpha$  and  $\beta$  phases are complete. First the intensity rises when the  $\alpha$  phase is formed. Since the  $\alpha$  phase is known to be completed after deposition of  $1/3$  ML, we can estimate from this figure at which moment we have deposited  $1/3$  ML. The arrow indicates this position, which is after 105 secs. After exactly four times this amount, 420 secs, the  $\beta$  phase is completed (second arrow). In between the intensity goes back to zero, because of the low-temperature phase transition around  $180^\circ\text{C}$  for a coverage just below  $4/3$  ML. Assuming that no desorption occurs, the  $\beta$  phase thus has a saturation coverage of  $4/3$  ML. From Fig. 4.2(b) it becomes clear that the phase transition to the  $1 \times 1$  phase critically depends on the coverage. Below  $4/3$  ML it occurs around  $\sim 180^\circ\text{C}$ , and above  $4/3$  ML around  $\sim 300^\circ\text{C}$ . Also here we measured a transverse in-plane scan of the  $(\frac{2}{3} \frac{2}{3} 0.1)$

CHAPTER IV

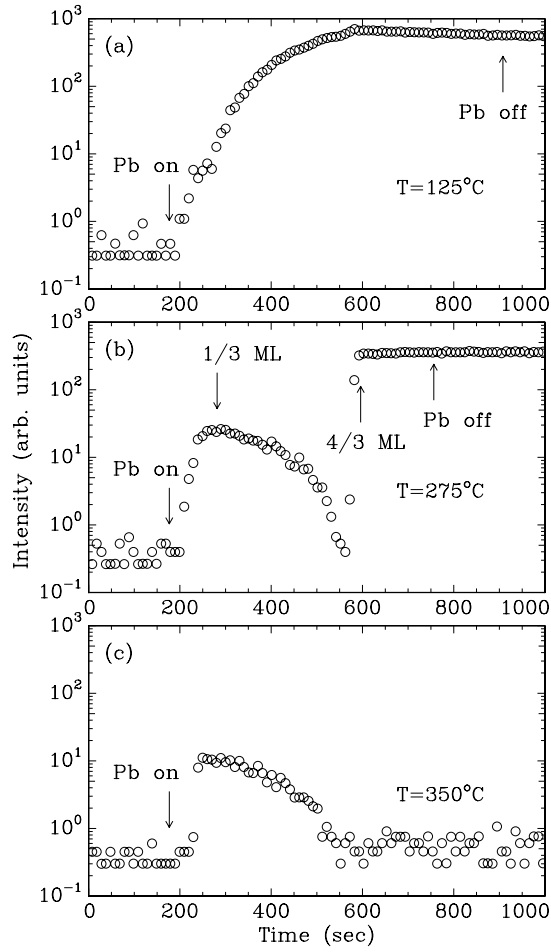


**Figure 4.2:** The  $(\frac{2}{3} \frac{2}{3} 0.1)$  fractional order reflection during Pb deposition at three different Ge(111) substrate temperatures. The arrows indicate the starting and stopping of the Pb deposition. In (b) the completion of the  $\alpha$  phase after 105 secs of deposition (1/3 ML) and the  $\beta$  phase after 420 secs (4/3 ML) are indicated by arrows as well.

reflection, for which we found a resolution limited  $\Delta Q_{\text{FWHM}} \cong 0.7 \cdot 10^{-3} \text{ \AA}^{-1}$ , which means the correlation length is larger than 2500 Å. The domains are thus exceptionally large. Note that the completion of the  $\beta$  phase coincides exactly with the break in the deposition curve shown in Fig. 4.2(a).

Pb deposition at 350°C is shown in Fig. 4.2(c). Only the  $\alpha$  phase is formed, because we are above the high-temperature phase transition. In the remainder of this chapter, we will look at the atomic structure of 1.25 ML of Pb below and above the phase transition at  $\sim 180^\circ\text{C}$ . The  $\beta$  phase is studied at a temperature of 125°C and the  $1 \times 1$  phase at 260°C. Note that the temperature values used here are not very accurate (absolute error is about 50°C), but that we can reproducibly locate the phase transitions with the help of Fig. 4.2.

#### 4.3.2 Atomic structure of the $\beta$ phase

In order to determine the atomic structure below and above the phase transition we measured two integer order CTRs, as well as a number of in-plane reflections. As a reference we measured these rods for the clean starting sample at room temperature as well. The clean Ge(111)- $c(2 \times 8)$  reconstruction has been studied before with surface X-ray diffraction [94,95]. Our data is consistent with the structural model of Van Silfhout *et al.* [95].

In Fig. 4.3 the measured structure factor amplitudes for the  $\beta$  phase along the (0 1) and (0 2) CTRs are shown together with model calculations as a function of perpendicular momentum transfer  $l$ , expressed in reciprocal lattice units (r.l.u.). We have started our analysis with the model proposed by Feidenhans'l *et al.* [72], where one Pb atom is placed on an  $H_3$  site, and the other three Pb atoms on the bridge sites between the  $T_1$  and  $T_4$  sites. One fitting parameter is used to allow these three atoms to move off-center to the  $T_1$  or  $T_4$  site. For the height of the Pb atoms, two fitting parameters were used for the two different sites ( $H_3$  and bridge site). With a global scaling parameter, a surface fraction parameter  $\theta$  (fraction of surface that adopts the model surface structure), and in-plane and out-of-plane Debye-Waller parameters  $B_{\text{par}}$  and  $B_{\text{perp}}$  for the Pb atoms, the total number of free fitting parameters used in our  $\chi^2$  minimization was 7. For the Ge atoms an isotropic Debye-Waller  $B$  parameter was fixed at the room temperature bulk value of  $0.58 \text{ \AA}^2$  [96]. All Ge atoms were fixed at bulk positions, because no significant improvement to the fit was found by allowing them to relax. The best-fit has a reduced  $\chi^2$  value of 1.3.

A schematic of the model structure is shown in Fig. 4.4 in (a) top and (b) side view. One Pb atom is positioned at a  $H_3$  site and three atoms are displaced from the bridge site towards the  $T_1$  sites, as indicated by the arrows. In (b) the distances

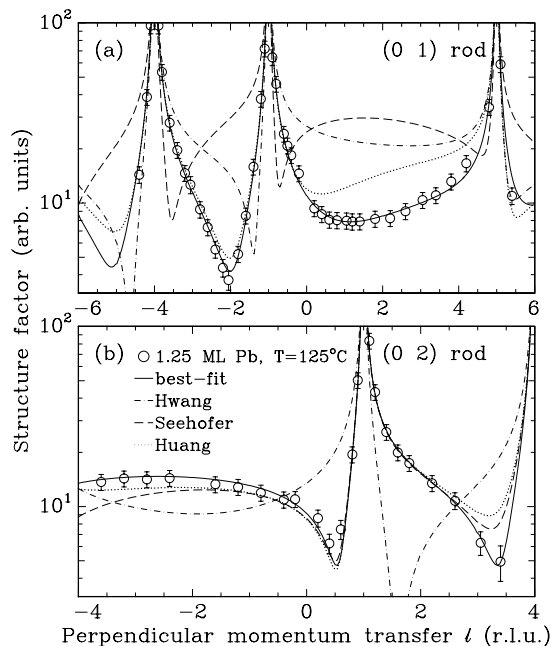


**Figure 4.3:** Structure factor amplitudes  $|F_{hkl}|$  along the (01) and (02) crystal truncation rods. Measured structure factors are indicated by open circles. The solid curve represents our best-fit model calculation. For comparison calculations for the models proposed by Hwang and Golovchenko [84] (dash-dotted), Seehofer et al. [83] (dashed), and Huang et al. [79] (dotted) are also shown.

between atoms and the Pb (covalent) radius are drawn to scale.

The solid curves in Fig. 4.3 show our best-fit model calculation. The fit parameters are shown in Table 4.1 together with the atomic coordinates. From the surface fraction parameter  $\theta$  we find a coverage of  $0.89 \times 4/3 = 1.19$  ML, which is close to our estimated deposition of 1.25 ML. Since the coverage is below  $4/3$  ML, it could be that one of the sites is less occupied. However, by taking a surface fraction 1 and fitting the occupancies of the  $H_3$  and OC  $T_1$  sites the reduced  $\chi^2$  went up from 1.3 to 1.8. Thus the  $(\sqrt{3} \times \sqrt{3})R30^\circ$  domains appear to have locally a coverage of  $4/3$  ML.

We find that the bridge atoms are displaced towards the  $T_1$  site (OC  $T_1$ ) by an amount of  $0.39 \text{ \AA}$  from the bridge center, in agreement with earlier X-ray ( $0.35 \text{ \AA}$ ) and LEED measurements ( $0.43 \text{ \AA}$ ) [72, 79]. We find a large in-plane Debye-Waller factor of 6.3. The parameter  $B$  is related to the mean-square thermal

PB ON GE(111)

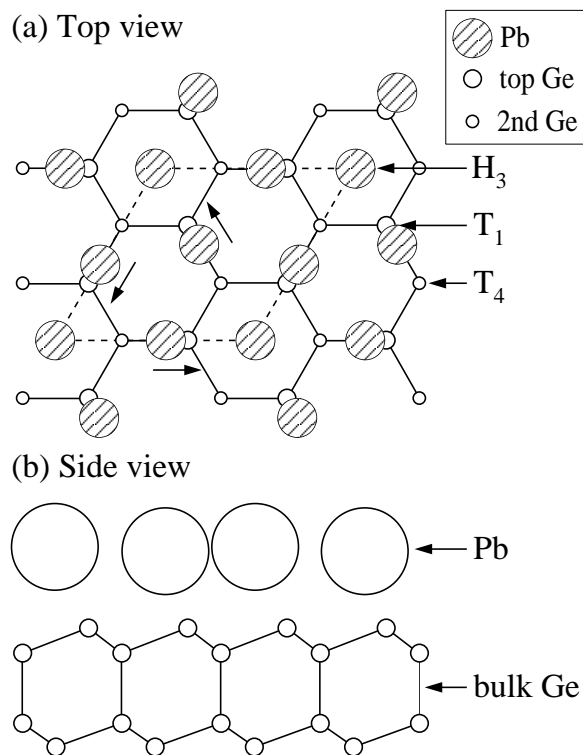


**Figure 4.4:** Schematic projections of our structural model in (a) top view and (b) side view. The  $(\sqrt{3} \times \sqrt{3})R30^\circ$  unit cell is indicated by the dashed lines. One Pb atom is positioned at a  $H_3$  site and three atoms are displaced from the bridge site towards the  $T_1$  sites, as indicated by the arrows. In (b) the distances between atoms and the Pb (covalent) radius are drawn to scale.



**Table 4.1:** Best-fit parameters and atomic coordinates for the structural model for the  $\beta$  phase. The atom positions in the surface unit cell are given by  $\mathbf{r} = x\mathbf{a}_1 + y\mathbf{a}_2 + z\mathbf{a}_3$ , with  $\{\mathbf{a}_i\}$  the fundamental translation vectors as defined in Eq. (2.1). Fixed values are indicated by an asterisk (\*).

Fit parameter	
$\theta$ surface fraction	0.89(2)
OC $T_1$ displacement ( $\text{\AA}$ )	0.39(4)
Height $H_3$ atom ( $\text{\AA}$ )	2.88(17)
Height OC $T_1$ atoms ( $\text{\AA}$ )	2.76(4)
Debye-Waller $B_{\text{par}}$ ( $\text{\AA}^2$ )	6.3
Debye-Waller $B_{\text{perp}}$ ( $\text{\AA}^2$ )	1

Atom	$x$	$y$	$z$
$H_3$ Pb	0.333*	0.667*	0.377
OC $T_1$ Pb	-0.223	1.223	0.365
OC $T_1$ Pb	1.447	1.223	0.365
OC $T_1$ Pb	0.777	1.554	0.365
Top Ge	0.667*	0.333*	0.083*
2nd Ge	0.000*	0.000*	0.000*

vibration amplitude  $\langle u^2 \rangle$  by  $B = 8\pi^2 \langle u^2 \rangle$ . We have thus an in-plane root mean squared (rms) thermal vibration amplitude of 0.28  $\text{\AA}$ . The perpendicular Debye-Waller parameter remains small, but our fit is not significantly affected by this parameter. The total amplitude  $\langle u^2 \rangle = \langle u_{\text{par}}^2 \rangle + \langle u_{\text{perp}}^2 \rangle$  corresponds to a Debye temperature of the Pb monolayer  $T_D \sim 55$  K [97]. The bulk Pb Debye temperature is  $T_D = 81$  K. Even lower values, however, for a Pb monolayer were found by photo emission measurements ( $T_D = 41$  K) [73], X-ray standing wave measurements ( $T_D = 32$  K) [89], and predicted by molecular dynamics ( $T_D = 34$  K) [86].

There has been some debate about the height of the overlayer Pb atoms with respect to the top layer Ge atoms [98]. Huang *et al.* [79] find for these vertical distances 2.22  $\text{\AA}$  and 2.70  $\text{\AA}$  for the lower (at  $H_3$ ) and upper (between  $T_1$  and  $T_4$ ) Pb layers, respectively. Dev *et al.* [77] find for these values 1.55 and 2.85  $\text{\AA}$ . In our analysis these distances are 2.88  $\text{\AA}$  and 2.76  $\text{\AA}$ . So in our determination the atoms on the  $H_3$  sites are the upper atoms. This was also found by Seehofer *et al.* [83] who estimated the relative height difference between the  $H_3$  and OC  $T_1$  to

be 0.15 Å, which comes close to our value of 0.12 Å. However, our error bar on the height of the  $H_3$  atom is rather large (0.17 Å) so we cannot be very definitive about this issue. In *ab initio* molecular dynamic calculations [82] it was found that the Pb atoms all have about the same height,  $\sim 2.7$  Å above the Ge surface.

In earlier X-ray measurements no out-of-plane positions were given [72], but our in-plane atomic coordinates are in agreement with these measurements as well as with the LEED measurements of Huang *et al.* [79]. As mentioned above, however, our model gives other height parameters for the Pb atoms. The dotted line in Fig. 4.3 shows a calculation for the model of Huang *et al.* Especially for the positive part of the (0 1) CTR the predicted distribution differs significantly from our measured structure factors. The model proposed by Seehofer *et al.* [83] agrees with ours on the out-of-plane coordinates, but differs in the way the bridge atoms are placed. In their model these Pb atoms occupy OC  $T_4$  sites, instead of OC  $T_1$  sites. This corresponds to changing the sign of the in-plane displacement in our model. Then we obtain the dashed curve, which is clearly not consistent with our data. From our measurements shown in Fig. 4.2, we have already concluded that models favoring three atoms per unit cell can be excluded. From our CTR measurements this is confirmed when we compare our data with the model proposed by Hwang and Golovchenko [84], that consists of a trimer with the  $T_1$  Pb atoms displaced towards the  $H_3$  sites by 0.3 Å (dash-dotted curve).

The models of Seehofer and of Hwang and Golovchenko are based on STM measurements. In a later paper Seehofer *et al.* [88] have demonstrated that the  $\beta$  phase has a rather complex appearance in STM images that depends on both the bias voltage and the tunneling current. Depending on the tunneling parameters they have observed one, three, or four protrusions per  $(\sqrt{3} \times \sqrt{3})R30^\circ$  unit cell. By comparing the results with the closely related incommensurate phase at a slightly higher Pb coverage, they identified both substrate- and adsorbate-induced features and therefore ruled out that the pattern with three protrusions per unit cell, as seen by Hwang and Golovchenko, matches the arrangement of the adsorbed Pb atoms. Their measurements illustrate the fact that it is generally not possible to obtain reliable structural information on the basis of STM data alone.

#### 4.3.3 $1 \times 1$ phase: a two-dimensional solid or liquid?

For the same Pb coverage, we have heated the substrate to 260°C, well above the transition temperature to the  $1 \times 1$  phase. We have confirmed the observation of Grey *et al.* [80] that a diffraction ring appears, characteristic of a two-dimensional liquid phase. Radial scans perpendicular to this ring in the directions  $[hk]=[21]$ ,  $[32]$ ,  $[41]$ , and  $[11]$  are shown in Fig. 4.5. Although the count rates are very low

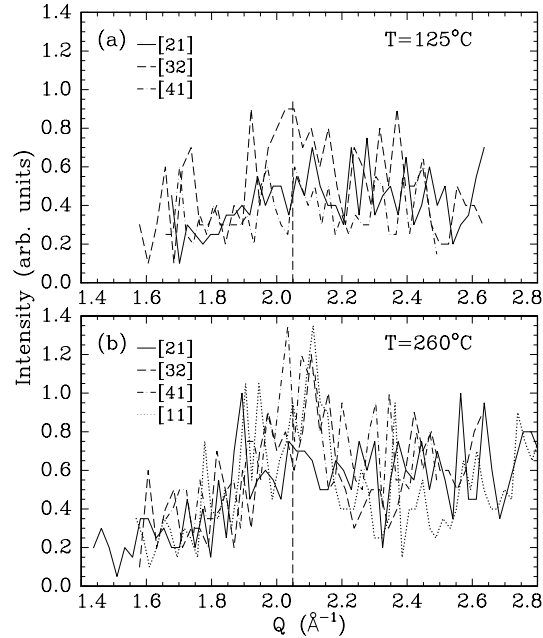


**Figure 4.5:** Radial scans in the directions  $[hk]=[21]$ ,  $[32]$ ,  $[41]$ , and  $[11]$  (a) below and (b) above the phase transition. In (a) the  $[11]$  direction is omitted, because of the huge  $(\frac{2}{3}, \frac{2}{3})$  peak at  $Q = 2.09 \text{ \AA}^{-1}$ . The dashed line marks  $Q = 2.05 \text{ \AA}^{-1}$  where Grey *et al.* [80] found the maximum of the diffraction ring.

in these scans (the beam conditions were not optimal), at a temperature of  $260^\circ\text{C}$  the appearance of the ring of diffuse scattering is visible (Fig. 4.5(b)). It is hard to obtain the peak width and position of the ring, but the peak position we find is very close to the position reported by Grey *et al.* at  $Q = 2.05 \text{ \AA}^{-1}$ , which is marked by the dashed line in the figure. This diffuse ring of scattering is thus evidence that the Pb monolayer behaves indeed partly as a two-dimensional liquid. For a genuine two-dimensional liquid, the value of  $2.05 \text{ \AA}^{-1}$  corresponds to a nearest-neighbour distance of  $3.42 \text{ \AA}$  [76].

Figure 4.6 shows the distribution of measured structure factors along the  $(01)$  and  $(02)$  rods for this phase (filled circles) together with the data for the  $\beta$  phase (open circles). The effect of the phase transition on the  $(01)$  rod is hardly visible, while the change in the  $(02)$  rod is more dramatic. The dashed curve is a calculation for a simple bulk terminated Ge(111) crystal (unreconstructed) and for the  $(02)$  rod the measured structure factors follow this curve quite well. This rod is very

PB ON GE(111)

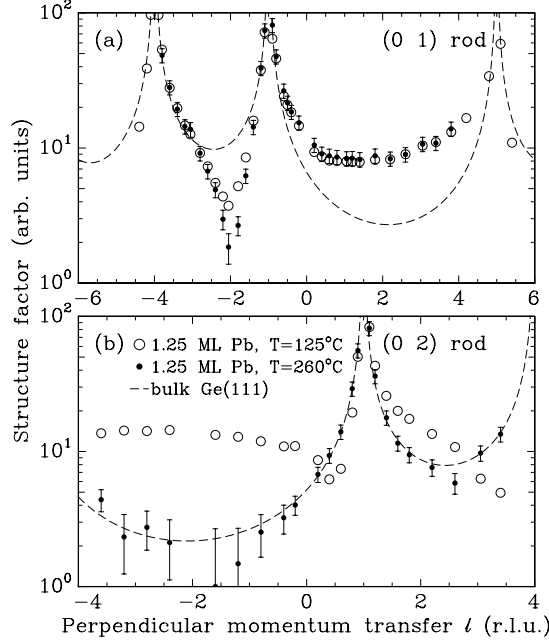


**Figure 4.6:** Structure factor amplitudes  $|F_{hki}|$  along the (01) and (02) crystal truncation rods. Measured structure factors are indicated by open circles for the  $\beta$  phase at 125° C and filled circles represent the data for the  $1 \times 1$  phase at 260° C. The dashed curves give calculations for the flat bulk terminated Ge(111) surface.

sensitive to the  $(\sqrt{3} \times \sqrt{3})R30^\circ$  structure and above the transition there seems to be no ordered Pb visible at all. Apparently, the Pb layer has both liquid-like and solid-like properties. Next we will quantify this by discussing various models of the high-temperature phase.

There are two types of models. One with a  $(\sqrt{3} \times \sqrt{3})R30^\circ$  unit cell and vanishing correlation length, the other with a genuine  $(1 \times 1)$  cell. The liquid ring or the vanishing correlation lengths point to a high mobility. For this reason, we assume the surface to be uniform (i.e., the surface fraction equals 1) and allow for coverages below  $4/3$  ML by varying the occupancies of the different possible sites. We start our analysis by taking a  $1 \times 1$  unit cell and allowing the Pb atoms to occupy any of the three high symmetry sites  $T_1$ ,  $T_4$ , or  $H_3$  on the surface. When we do our fit procedure we find that the  $T_4$  site is not significantly occupied (less than 15%) and therefore we do not consider this position any further. This is consistent with the low-temperature model and the conclusions of others. When

**Table 4.2:** Best-fit parameters, reduced  $\chi^2$  values, and Pb nearest-neighbour distances for the structural models for the high-temperature  $1 \times 1$  phase of 1.25 ML Pb on Ge(111). Fixed values are indicated by an asterisk (\*). The  $1 \times 1$  model is equivalent to the model proposed by Franklin et al. [89] (see text).

Fit parameter	$1 \times 1$	$\beta$ model	$\beta$ -fit	Trimer
In-plane displacement (Å)	0*	0.39*	0.83	0.50
Height $H_3$ atom (Å)	2.90	2.88*	2.91	2.93
Height (OC) $T_1$ atoms (Å)	2.70	2.76*	2.72	2.76
$H_3$ occupancy	0.29	0.59	1*	0.51
(OC) $T_1$ occupancies	0.89	1	1*	0.59
Debye-Waller $B_{\text{par}}$ (Å <sup>2</sup> )	35	24	35	6.3*
Debye-Waller $B_{\text{perp}}$ (Å <sup>2</sup> )	1	1	1	1*
$\chi^2$	0.3	2.4	0.3	0.7
Pb nearest-neighbour distance (Å)	2.32	3.07	2.65	1.82

we allow only the  $T_1$  and  $H_3$  sites we find in our best-fit that the  $T_1$  site is 89% occupied and the  $H_3$  site 29% (see Table 4.2, column ‘ $1 \times 1$ ’ and Fig. 4.7 solid curve). This corresponds to a total coverage of 1.17 ML, consistent with our estimated Pb coverage of 1.25 ML. In molecular dynamic simulations done by Ancilotto *et al.* [86] it was proposed that the Pb overlayer becomes diffusive above the phase transition, but that the Pb atoms still spend an important fraction close to symmetry sites. The average time spent close to a  $T_1$  site was 58%, close to a  $T_4$  site 14%, and close to a  $H_3$  site 28%. They showed that the diffusion in the overlayer is not purely two-dimensional liquid-like, but has lattice gas-like features. These calculations were done for a higher temperature, and Ancilotto *et al.* speculate that for temperatures around  $\sim 200^\circ\text{C}$  the non-liquid-like features should be comparatively more important. This is consistent with our observations.

Hwang and Golovchenko [84] have proposed that at the phase transition the long range order of the  $(\sqrt{3} \times \sqrt{3})R30^\circ$  reconstruction is destroyed by thermal fluctuations. The  $(\sqrt{3} \times \sqrt{3})R30^\circ$  domains become very small, but in principle the structure stays the same. Since we have shown that their trimer model is not consistent with our data we have tried to fit our high-temperature data with our structural model for the  $\beta$  phase. In its extreme form, this model would predict the  $(\sqrt{3} \times \sqrt{3})R30^\circ$  reflections to disappear while the integer-order ones remain constant, because these are insensitive to the anti-phase domain disorder. The data

PB ON GE(111)

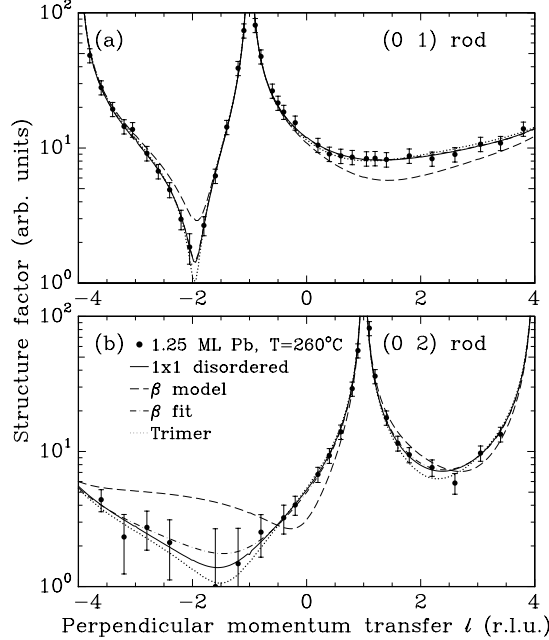


**Figure 4.7:** Structure factor amplitudes  $|F_{hki}|$  along the (01) and (02) crystal truncation rods at a substrate temperature of 260°C. Measured structure factors are indicated by filled circles. The curves are model calculations (see text).

in Fig. 4.6 show that this is not true. So instead we tried to fit the high-temperature data keeping the displacements fixed and varying only the occupancies and Debye-Waller parameters. We do not find a good fit to our data in this way (see Table 4.2, column ‘ $\beta$  model’ and Fig. 4.7 dashed curve).

Thus during the phase transition, some of the structural parameters vary. If we fit the displacements in the  $\beta$  phase model we obtain a fit to our data that is as good as the  $1 \times 1$ -fit (see Table 4.2, column ‘ $\beta$ -fit’ and Fig. 4.7 dash-dotted curve). The OC  $T_1$  atoms are displaced much closer to the  $T_1$  sites than in the low-temperature  $\beta$  phase. If the in-plane displacement equals 1.15 Å, the atoms are exactly on  $T_1$  sites. This is the model proposed by Franklin *et al.* [89], who suggest that at the phase transition the symmetry of the ideal Ge(111) surface is thus restored. For the integer-order rods we can measure, this model gives the same results as the  $1 \times 1$  model, because for these rods one site out of three that is fully occupied in a  $(\sqrt{3} \times \sqrt{3})R30^\circ$  unit cell is equivalent to all sites with a 1/3 occupancy.

The in-plane Debye-Waller parameter  $B_{\text{par}}$  of 35 corresponds to an in-plane

rms vibrational amplitude of 0.67 Å. Franklin *et al.* find an in-plane rms vibrational amplitude of 0.60 Å. These vibrational amplitudes are huge, although consistent with the greatly agitated state of the Pb atoms seen in STM pictures [84] and with molecular dynamics calculations [86]. Unfortunately, we only have two complete CTRs, so we cannot observe the effect of the Debye-Waller factor over a large range in parallel momentum transfer. To see whether it is possible to find a good fit to our data without the large vibrational amplitudes, we tried several models while fixing the Debye-Waller parameters to the values found for the  $\beta$  phase. Note that from the Debye temperature  $T_D \sim 55$  K mentioned above, the temperature rise from 125°C to 260°C should result in an increase of  $\sqrt{\langle u^2 \rangle} = 0.30$  Å to 0.35 Å. The only model for which we obtain a good fit to our data, is a model where trimers of atoms on  $T_1$  sites are displaced towards the  $H_3$  center by 0.5 Å. This model is similar to that proposed by Hwang and Golovchenko [84], except that we also have a Pb atom in the middle of the trimer at the  $H_3$  site. The occupancies found for the two sites are 0.51 and 0.59 for the  $H_3$  and  $T_1$  sites, respectively (see Table 4.2, column ‘Trimer’ and Fig. 4.7 dash-dotted curve) corresponding to a visible coverage of only 0.76 ML. The remaining 0.5 ML do not follow the Ge(111) lattice, and could therefore be liquid-like.

The models for the high-temperature phase all predict surprisingly small nearest-neighbour distances for the Pb atoms compared to the covalent distance of 2.94 Å. The  $1 \times 1$  (and Franklin) model gives 2.32 Å, the  $\beta$ -fit model 2.65 Å, and the trimer model 1.82 Å. Differences in height cannot significantly change this. From our data we know for sure that the  $1 \times 1$  phase has a different structure than the  $\beta$  phase which *does* have the expected bond distance. The bond length argument thus favours the  $\beta$ -fit model and essentially rules out the trimer model. The  $1 \times 1$  model yields a 20% decrease in nearest-neighbour distance, which seems unlikely. A large change in bond distance is only expected if the phase transition simultaneously modifies the electronic structure.

On the basis of our data we cannot fully decide whether the  $1 \times 1$  phase consists of very small domains of  $(\sqrt{3} \times \sqrt{3})R30^\circ$  structure as proposed by Hwang and Golovchenko [84], or of an ordered phase where all Pb atoms occupy high symmetry sites with a high diffusion between these sites, as was proposed by Ancilotto *et al.* [86]. When the domain size becomes very small, a large fraction of the Pb atoms is located at domain boundaries. This may lead to additional relaxations that we only model on average in the structure of our model unit cells.

The bond lengths favour the  $\beta$ -fit model, in which a snap shot would closely resemble the low-temperature structure shown in Fig. 4.4. The atoms on OC  $T_1$  sites are in the  $\beta$ -fit model closer to the  $T_1$  sites (see ‘solid’ Pb atoms in Fig. 4.8), which could well be caused by the fact that on average the number of

PB ON GE(111)

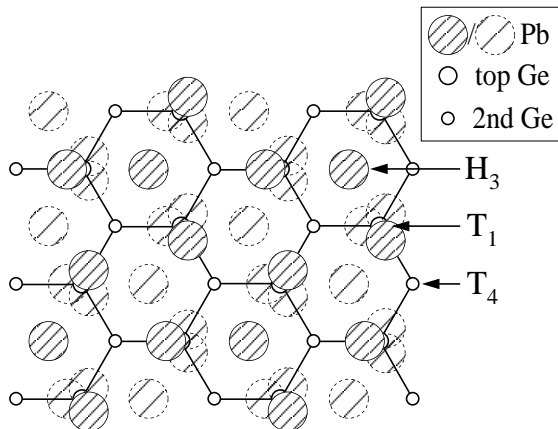


**Figure 4.8:** Schematic top view of our ‘ $\beta$ -fit’ structural model. The ‘solid’ Pb atoms are placed in one  $(\sqrt{3} \times \sqrt{3})R30^\circ$  domain and can be considered as a snapshot of the surface. The ‘dashed’ Pb atoms indicate the positions where the Pb atoms on average can also be found forming other domains (see text).

nearest neighbours is reduced compared to the saturation coverage. Size hindrance prevents the atoms to occupy the exact  $T_1$  sites. Because of diffusion, all atoms rapidly change positions and on average all  $H_3$  sites will have the same occupancy, while all three equivalent OC  $T_1$  sites will also be equally occupied (see ‘dashed’ Pb atoms in Fig. 4.8). These occupancies are less than  $1/3$  since the atoms can also be found on non-lattice sites, as evidenced by the liquid ring. The fact that the phase transition occurs for a coverage of  $1.25$  ML is consistent with this picture and points to a *lattice* gas model. When more Pb atoms are added more sites are occupied and there is no room for diffusion left. Therefore, at a coverage of  $4/3$  ML the Pb adlayer is forced to the  $(\sqrt{3} \times \sqrt{3})R30^\circ$  reconstruction. This reconstruction melts at a temperature of  $\sim 330^\circ\text{C}$ , which is close to the bulk melting point of Pb of  $327.5^\circ\text{C}$ .

#### 4.4 Conclusions

We have determined that the  $\beta$  phase has four atoms per unit cell and therefore the saturation coverage is  $4/3$  ML. Our model, consisting of three Pb atoms on OC  $T_1$  sites and one Pb atom on a  $H_3$  site, is consistent with other LEED and X-ray scattering studies.

The phase transition to the  $1 \times 1$  phase was found to be an order-order transition and disagrees with a strictly two-dimensional liquid interpretation. To explain



## CHAPTER IV

our measurements large in-plane thermal vibration amplitudes are required. The picture that emerges is that of rapidly diffusing atoms that spend a significant fraction of their time close to lattice sites. More theoretical work is necessary to reconcile this with the simultaneous observation of liquid diffraction rings.

## V

### Surface atomic structure of KDP crystals in aqueous solution: an explanation of the growth shape

*With this study on KDP, we present an interface atomic structure determination of a crystal in contact with its growth solution. Using X-ray diffraction at a third generation synchrotron radiation source, the structure of both the  $\{101\}$  and  $\{100\}$  faces has been determined. We found that the  $\{101\}$  faces are terminated by a layer of  $K^+$  ions and not by  $H_2PO_4^-$  groups, resolving a long-standing issue that could not be predicted by theory. This result leads to an atomic-scale explanation of the influence of metal impurities on the macroscopic growth morphology.*

#### 5.1 Introduction

The crystallographic theory of Hartman and Perdok aims to predict the morphology of growing crystals [99, 100]. With this theory it is often possible to predict from a known crystal structure the facets, referred to by the Miller indices  $(hkl)$ , that will dominate the crystal form. These faces are the so-called F (flat) faces. Since the growth of crystals takes place at the crystal-solution interface, one expects the atomic structure at this boundary to play a primary role in the composition, growth, and morphology of the crystal. Hardly any atomic-scale experimental data exist to verify this. Hartman-Perdok theory does not take into account possible relaxations or reconstructions at the crystal surface, nor the influence of the solution on the interface, but is still remarkably successful. A problem in the theory is, however, that often more than one surface termination is possible for a given orientation  $(hkl)$  and that it is impossible to predict which of the alternatives will control the crystal growth.

With the appearance of third-generation synchrotron radiation sources it is now possible to look accurately at the atomic structure of these interfaces with X-rays. Surface X-ray diffraction has proven to be a very powerful technique for studying interfaces at an atomic scale [17] and it is one of the few surface science techniques that does not require a vacuum environment. X-ray scattering studies have been

done on liquid-liquid [101] and liquid-solid interfaces [5, 102]. In particular, surfaces of electrodes in an electrolyte solution have received attention [103, 104]. Recently the first *in situ* X-ray diffraction studies on crystals in their growth solution have been reported [105, 106]. Here we report the determination of the atomic positions at such an interface.

## 5.2 KDP

The system we study is a potassium dihydrogen phosphate ( $\text{KH}_2\text{PO}_4$ , KDP) crystal in its aqueous growth solution. KDP finds widespread use as a frequency doubler in laser applications and has been studied in great detail [107]. Hartman-Perdok theory predicts that the pyramidal faces  $\{101\}$  and the prismatic faces  $\{100\}$  of KDP are flat in solution [108, 109]. This is in agreement with the observed habit of these crystals: they exist as a tetragonal prism consisting of four faces of the form  $\{100\}$  terminated by two opposing tetragonal pyramids consisting of  $\{101\}$  faces (see Fig. 5.1(a)). For the prismatic  $\{100\}$  faces exactly one surface termination is predicted. For the pyramidal  $\{101\}$  faces, however, two alternative terminations are theoretically possible. One has the negative  $\text{H}_2\text{PO}_4^-$  groups on the outside, and the other the positive  $\text{K}^+$  ions (see Fig. 5.1(b)).

For these pyramidal faces the question arises whether growth kinetics is determined by single layers, with alternately  $\text{K}^+$  and  $\text{H}_2\text{PO}_4^-$  on top, or double layers. The single layers are strongly polar. The difference in polarity of the layers and, especially, the differences in size and polarizability of the ions will result in a different surface free energy. If the polarity of the surface layers does not play a role in the step kinetics, the surface would consist of both  $\text{K}^+$  and  $\text{H}_2\text{PO}_4^-$ -terminated layers. From the surface morphology observed with interference-contrast reflection microscopy and considering the symmetry of the crystal [109, 110] it can be concluded that the surface is bounded by only one of the polar layers. This is confirmed by atomic force microscopy measurements where the height of the steps on the  $\{101\}$  face is always found to correspond to the thickness of double layers [111].

The question remains which of the two alternative layers is the one at the surface. We have determined the surface structure of both the  $\{101\}$  and  $\{100\}$  surfaces in solution by measuring the distribution of diffracted intensities along so-called crystal truncation rods (CTRs) [22]. These CTRs are tails of diffuse intensity connecting the bulk Bragg peaks in the direction perpendicular to the surface and show the interference between bulk and surface structure. Parallel to the interface the aqueous solution will be very weakly ordered [104]. We have only measured CTRs which have an in-plane component (i.e. not the specular rod),

SURFACE STRUCTURE OF KDP IN SOLUTION

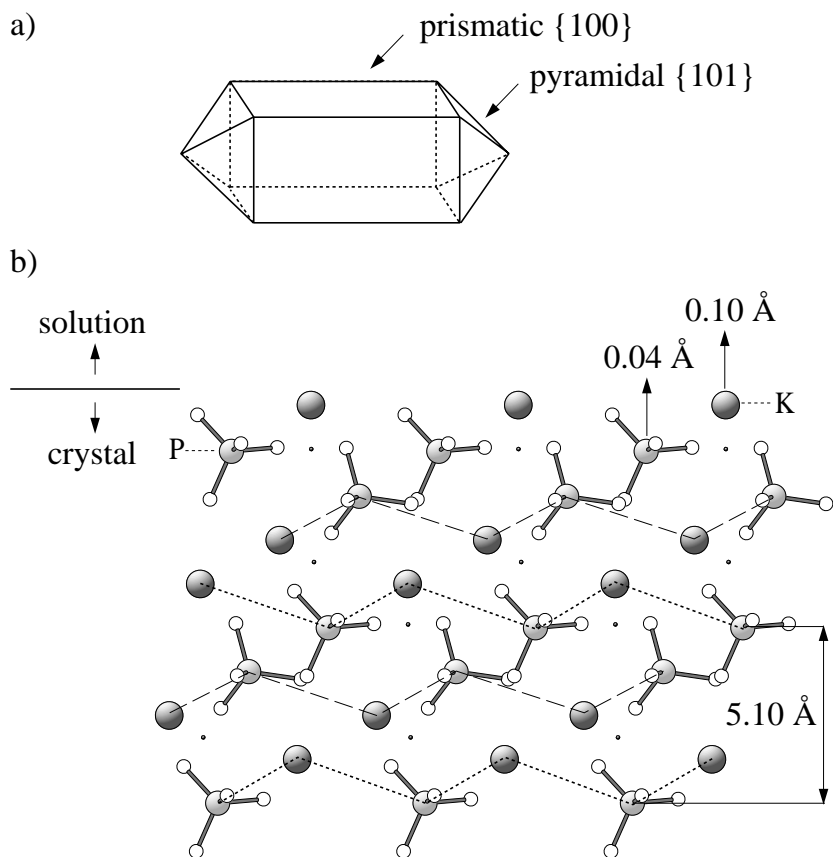


**Figure 5.1:** (a) Growth habit of a KDP crystal with the prismatic and pyramidal faces indicated. (b) Schematic side view of the pyramidal face, KDP(101), projected on the (111) plane. The big circles are the potassium atoms while the  $\text{PO}_4$  groups are depicted as a circle for the phosphorus atom connected by sticks to the four neighbouring oxygen atoms, shown as small white circles. The dots give the positions of the hydrogen atoms between two oxygen atoms. The layers with the  $\text{K}^+$  ions on top are schematically indicated by the dotted lines and the layers with the  $\text{H}_2\text{PO}_4^-$  groups on top by the dashed lines. Arrows indicate the relaxations in the topmost layer as determined from fitting the experimental data.

for which the intensity distribution will hardly be influenced by the solution and mainly depends on the crystal surface atomic structure.

### 5.3 Experimental

For KDP(101) we use a unit cell of which the primitive lattice vectors  $\{\mathbf{a}_i\}$  can be expressed in the conventional tetragonal lattice vectors as

$$\mathbf{a}_1 = \frac{1}{2} [1\ 1\ 1]_{\text{tetragonal}}, \quad \mathbf{a}_2 = \frac{1}{2} [\bar{1}\ 1\ \bar{1}]_{\text{tetragonal}}, \quad \mathbf{a}_3 = [\bar{1}\ 0\ 1]_{\text{tetragonal}}, \quad (5.1)$$

with

$$|\mathbf{a}_1| = |\mathbf{a}_2| = \sqrt{\frac{1}{2}a^2 + \frac{1}{4}c^2}, \quad |\mathbf{a}_3| = \sqrt{a^2 + c^2},$$

with  $a = 7.45 \text{ \AA}$  and  $c = 6.97 \text{ \AA}$  the lattice constants of bulk KDP [112]. The corresponding reciprocal lattice vectors  $\{\mathbf{b}_i\}$  are defined by  $\mathbf{a}_i \cdot \mathbf{b}_j = 2\pi\delta_{ij}$ . The momentum transfer vector  $\mathbf{Q}$ , which is the difference between the wavevectors of the incident and scattered X-rays, can be denoted by the diffraction indices  $(hkl)$  in reciprocal space:

$$\mathbf{Q} = h\mathbf{b}_1 + k\mathbf{b}_2 + l\mathbf{b}_3. \quad (5.2)$$

For CTRs, which are labelled by  $(hk)$ , the indices  $h$  and  $k$  have integer values, whereas  $l$  is unconstrained and refers to the component of  $\mathbf{Q}$  perpendicular to the surface. The Bragg peaks occur for integer values of  $l$ , which is in reciprocal lattice units (r.l.u.) of  $0.62 \text{ \AA}^{-1}$ . For KDP(100) we use a unit cell in which the primitive lattice vectors are

$$\mathbf{a}_1 = [0\ 1\ 0]_{\text{tetragonal}}, \quad \mathbf{a}_2 = [0\ 0\ 1]_{\text{tetragonal}}, \quad \mathbf{a}_3 = [1\ 0\ 0]_{\text{tetragonal}}. \quad (5.3)$$

These definitions result in  $1 \text{ r.l.u.} = 0.84 \text{ \AA}^{-1}$  along the  $l$  direction.

The measurements were performed at the TROIKA open undulator beamline (ID10A) of the European Synchrotron Radiation Facility (ESRF) in Grenoble, France [113]. These data were fully consistent with earlier measurements (with a lower accuracy) performed at the Synchrotron Radiation Source in Daresbury, U.K. The crystals were mounted in a growth chamber made of polycarbonate, consisting of an outer heating bath kept at a constant temperature by a thermostat. In the inner chamber, the crystal is mounted in an environment of a saturated aqueous KDP solution. The structure determination was carried out at a temperature of  $22^\circ\text{C}$ . The incoming and outgoing X-ray beams penetrate through a thin Mylar

foil ( $6\ \mu\text{m}$ ) which can be pushed close to the crystal surface, leaving a thin layer of saturated solution between the crystal and the foil (thickness  $\sim 10\ \mu\text{m}$ ). The crystal growth chamber is mounted onto a horizontal diffractometer (i.e., the scattering plane is horizontal). The beryllium monochromator was set to select a wavelength of  $0.73\ \text{\AA}$  ( $17.0\ \text{keV}$ ) using the (002) reflection, leading to approximately  $10^{12}$  photons/sec in a  $2 \times 1\ \text{mm}^2$  spot. This wavelength was chosen as an optimum in the signal to background ratio. For smaller wavelengths the diffuse background scattering from the bulk crystal rapidly goes up, while for larger wavelengths attenuation in the solution (and the Mylar) becomes too strong. For a typical surface reflection the signal-to-background ratio is about 10%, but for weak reflections this can be as small as 2%. The possibility to do accurate measurements under these circumstances has enormously increased with the availability of high-intensity and high-energy X-ray beams from third-generation synchrotron radiation sources such as the ESRF. The KDP crystals are sufficiently flat to measure the CTR intensity far from the Bragg peaks, where the surface sensitivity is highest.

#### 5.4 Results

Figure 5.2 shows measured structure factor amplitudes along the (10) CTR for KDP(101). The integrated intensity at each point  $l$  is determined by rotating the crystal about the surface normal and measuring the number of diffracted photons. The measured integrated intensities are corrected for the active sample area, the Lorentz factor, the polarization factor, the rod interception [46], and the absorption due to the different pathways of the outgoing beam through the liquid and the Mylar foil. Structure factor amplitudes are obtained by taking the square root of the corrected integrated intensity. The values for the negative  $l$  part of the rod are obtained according to Friedel's rule by inverting the structure factor distribution along the positive  $(hk) = (\bar{1}0)$  rod through the origin of reciprocal space.

The dotted curve in Fig. 5.2 gives the expected values for a bulk  $\text{K}^+$ -terminated surface and the dashed curve is a calculation for a surface terminated by the  $\text{H}_2\text{PO}_4^-$  groups. It is immediately clear that the surface must be  $\text{K}^+$ -terminated. Our data confirm the conclusion of De Yoreo, Land, and Dair [111] that the surface does not contain both  $\text{K}^+$  and  $\text{H}_2\text{PO}_4^-$ -terminated parts. An even better description of the data is obtained when small out-of-plane relaxations of the top layer are allowed and when a simple model for surface roughness on an atomic scale is included [22]. Least-squares fitting of the data then results into a model that yields the solid line. A schematic side view of this model is shown in Fig. 5.1(b). The fit procedure was performed using the complete data set which also includes the (1 1) and (2 1) CTRs (not shown). In the best fit model the K atoms in the top layer relax outwards by an

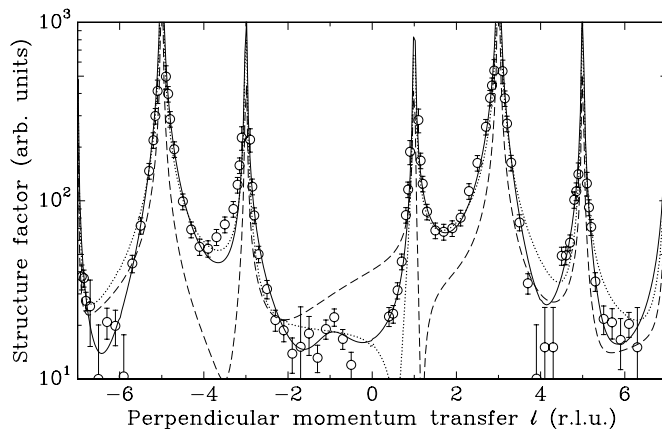


**Figure 5.2:** Structure factor amplitudes along the (10) crystal truncation rod for KDP(101) as a function of the diffraction index  $l$  which is expressed in reciprocal lattice units. The dotted line is a calculation for a bulk  $K^+$ -terminated surface, the dashed curve for a  $H_2PO_4^-$ -terminated one. The solid line is the best fit starting from a  $K^+$ -terminated surface and allowing the  $K^+$  ions and the  $H_2PO_4^-$  groups in the top layer to relax.

amount of  $0.10 \pm 0.05 \text{ \AA}$  and the  $H_2PO_4$  groups by  $0.04 \pm 0.05 \text{ \AA}$ . The root mean square (rms) roughness was estimated to be  $2.0 \pm 0.5 \text{ \AA}$  measured over a lateral length scale of a few thousand  $\text{\AA}$ .

In a similar fashion, data were obtained on KDP(100). In Fig. 5.3, structure factor amplitudes along the (12) CTR are shown. For this surface only one bulk crystal termination is possible. The solid curve is a fit to the data using as fit parameters only a scale factor and a roughness parameter. For the fit the full data set was used that also contains parts of the (21) and (30) CTRs (not shown). The rms roughness found for this surface is  $1.2 \pm 0.3 \text{ \AA}$ . A schematic side view of the structure model is shown in Fig. 5.4. The data set on this face was much smaller than on KDP(101), and therefore we can only conclude that if there are relaxations of the top layer atoms, these are smaller than  $0.1 \text{ \AA}$ .

## 5.5 Discussion and Conclusions

Having established the atomic structure of both faces, we can now understand why small traces of trivalent metal ion impurities like  $Fe^{3+}$  or  $Cr^{3+}$  block the growth of the prismatic faces, but affect the growth of the pyramidal faces to a much lesser extent [109, 114, 115]. When such impurities are present the crystals become more

## SURFACE STRUCTURE OF KDP IN SOLUTION

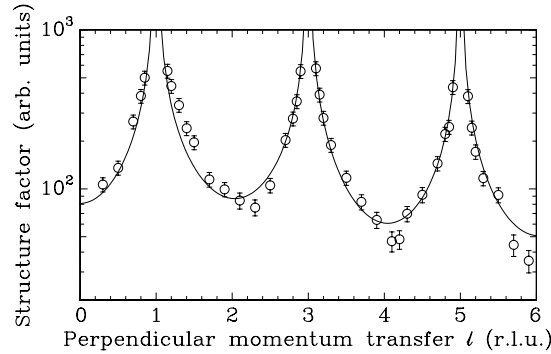


**Figure 5.3:** Structure factor amplitudes along the  $(12)$  crystal truncation rod of  $KDP(100)$ . The solid curve is a calculation for a bulk terminated crystal with a rms roughness of  $1.2 \text{ \AA}$ .

elongated in the direction of the pyramids. Looking at Figs. 5.1 and 5.4, it is seen that the pyramidal face has the  $K^+$  ions on the outside of the crystal for the best fit model. The prismatic face has both the positive  $K^+$  ions and the negative  $H_2PO_4^-$  at the interface. This result supports the hypothesis of Dam *et al.* [109] that the attachment of cations to the pyramidal faces is less favourable than to the prismatic faces. With only  $K^+$  ions on the surface of the crystal, metal impurities like  $Fe^{3+}$  and  $Cr^{3+}$  ions will experience a large barrier to adsorption onto the positively charged face. On the prismatic faces, however, these ions can adsorb easily, and small amounts of  $Fe^{3+}$  or  $Cr^{3+}$  will already block the growth.

For the pyramidal growth sectors the segregation coefficient of trivalent metal ions has been found to be much lower than for the prismatic sectors [116]. Similar differences in impurity segregation on crystallographically dissimilar faces [117] as well as dissimilar steps on a single face [118] have been observed in other crystal systems grown from solutions. Paquette and Reader [118] attributed such inhomogeneities in  $CaCO_3$  to differences in kink site geometries, the implication being that incorporation kinetics at steps controlled the impurity content. We now have shown that for KDP a different mechanism is active, since the impurity content in the pyramidal sectors of the crystal is limited by adsorption kinetics on the terraces rather than incorporation kinetics at the steps.

Our results thus present an atomic-scale explanation for the influence of impurities on the macroscopic growth morphology of KDP. At the same time the possibility of determining the interface structure of a crystal in its growth solution is an important step towards the development of more sophisticated crystal growth



CHAPTER V

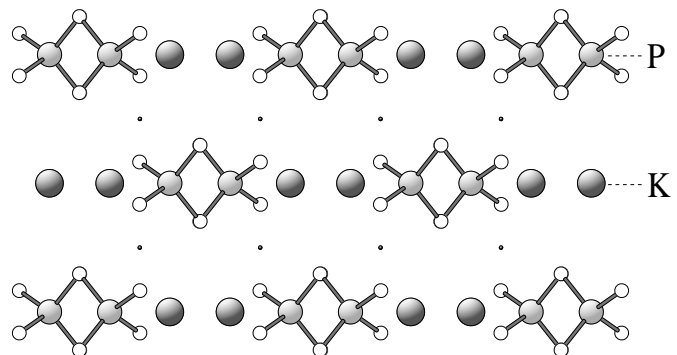


**Figure 5.4:** The prismatic face  $KDP(100)$  projected on the  $(010)$  plane. Here only one termination is possible.

theories. The atomic structure at the solid-liquid interface, including relaxations or even reconstructions, is important for controlling the distribution and concentration of the molecules in the solution. An intriguing implication of the present work is that a strongly polarized crystal surface will affect the structure of the near-surface liquid layer. Presumably there is a charge compensating layer of solution adjacent to the surface and this must strongly affect the adsorption kinetics for the solute ions. In addition, the fact that the  $(101)$  surface is positively charged suggests that the reaction rate (desolvation and attachment) for anions is much greater than for cations. More experiments and theory are necessary to further increase our understanding of these phenomena.

## VI

### **X-ray diffraction studies of KDP crystal surfaces**

*We have studied the surface atomic structure of KDP crystals using X-ray scattering. These crystals are grown from an aqueous solution and we have done measurements both ex situ and in situ. The ex situ measurements are performed in vacuum and in air. In order to be able to do in situ measurements, we have designed and built a crystal growth chamber which is compatible with X-ray diffraction experiments. The surface atomic structure of the two natural existing faces of KDP has been determined. Preliminary results are presented of measurements during growth. Furthermore, the influence of metal impurities on the atomic structure of the growing interface was examined.*

#### **6.1 Introduction**

Crystal growth from solution is a very important process that is used from the laboratory to the industrial scale. An innumerable number of organic and inorganic crystals is grown in this fashion. Recently it has become clear that in crystal growth from solution the interface region plays a much more important role than originally thought [1]. Both the liquid and the solid part of the interface are important, but as a first step we have studied the crystal structure.

Structural information on the immersed solid is most relevant for crystal growth from solution or melt, and a range of topics is of interest: the relaxations in the top layers, the influence of impurities on the morphology, and, for multi-component crystals, the termination at the surface. For crystal growth it is also very important to know whether the interface is atomically flat or rough, because the growth mode will be entirely different for these two cases [119]. Which of the two situations occurs can be predicted by a theory that has integrated the statistical-mechanical Ising models with the crystallographic morphological theory of Hartman and Perdok [99].

There is a lack of information on the atomic-scale interface structure, because most surface science techniques require a vacuum environment and cannot be

applied to solid-liquid interfaces. Exceptions are Scanning Tunneling Microscopy (STM), Atomic Force Microscopy (AFM), and X-ray diffraction. STM/AFM is mostly used for morphological studies. Most of the X-ray experiments reported to date on solid-liquid interfaces have not been on bulk crystal growth, but on electrochemical deposition of thin layers of one metal on another [120]. With an appropriate choice of materials (strongly scattering overlayers), this type of work is “relatively” easy.

With the appearance of third-generation synchrotron radiation sources it is now possible to look accurately at the atomic structure of interfaces of crystals in their growth solution with X-rays. We have recently reported the determination of the atomic positions at such an interface [121].

The overruling difficulty compared to studies in vacuum is the increase in background due to the scattering from the solution, which can easily drown the weak signal from the surface. The signal to noise ratio can be improved by (1) carefully setting the slits in order to illuminate as little solution as possible, (2) using a light solution in combination with a high- $Z$  crystal, and (3) using a high-quality crystal that produces very sharp diffraction spots. In practice it will of course not always be possible to optimize all three conditions at the same time.

The system we study is the ferroelectric crystal potassium dihydrogen phosphate (KDP,  $\text{KH}_2\text{PO}_4$ ) in its aqueous growth solution. We have chosen KDP because of its high crystal quality (no mosaic spread) and because it is a very interesting crystal both from a technological and a fundamental point of view. KDP crystals are the primary material used in devices controlling laser radiation, its modulation, frequency conversion and scanning. They are manufactured in larger quantities than the total sum of all other crystals used in quantum electronics. Therefore, KDP-family crystals have been studied in great detail [107].

In a previously reported X-ray-diffraction study [121] we have shown that in solution the  $\{101\}$  faces are terminated by a layer of  $\text{K}^+$  ions and not by  $\text{H}_2\text{PO}_4^-$  groups, resolving a long standing issue that could not be predicted by theory. From this result we have proposed an atomic-scale explanation of the influence of metal impurities on the macroscopic growth morphology. It has been known for a long time that small traces of trivalent metal ion impurities like  $\text{Fe}^{3+}$  or  $\text{Cr}^{3+}$  block the growth of the  $\{100\}$  or prismatic faces, but affect the growth of the  $\{101\}$  or pyramidal faces to a much lesser extent [109, 114, 115]. From the atomic structure found for the two faces in solution, we can explain why impurities experience a larger barrier to attach to the  $\{101\}$  faces than to the  $\{100\}$  faces, and therefore block the growth on the latter ones [121]. One possibility is that the Fe forms a (partly) ordered adlayer. It is also possible that only minute fractions of impurities pin growing step edges and therefore stop the growth [10]. In the case of the

prismatic  $\{100\}$  faces, there is a so-called “dead area”, a range of supersaturations over which no growth occurs. It is known that the addition of impurities leads to a larger dead area, and it is even possible that the entire dead area effect is due to impurities that are present in even the purest solutions. Impurities have a much smaller effect on the pyramidal  $\{101\}$  faces, and no dead area has been reported. Nevertheless, small morphological differences have been observed using optical microscopy [114].

In this chapter we will describe in more detail the experiments which lead to the result described in chapter 5. Readers who are only interested in the main conclusions are referred to that chapter. We present some of the experimental details here because experiments of this type are new and require a different optimization than the familiar vacuum experiments. Before the *in situ* measurements were done, we first investigated the KDP surfaces in air and in vacuum. The experimental set up, with which the *in situ* measurements were done, will be described. Furthermore, we present the first results of experiments in which we tried to look at the solid-liquid interface during growth, with and without the addition of iron impurities.

## 6.2 Experimental

The KDP crystals used were grown at Lawrence Livermore National Laboratory (LLNL). At LLNL one is preparing for the National Ignition Facility (NIF) for inertial fusion experiments. In power optics devices, powerful laser beams are being transmitted and even a slight absorption or scattering of light in a crystal may destroy the material or lead to an unacceptable distortion of the radiation characteristics. For the lasers of NIF, about 800 high-quality KDP crystals are required with a size of  $37 \times 37 \times 1 \text{ cm}^3$  — a fantastic size for artificial single crystals. Nevertheless it is possible to grow such crystals.

Some of the measurements were done on crystals cut from bigger single crystals. The crystals were cut using a diamond blade saw and an ethylene glycol solution. After cutting, the crystals were “etched” in ultra-clean water. This etching consists of simply putting the crystals into pure water for a few seconds. By doing this the surface layer of the crystal dissolves and large regular etch pits are seen when these crystals are observed under an optical microscope. However, Atomic Force Microscopy (AFM) measurements show that big flat terraces exist on these surfaces, see Fig. 6.1. The terraces typically have widths of the order of 1000 to 10000 Å and are large enough to allow X-ray diffraction measurements. The step heights for the (101) face shown in the figure are all 5.1 Å, which corresponds to half the height of the unit cell in the direction perpendicular to the surface. These are therefore all monomolecular steps, as was also seen in *in situ* AFM measurements done by

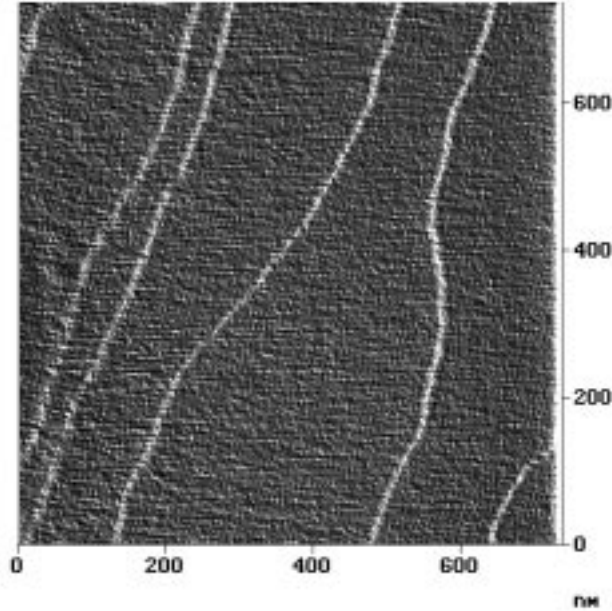


**Figure 6.1:** AFM image of  $KDP(101)$  crystal after an “etch” in  $H_2O$ .

De Yoreo *et al.* [111].

The measurements were performed at four different beamlines at three different synchrotron radiation sources. The first test experiments were done in our ultra-high vacuum set up at beamline 9.4 at the Synchrotron Radiation Source (SRS) in Daresbury, UK [42]. The *ex situ* experiments were continued at beamline BW2 at the synchrotron radiation source at HASYLAB, Germany [122]. The *in situ* measurements were started again in Daresbury, and continued at the TROIKA undulator beamline ID10A of the European Synchrotron Radiation Facility (ESRF) in Grenoble, France [113]. The last experiments, where we have tried out a new set up to look at *in situ* growth, were done at the SEXAFS and Standing Waves undulator beamline ID32, also at the ESRF. Only at the TROIKA beamline the surface of the crystal is positioned horizontally onto the diffractometer. At all the other beamlines the crystal surface is vertical.

Integrated intensities at various values of the diffraction index  $l$  along a crystal truncation rod are determined by rotating the crystal about the surface normal and measuring the number of diffracted photons. To obtain the structure factor amplitudes from the integrated intensities, different geometrical and resolution corrections are necessary. For the experiments done in Daresbury expressions for

these corrections are given in chapter 2. For the other measurements the incoming angle of the X-ray beam was fixed to a value close to  $1^\circ$  and therefore no incoming beam profile correction is needed. However, the difference in scattering geometry means one other correction is needed that was not mentioned in chapter 2: a rod interception correction. This correction factor originates from the fact that the integration range along the rod is not constant for different reflections. All corrections needed (and used) for the different geometries in this chapter are extensively described by Vlieg [46].

The momentum transfer vector  $\mathbf{Q}$  is the difference between the outgoing and the incoming wavevector of the X-ray beam:

$$\mathbf{Q} = \mathbf{k}_{\text{out}} - \mathbf{k}_{\text{in}}, \quad (6.1)$$

with  $|\mathbf{k}_{\text{out}}| = |\mathbf{k}_{\text{in}}| = 2\pi/\lambda$ . In reciprocal space  $\mathbf{Q} = (hkl)$ , where  $h$ ,  $k$ , and  $l$  are the coordinates along the axes  $\mathbf{b}_1$ ,  $\mathbf{b}_2$ , and  $\mathbf{b}_3$  of the reciprocal lattice. The convention commonly used is that  $h$  and  $k$  are the in-plane Miller indices, while  $l$  is along the out-of-plane direction. To make sure that  $l$  is perpendicular to the surface, we have to choose the lattice vectors  $\mathbf{a}_1$  and  $\mathbf{a}_2$  of our primitive unit cell in the surface plane as we did in Eq. 5.1 for KDP(101). Since the corresponding reciprocal lattice vectors  $\{\mathbf{b}_i\}$  are defined by  $\mathbf{a}_i \cdot \mathbf{b}_j = 2\pi\delta_{ij}$ ,  $\mathbf{b}_3$  is proportional to the cross product of  $\mathbf{a}_1$  and  $\mathbf{a}_2$  and therefore perpendicular to the surface plane. In the case of KDP(101) the lattice parameters  $\{\mathbf{a}_i\}$  as defined in Eq. 5.1 are not orthogonal. The angle  $\alpha_1$  between  $\mathbf{a}_2$  and  $\mathbf{a}_3$  is  $86.93^\circ$ . The other two angles are  $\alpha_2 = 93.07^\circ$  (between  $\mathbf{a}_1$  and  $\mathbf{a}_3$ ) and  $\alpha_3 = 107.73^\circ$  (between  $\mathbf{a}_1$  and  $\mathbf{a}_2$ ). The corresponding angles in reciprocal space between the  $\{\mathbf{b}_i\}$  are  $\beta_1 = 92.24^\circ$ ,  $\beta_2 = 87.76^\circ$ , and  $\beta_3 = 72.39^\circ$ . Normally in surface X-ray diffraction measurements “in-plane” data are taken with small out-of-plane momentum transfer, e.g.  $l = 0.1$ . Since for the case of KDP(101) the  $(hk)$  plane makes an angle with the real surface plane, for some values of  $h$  and  $k$  it is possible to measure at  $l = 0$ .

In order to label the reflections for the measurements on KDP(100), we use the unit cell lattice vectors  $\{\mathbf{a}_i\}$  as defined in Eq. 5.3, which *are* orthogonal. So in that case the terms in-plane and out-of-plane have their normal meaning.

### 6.3 In situ set up

In order to determine the surface atomic structure of KDP crystals in their growth solution a crystal chamber has been designed and built. A schematic side view of this chamber is shown in Fig. 6.2(a). The growth chamber is cylindrically symmetric and is made of polycarbonate. It consists of two separate compartments. An outer heating bath is kept at a constant temperature by flowing water through a

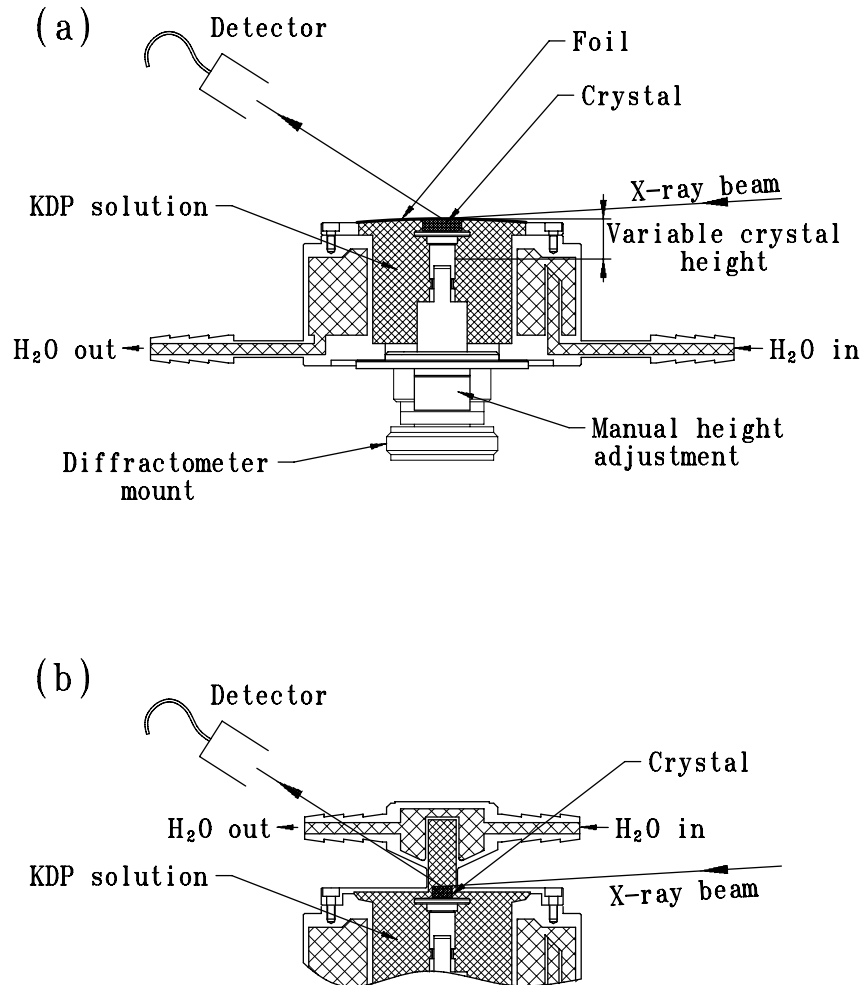


**Figure 6.2:** Side view of the crystal chamber. The chamber is made of polycarbonate and cylindrical in shape. In (a) the chamber is shown in reflection geometry, which was used for the experiments in Daresbury and on the TROIKA beamline at the ESRF. (b) shows the chamber with a transmission geometry top plate, used for the experiments at ID32.

X-RAY DIFFRACTION STUDIES OF KDP CRYSTAL SURFACES

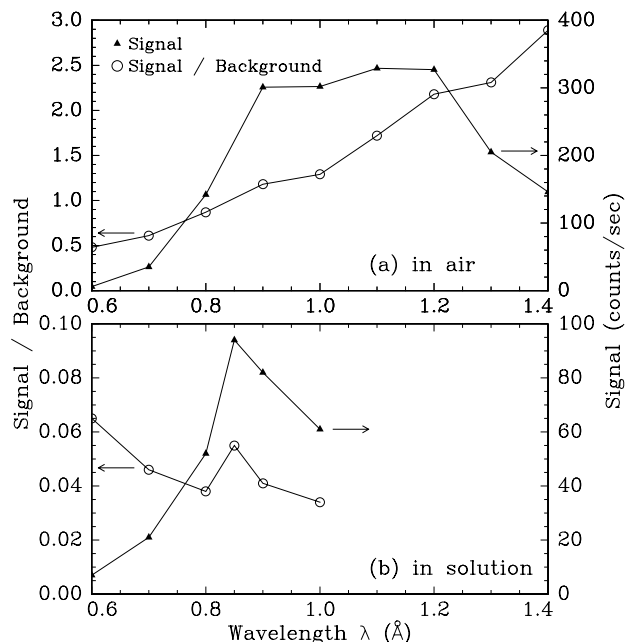


**Figure 6.3:** The (2 1 0.7) reflection measured on KDP(101) for different wavelengths in (a) air and (b) saturated KDP solution at 22° C. The open circles give the signal to background ratio and the filled triangles the peak height.

thermostat. The crystal is mounted in the inner chamber, which can be filled with saturated aqueous KDP solution.

In Daresbury the growth chamber was mounted on a five-circle diffractometer with the surface normal horizontal. First we did measurements on KDP(101) without the solution. To find an optimum wavelength to do our experiment we measured the (2 1 0.7) reflection as a function of the X-ray wavelength, using an incoming angle of 1°. The signal to background ratio and peak signal are shown in Fig. 6.3(a). The signal to background ratio (open circles) keeps rising with increasing wavelength. This is expected, since for larger wavelengths (lower energy) less of the bulk crystal is illuminated which results in less background scattering. The wiggler beamline gives the most intense radiation for wavelengths between 0.8 and 1.2 Å as is seen from the peak signal of this reflection (filled triangles). If we would measure in air, the best wavelength to use would thus be 1.2 Å.

After aligning the crystal, we can retract the crystal manually and put a foil on



CHAPTER VI

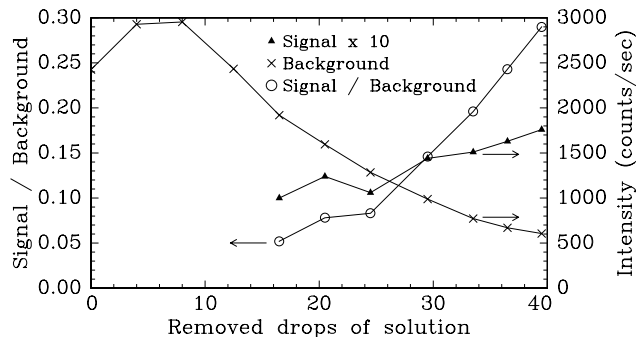


**Figure 6.4:** Signal to background ratio and signal and background intensities of the (2 1 0.7) reflection while removing saturated solution. The signal intensity is multiplied by a factor 10 to put it on the same scale as the background intensity.

top of the chamber. This foil is tightened with a ring around the chamber top, and made water proof by a viton seal. Now the chamber can be filled with saturated KDP solution. Different foils were tested for attenuation and the amount of extra background scattering. We did not find much difference between the different foils like polyethylene, propylene and Mylar, but the last one is the strongest and was therefore used to minimize the chance of leaking.

The solution was made to have a saturation temperature of 22 °C and the thermostat was set at this temperature. After letting the solution into the crystal chamber, the system can equilibrate before moving the crystal back to the original position. This can be done quite accurately, because we were always able to easily find back our crystallographic alignment. Because of the solution pressure the foil is pushed outwards a bit and leaves a lot of solution between crystal and foil. To become able to measure anything from the surface this amount of solution has to be reduced. We found that the best way to do this is by letting out drops of solution, thus creating a little under pressure. By this method the foil is nicely pushed against the sample.

We again measured the (2 1 0.7) reflection with different wavelengths using the same geometry. The signal to background ratio and peak signal are shown in Fig. 6.3(b). First of all, note that the signal to background ratio has gone down by more than a factor 10. For the wavelengths probed the signal to background ratio goes down from 0.07 to 0.03 going from 0.6 Å to 1.0 Å. At a wavelength of 1.0 Å the absorption in the liquid is really significant. At 0.8 Å we have only little intensity (see Fig. 6.3(a)), so we selected a wavelength  $\lambda = 0.85 \text{ \AA}$  (14.6 keV) for these experiments.

## X-RAY DIFFRACTION STUDIES OF KDP CRYSTAL SURFACES

To improve the signal to background ratio, we let out more drops of solution to make the liquid layer between foil and crystal thinner. We could easily follow this process by monitoring the (2 1 0.7) reflection while removing drops of solution. This is shown in Fig. 6.4. Because the incoming angle is small ( $1^\circ$ ), even the background signal cannot reach the detector when there is too much liquid. Therefore the background signal first goes up, before it decreases (crosses). The signal (filled triangles) is increasing after the layer of liquid is thin enough not to attenuate the X-rays too much.

We measured the  $1/e$  penetration depth of X-rays with a wavelength of  $0.85 \text{ \AA}$  in saturated KDP solution to be 2.4 mm. Mylar has a penetration depth for this wavelength of  $\sim 7$  mm. From the measurements shown in Fig. 6.4, and comparing the intensities to what we found without solution, we can estimate the thickness of the liquid layer between the crystal and the foil. The first time a signal is found (after removing 17 drops) the amount of liquid between crystal and foil is estimated to be of the order of  $\sim 100 \mu\text{m}$ . During the experiment this was  $\sim 10 \mu\text{m}$ .

The set up shown in Fig. 6.2(a) and used for the equilibrium structure determination described in chapter 5, is not really appropriate for growth experiments. The liquid layer on top of the surface is too thin. When the crystal grows, the saturation level of the solution will locally change because mass transportation is too slow. Besides, since there is no temperature stabilization on the foil side, gradients in temperature will easily occur. For these reasons a new top part was designed and built to make experiments possible in a transmission geometry. A schematic of this design is shown in Fig. 6.2(b). The top is again made out of polycarbonate and it consists of a small cylinder (diameter 1 cm, wall thickness of 0.5 mm) which is kept at constant temperature by the same thermostat as the bottom chamber. In this geometry there is a cylindrical column of solution above the surface. This transmission geometry was used for our experiment done at beamline ID32 at the ESRF. The crystals used were cut circular (diameter 7 mm, thickness 1 mm) in order to have solution flow between the cylindrical column above the sample and the “reservoir” of saturated solution below the sample. A disadvantage of this set up is that the X-rays have to penetrate through the walls of the cylinder, and, more importantly, have to go through 1 cm of saturated KDP solution. Therefore a higher photon energy is needed. At ID32 it is rather easy to change the X-ray energy and we could optimize it quite well. We found that an energy of 21 keV ( $0.59 \text{ \AA}$ ) gives the best signal to background ratio.

#### 6.4 Ex situ results

Before doing *in situ* experiments in the crystal growth chamber we have studied the surface structure of the  $\{101\}$  and  $\{100\}$  faces in air and vacuum. The first test experiments were done on KDP(101) in ultra-high vacuum at the SRS in Daresbury. These tests confirmed that KDP crystals are of very high quality with no mosaic spread. Here we also did some measurements on optically polished crystals, which turned out to be too rough on the X-ray length scale to be usable. These crystals in addition had very big miscuts of about  $2\text{-}4^\circ$  from the ideal (101) plane.

At the synchrotron radiation source at HASYLAB full data sets were taken on “dry” as-grown KDP crystal surfaces. For the X-ray wavelength used (1.38 Å, 9.0 keV), there is a lot of background scattering from the air. The signal to noise ratio could be improved by a factor ten by putting a graphite cap around the sample which could be evacuated. The results for 6 different CTRs are shown in Fig. 6.5. The solid curves represent calculations for a bulk  $\text{K}^+$ -terminated surface, the dashed curves for a  $\text{H}_2\text{PO}_4^-$ -terminated one.

After we measured this complete data set, we tried to see whether there was any effect on the sample by removing the vacuum and we measured the (2 1) rod while the sample was in air (see Fig. 6.6, triangles). No significant differences are seen in comparison with the earlier measurements in vacuum (circles). The measurements were done on a naturally grown (101) surface of a small crystal that had been in stock for quite some time, while no surface preparation was done. Therefore, we also took some measurements after etching the sample with pure water (+ symbols in Fig. 6.6). The intensity seems to be significantly higher. Unfortunately, we only measured the positive  $l$  part of the CTR in this case.

During the measurements in vacuum we constantly monitored the (1 1 0.5) and (2 0 2.3) reflections, to see whether there was any change in intensity. And indeed we found that in approximately 20 hours the structure factor amplitude decreased by 15% for the (1 1 0.5) reflection, and by 25% for the (2 0 2.3) reflection. While we were measuring the same surface in air, the (1 1 0.5) reflection hardly changed. The (2 0 2.3) reflection, however, went up in amplitude by 40% in 10 hours. After the water etch, the (1 1 0.5) reflection was back at the starting level and the (2 0 2.3) went up another 25%. From these observations we must conclude that in vacuum the surface quality decreases. Therefore, the data depicted in Fig. 6.5 are not accurate enough to find out whether there are surface relaxations. However, comparing the data with the calculations for the two possible terminations, we can conclude that the solid curve for  $\text{K}^+$ -termination describes our data best.

Another sample, which was grown in our own laboratory gave the results shown by the crosses in Fig. 6.6. This sample was measured in vacuum, and again the

X-RAY DIFFRACTION STUDIES OF KDP CRYSTAL SURFACES

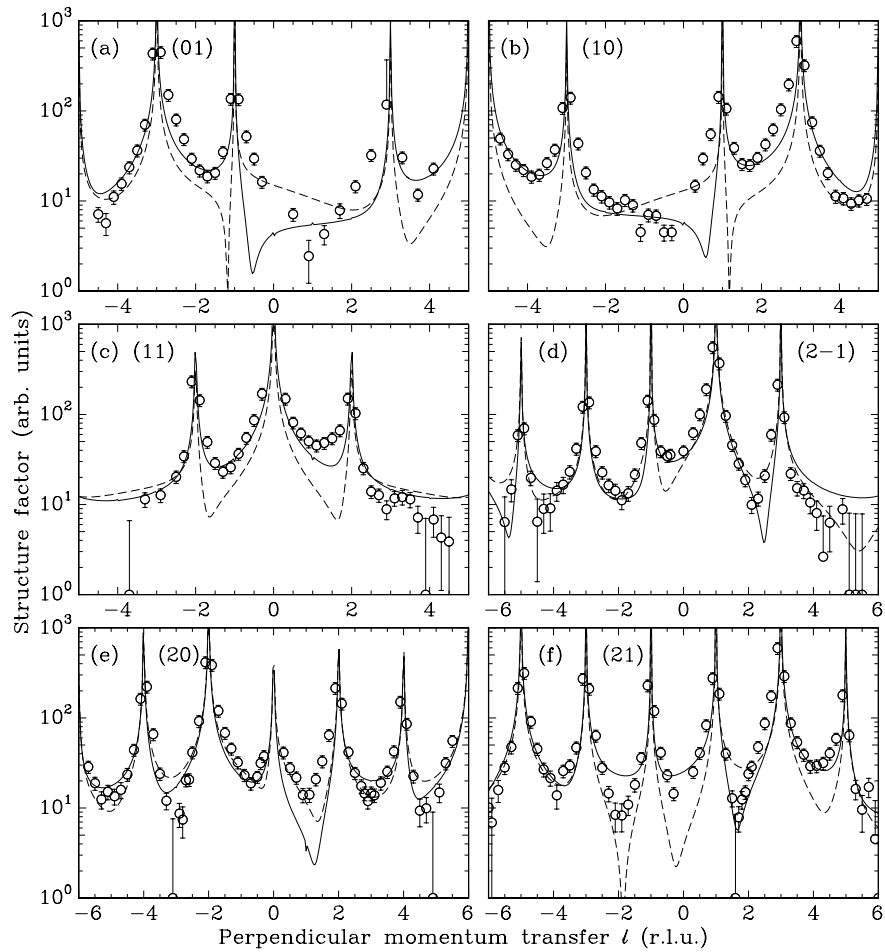


**Figure 6.5:** Structure factor amplitudes along 6 different crystal truncation rods ( $hk$ ) for KDP(101) in vacuum as a function of the diffraction index  $l$  which is expressed in reciprocal lattice units. The solid curves represent calculations for a bulk  $K^+$ -terminated surface, the dashed curves for a  $H_2PO_4^-$ -terminated one.

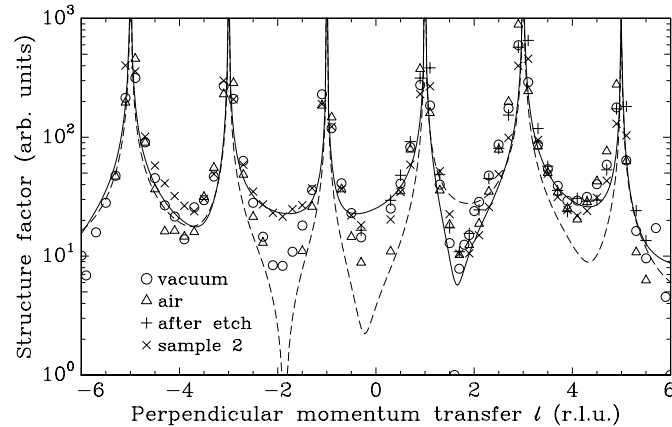


**Figure 6.6:** Structure factor amplitudes along the  $(2\ 1)$  crystal truncation rod for KDP(101).

(2 1 0.3) and (2 1 0.7) showed a decrease in structure factor amplitude of  $\sim 10\%$  during the 4.5 hour measurement of the  $(2\ 1)$  CTR.

We also measured some CTRs on KDP(100) in vacuum. This was done on a sawn crystal which was etched afterwards in pure water. Structure factor amplitudes for the  $(2\ 1)$  and  $(3\ 0)$  CTRs are shown in Fig. 6.7 together with a calculation of the bulk terminated KDP(100) surface. Contrary to the case of KDP(101), during these measurements we did not find any systematic changes in the intensity of reflections over a period of 19 hours.

In general we may conclude that the *ex situ* surface quality depends both on time and on the preparation conditions. For this reason *in situ* measurements are to be preferred.

## 6.5 In situ results

### 6.5.1 Atomic structure in equilibrium

In Daresbury we took a full data set using the crystal chamber as described in section 6.3. We used a Mylar foil with a thickness of  $3.8\ \mu\text{m}$ . The liquid layer on top of the surface was about  $\sim 10\ \mu\text{m}$  thick. The CTR results are shown in Fig. 6.8. The solid and dashed curves again give the expected structure factor distribution for a bulk  $\text{K}^+$ -terminated and  $\text{H}_2\text{PO}_4^-$ -terminated surface. The KDP crystals are sufficiently flat to measure the CTR intensity far from the Bragg peaks, where the surface sensitivity is highest, but in solution these parts are problematic due to the

X-RAY DIFFRACTION STUDIES OF KDP CRYSTAL SURFACES

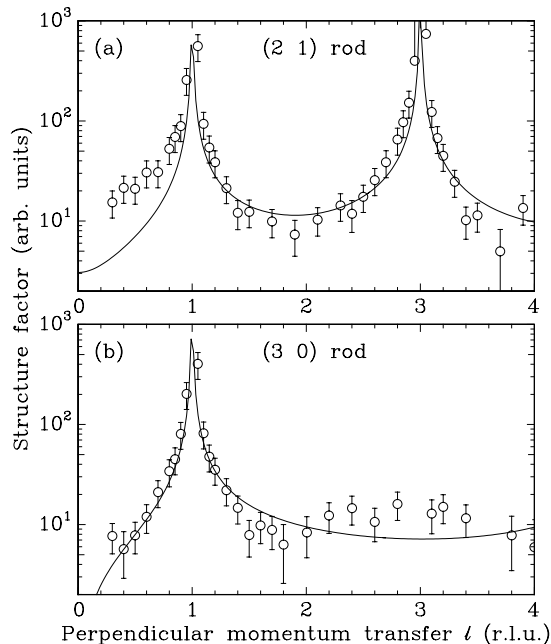


**Figure 6.7:** Structure factor amplitudes along the (2 1) and (3 0) crystal truncation rods for KDP(100) measured in vacuum. The solid curves show a calculation for a simple bulk terminated (100) surface.

high background. From these CTRs we can already conclude that the surface is K-terminated, but the measurements are not accurate enough to determine the precise structure. The possibility to do accurate measurements under these circumstances has enormously increased with the availability of high-intensity and high-energy X-ray beams from third-generation synchrotron radiation sources such as the ESRF.

At the TROIKA beamline at the ESRF the crystal growth chamber is mounted onto a horizontal diffractometer (i.e., the scattering plane is horizontal). Here a Mylar foil of 10  $\mu\text{m}$  was used. The beryllium monochromator was set to select a wavelength of 0.73  $\text{\AA}$  (17.0 keV) using the (002) reflection, leading to approximately  $10^{12}$  photons/sec in a  $2 \times 1 \text{ mm}^2$  spot. Unfortunately, the wavelength cannot be as easily changed as at beamline 9.4 in Daresbury, because at TROIKA the incoming beam optics has to be realigned for different wavelengths. Therefore, we could not do any optimization in this respect. We chose the wavelength of 0.73  $\text{\AA}$  to be sure we have little attenuation of X-rays in the liquid and at the same time have a high flux. For higher energies the diffuse background scattering from the bulk crystal

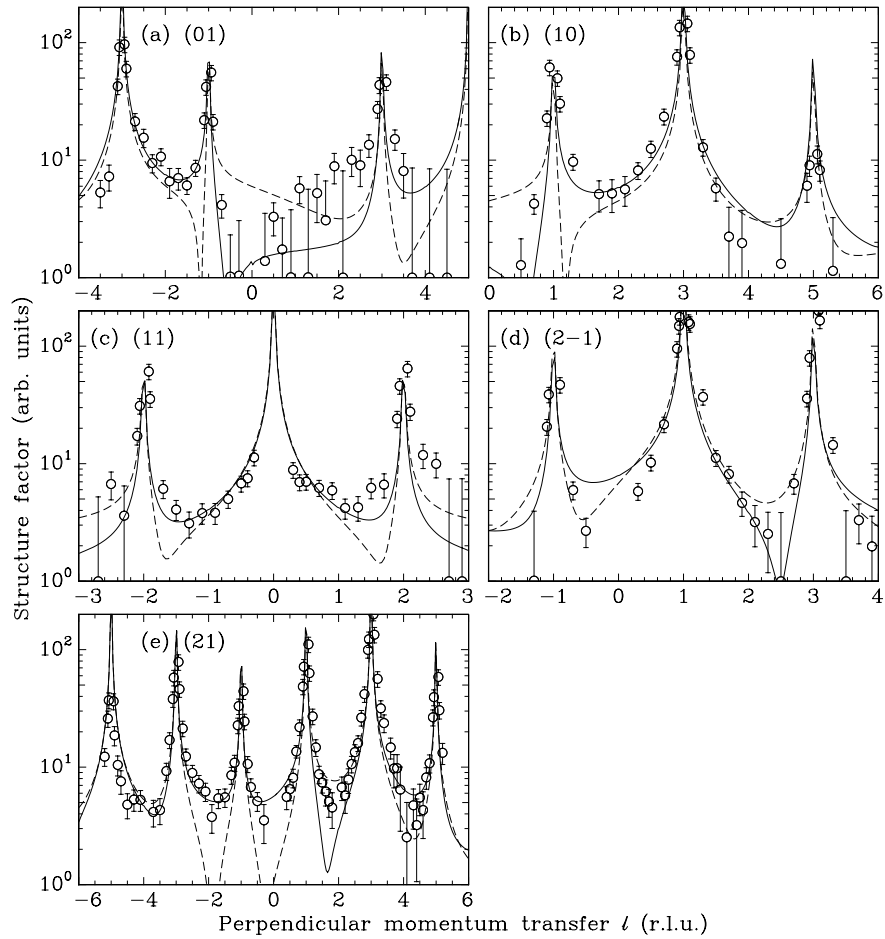


**Figure 6.8:** Structure factor amplitudes along 5 different crystal truncation rods ( $hk$ ) for KDP(101) in solution as a function of the diffraction index  $l$  measured on station 9.4 at Daresbury. The solid curve represents a calculation for a bulk  $K^+$ -terminated surface, the dashed curve for a  $H_2PO_4^-$ -terminated one.

## X-RAY DIFFRACTION STUDIES OF KDP CRYSTAL SURFACES

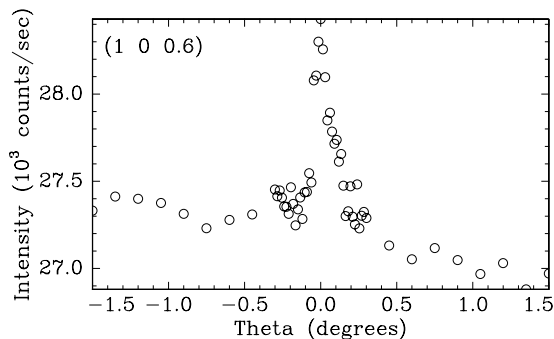


**Figure 6.9:** The (1 0 0.6) reflection measured in solution on KDP(101) at the TROIKA beamline at the ESRF.

rapidly goes up, as we learned from Fig. 6.3.

It is still very difficult to do accurate measurements on this system. For a typical surface reflection the signal-to-background ratio is about 10%, but for weak reflections this can be as small as 2%. As an example the (1 0 0.6) reflection is shown in Fig. 6.9. This is still far from the lowest part of the CTR (see Fig. 6.8(b) or Fig. 6.10(a)), but the signal to background ratio is only about 3%. The diffuse background intensity of 27000 counts per second is huge. Only the high flux at the ESRF allows us to measure such weak reflections in a reasonable time.

In Fig. 6.10 three CTRs measured *in situ* on KDP(101) are shown (open circles), together with the calculations for a bulk  $K^+$ -terminated surface (dotted curve), and a  $H_2PO_4^-$ -terminated surface (dashed curve). Our best-fit model, which was described in detail in chapter 5, is given by the solid curve (see for schematic of this model Fig. 5.1(b)).

The data measured on KDP(100) are presented in Fig. 5.3 of chapter 5. There we found that the surface is simply bulk terminated.

### 6.5.2 Specular reflectivity

We measured the specular reflectivity on the KDP(101) surface under three different circumstances. In Daresbury we measured this in ultra-high vacuum (circles in Fig. 6.11). At ID32 we measured the specular reflectivity both in air (triangles) and with solution (crosses). While for the CTRs discussed above there was little difference between air, vacuum or solution, here the vacuum data is very different and follows more closely the calculation for a  $H_2PO_4^-$ -terminated surface (dashed curve) than the one for a  $K^+$ -termination (solid curve). This could be real, but



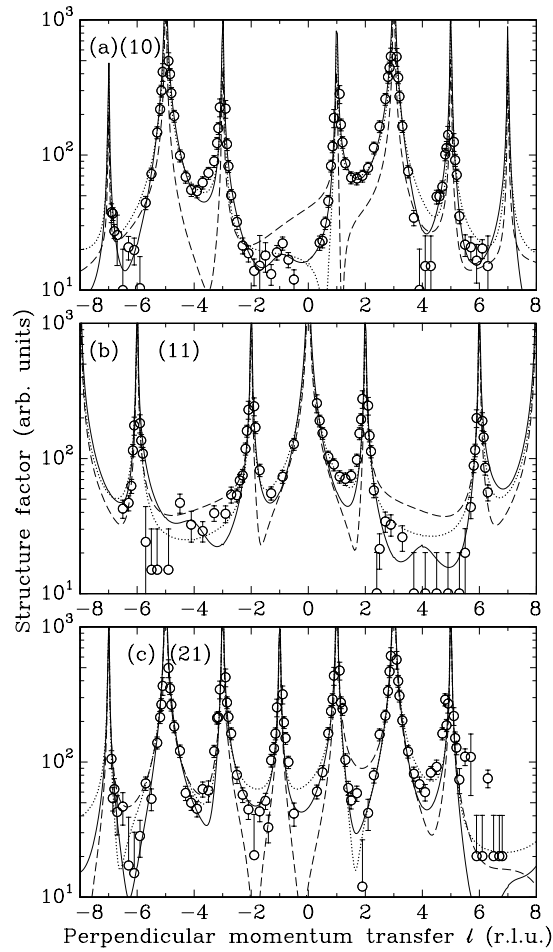


**Figure 6.10:** Structure factor amplitudes along the  $(10)$ ,  $(11)$ , and  $(21)$  crystal truncation rods for  $KDP(101)$  in solution as measured at TROIKA. The dotted line is a calculation for a bulk  $K^+$ -terminated surface, the dashed curve for a  $H_2PO_4^-$ -terminated one. The solid line is the best fit starting from a  $K^+$ -terminated surface and allowing the  $K^+$  ions and the  $H_2PO_4^-$  groups in the top layer to relax, as was described in chapter 5.

## X-RAY DIFFRACTION STUDIES OF KDP CRYSTAL SURFACES

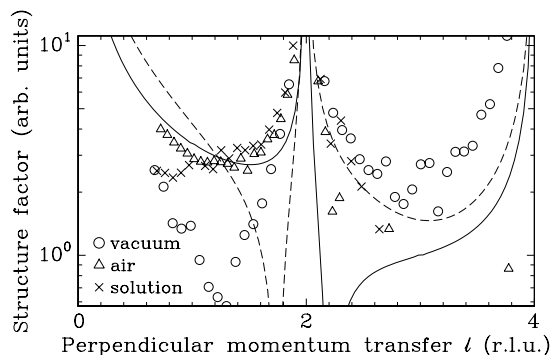


**Figure 6.11:** Structure factor amplitudes along the specular crystal truncation rod for KDP(101). The vacuum measurements were taken in Daresbury (circles) and the measurement in air (triangles) and in solution at ID32 at the ESRF using the transmission geometry (crosses). The solid curve represents a calculation for a bulk  $K^+$ -terminated surface, the dashed curve for a  $H_2PO_4^-$ -terminated one.

may also be caused by surface damage or by alignment problems. The other data follow the calculation for a  $K^+$ -termination more closely.

We used “ridge” scans to measure the specular reflectivity, in which the incident and exit angles are symmetrically incremented. The background intensity is measured by a similar scan giving one of the two beam angles an offset. This procedure may not be accurate enough because the background intensity is huge, in particular for large  $l$ -values. Another point of concern is the footprint of the incoming beam on the sample. If this footprint is smaller than the sample itself, this changes along the rod. To do these measurements accurately, transverse scans are necessary, while the alignment of surface and beamslits must be done very precisely. In principle the specular rod is more sensitive to the structure of the liquid side of the interface than the other CTRs, but the present data is not accurate enough to draw any conclusions about this. All we can say is that the specular data confirm the results from the other CTRs.

### 6.5.3 Impurities and growth

After establishing that the surface of KDP(101) is  $K^+$ -terminated we monitored some reflections during growth in order to determine the development of the surface roughness. The crystals grow when lowering the temperature of the system, which leads to supersaturation in the KDP solution. Heating leads analogously to dissolution of the crystal. By accurately controlling the temperature, the crystal

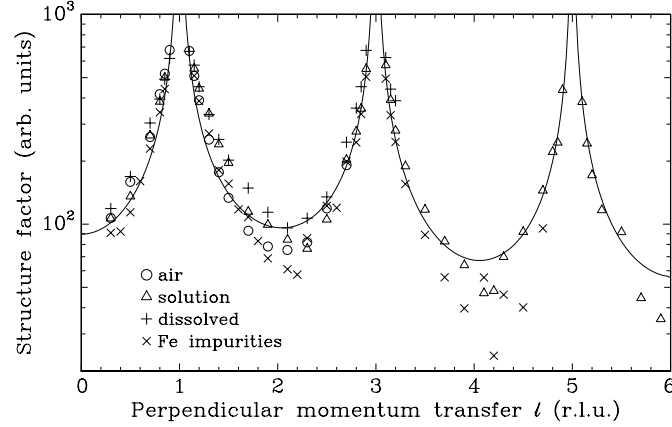


**Figure 6.12:** Structure factor amplitudes along the (1 2) crystal truncation rod for KDP(100) as measured at TROIKA.

surface can thus be conditioned.

The supersaturation  $\sigma$  is defined as

$$\sigma = \frac{c - c_{\text{eq}}(T)}{c_{\text{eq}}(T)}, \quad (6.2)$$

with  $c$  the actual concentration (kg solute/kg solvent), and  $c_{\text{eq}}(T)$  the saturation concentration. The saturation concentration curve follows from the solubility data [123]

$$c_{\text{eq}} = 0.1423 + 0.001463 \cdot T + 0.000031506 \cdot T^2, \quad (6.3)$$

with  $T$  in  $^{\circ}\text{C}$ .

After equilibrating the crystal at  $22^{\circ}\text{C}$ , we lowered the temperature to  $21^{\circ}\text{C}$ . This corresponds to a supersaturation  $\sigma$  of 2%. While changing the temperature we constantly measured the (2 1 0.7), (2 1 1.2), and (2 1 2.1) reflections. These measurements indicate that when we lower the temperature all reflections become sharper and the peak intensity higher. But also the structure factor amplitude increased. When heating up again to the original temperature the widths, peak intensity and integrated intensity decreased again. These measurements were done using the crystal chamber shown in Fig. 6.2(a).

The results for KDP(100) are shown in Fig. 6.12. The open circles give the measured structure factor amplitudes in air before the Mylar foil was mounted and the solution was put in. The open triangles show the same measurements as were

shown in Fig. 5.3 in solution. The solid curve is a calculation for an ideal flat bulk terminated crystal scaled to this data. There is not much difference between the in air data and the data taken in solution. However, we have measured the (1 2 0.7) reflection several times, and after filling the chamber with saturated solution the peaks definitely become sharper. We lowered the temperature to see whether we would see any effect on the surface quality, but we did not find significant changes. After this we increased the temperature to 23° and measured the (1 2) CTR again (+ signs). It appears that we have no real structural changes, but, since the structure factor amplitudes in between the Bragg peaks are sensitive to the roughness of the surface, we can conclude that after dissolution we seem to have the smoothest surface.

In chapter 5 we argued that from the atomic structure of both crystal faces, we can understand why metal impurities like Fe<sup>3+</sup> and Cr<sup>3+</sup> block the growth of the prismatic faces, but hardly affect the growth of the pyramidal faces. To find more evidence for this proposal, we added to our saturated KDP-solution a bit of FeCl to see whether the impurities affect the crystal surface. After dissolution the temperature was set back to its original value of 22° C. FeCl was added to the solution and after equilibrating this for some time, the (1 2) CTR was measured as depicted by the crosses in Fig. 6.12. The surface has roughened as seen from the decrease in intensity in between the Bragg peaks. The overall shape of the CTR is unchanged, so no ordered layer of Fe is formed on the surface.

As was discussed in section 6.3, for these experiments it is better to use a transmission geometry with more saturated solution on top of the surface. This was done with the top plate as depicted in Fig. 6.2(b) at ID32 at the ESRF. In Fig. 6.13 the (1 2) CTR on KDP(100) in solution is shown (circles). The solid curve again gives the expected structure factor distribution for a bulk terminated surface. First we want to determine what happens when we start the growth. Because of the “dead zone” on this surface, we need higher supersaturations than for KDP(101). We increased the supersaturation gradually to ~5% while monitoring different reflections along the rod. No significant changes were found. The total CTR was measured and the results are given by the triangles. The quality of the data is insufficient to say anything about differences in the structure factor amplitude intensities. Also in this chamber we tried to find evidence for an ordered layer of impurities on KDP(100). We doped the saturated KDP solution with 3 ppm Fe. Solutions containing iron impurities were made by using 10000 ppm iron in 2-5% nitric acid [124]. The results for the (1 2) CTR are depicted by the crosses. It seems that the surface has become rougher, but no structural changes are found.

On KDP(101) we also tried to look at *in situ* growth by measuring surface sensitive reflections while changing the temperature of the growth cell. Starting

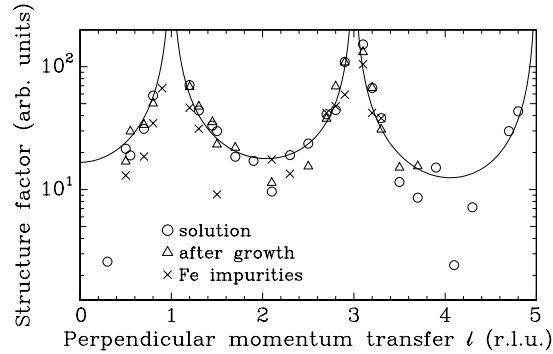


**Figure 6.13:** Structure factor amplitudes along the  $(1\ 2)$  crystal truncation rod for  $KDP(100)$  as measured with the transmission chamber at ID32 at the ESRF.

with the crystal in air, we observed an increase in width and decrease in height of the  $(2\ 1\ 0.55)$  reflection after adding a saturated solution. Since the integrated intensity stayed approximately constant, the crystallographic structure remains the same while the roughness is increasing.

Next we measured different surface sensitive reflections for different supersaturations to see what the effect of growth is on the surface quality and structure. The only significant and reproducible effect we have found is that upon dissolution of the crystal, the surface gets very smooth because the surface peaks get very sharp and the peak height goes up dramatically.

Unfortunately, during the time of these measurements there were problems with the synchrotron, which resulted in frequent beam losses. This was especially problematic because the monochromator needs time to stabilize after the beam is injected again. Because of these problems it was hard to determine which of the changes in our signal are due to this or due to real differences of our surface structure. These experiments need more stable conditions to extract reliable data.

## 6.6 Conclusions

We have used the technique of surface X-ray diffraction to study the structure of KDP crystal surfaces in air, vacuum and solution. All data show that the pyramidal  $\{101\}$  faces are terminated with K atoms rather than with  $H_2PO_4$  groups. From our measurements we cannot find clear differences between the surface structure in air, vacuum or in solution. In Fig. 6.14 the  $(1\ 0)$  rod measurements are compared. The data taken at the SRS and in HASYLAB are normalized on the  $(1\ 0\ 1.9)$  reflection of the TROIKA data. The vacuum data is consistent with the *in situ* data taken at

## X-RAY DIFFRACTION STUDIES OF KDP CRYSTAL SURFACES

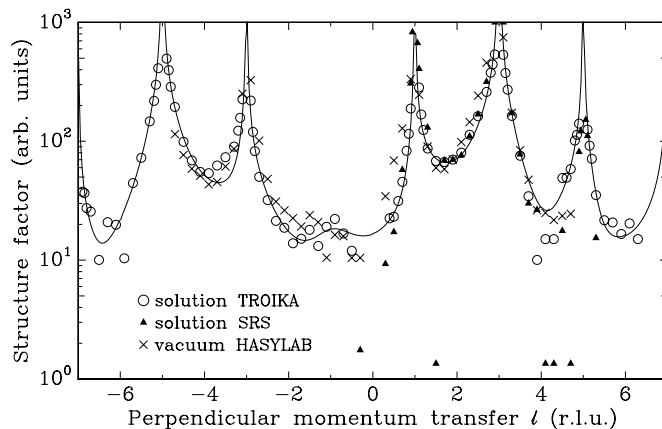


**Figure 6.14:** Comparison of the structure factor amplitudes along the  $(10)$  crystal truncation rod for  $KDP(101)$  measured in solution and in vacuum. The solid curve is our best-fit model calculation as described in chapter 5.

TROIKA. However, we have shown that when the surface is kept in vacuum the quality of the surface changes. Therefore, the *ex situ* data is not reliable enough to do an accurate structure determination. The quality of the surface, also as a function of time, is better controlled *in situ*.

Since the surface seems to recover in air, and certainly after a dip in pure water, it appears that in air the surface is covered by a thin layer of liquid. Recent ellipsometry measurements also point in this direction [125]. If this is the case, this liquid layer would gradually evaporate in vacuum and this may change the interface structure. This would also mean that the measurements done *in situ* should not be different from the ones done in air, because in both cases there would be a solid-liquid interface. Further experiments are necessary to clarify this.

We have found no evidence for an ordered Fe layer on the surface of  $KDP(100)$ . When we add Fe impurities to our saturated KDP solution, we observed the surface to become rougher. Apparently, the amounts of adsorbed Fe are very small. These impurities locally pin the moving steps, which causes an increased meandering of the steps and thus leads to a rougher surface.

In addition to stable X-ray beam conditions, the experiments can be improved along two lines. First of all it would help to observe whether growth or dissolution occurs by adding an optical microscope to the set-up. Secondly, the quality of the solution and the level of supersaturation could be controlled more accurately by flowing the solution over the surface, as is done in *in situ* AFM experiments [111].



## References

- [1] X.Y. LIU, E.S. BOEK, W.J. BRIELS, and P. BENNEMA, *Prediction of crystal growth morphology based on structural analysis of the solid-fluid interface*, Nature **374**, 342–345 (1995).
- [2] J.W.M. FRENKEN and J.F. VAN DER VEEN, *Observation of surface melting*, Phys. Rev. Lett. **54**, 134–137 (1985).
- [3] J.F. VAN DER VEEN, B. PLUIS, and A.W. DENIER VAN DER GON, *Surface melting*, in R. VANSELOW and R.F. HOWE, editors, *Chemistry and physics of solid surfaces VII*, volume 10 of *Springer series in surface sciences*, pp. 455–490, Berlin, 1988, Springer-Verlag.
- [4] D.W. OXTOBY, *New perspectives on freezing and melting*, Nature **347**, 725–730 (1990).
- [5] W.J. HUISMAN, J.F. PETERS, M.J. ZWANENBURG, S.A. DE VRIES, T.E. DERRY, D.L. ABERNATHY, and J.F. VAN DER VEEN, *Layering of a liquid metal in contact with a hard wall*, Nature **390**, 379–381 (1997).
- [6] W.J. HUISMAN, *Ordering phenomena at free and liquid covered diamond surfaces*, Ph.D. thesis, University of Amsterdam, 1997.
- [7] H.E. BUCKLEY, *Crystal growth*, John Wiley & Sons, New York, 1951.
- [8] J.B. ROMÉ DE LISLE, *Cristallographie*, volume 1, 2nd edition, 1783.
- [9] W.F. EGELHOFF and D.A. STEIGERWALD, *The role of adsorbed gases in metal on metal epitaxy*, J. Vac. Sci. Technol. A **7**, 2167–2173 (1989).
- [10] N. CABRERA and D.A. VERMILYEA, *The growth of crystals from solution*, in R.H. DOREMUS, B.W. ROBERTS, and D. TURNBULL, editors, *Growth and perfection of crystals*, pp. 393–410, New York, 1958, John Wiley & Sons.
- [11] J.J. DE MIGUEL, *Epitaxial growth and the role of surfactants*, Surf. Rev. Lett. **4**, 353–359 (1997).



## REFERENCES

- [12] H.A. VAN DER VEGT, H.M. VAN PINXTEREN, M. LOHMEIER, E. VLIEG, and J.M.C. THORNTON, *Surfactant-induced layer-by-layer growth of Ag on Ag(111)*, Phys. Rev. Lett. **68**, 3335–3338 (1992).
- [13] D.J. EAGLESHAM, F.C. UNTERWALD, and D.C. JACOBSEN, *Growth morphology and the equilibrium shape: the role of “surfactants” in Ge/Si island formation*, Phys. Rev. Lett. **70**, 966–969 (1993).
- [14] M.B. SMALL, E.A. GIESS, and R. GHEZ, *Liquid phase epitaxy*, in D.T.J. HURLE, editor, *Handbook of crystal growth*, volume 3a, pp. 223–253, Amsterdam, 1994, Elsevier Science Publishers.
- [15] E. BAUSER, P.O. HANSSON, M. ALBRECHT, H.P. STRUNK, and A. GUSTAFSSON, *Liquid phase epitaxy of SiGe structures*, Solid State Phenomena **32-33**, 385–396 (1993).
- [16] E. VLIEG, A.W. DENIER VAN DER GON, J.F. VAN DER VEEN, J.E. MACDONALD, and C. NORRIS, *Surface X-ray scattering during crystal growth: Ge on Ge(111)*, Phys. Rev. Lett. **61**, 2241–2244 (1988).
- [17] R. FEIDENHANS’L, *Surface structure determination by X-ray diffraction*, Surf. Sci. Rep. **10**, 105–188 (1989).
- [18] I.K. ROBINSON, *Surface crystallography*, in G. BROWN and D.E. MONCTON, editors, *Handbook on synchrotron radiation*, volume 3, pp. 221–266, Amsterdam, 1991, Elsevier Science Publishers.
- [19] I.K. ROBINSON and D.J. TWEET, *Surface X-ray diffraction*, Rep. Prog. Phys. **55**, 599–651 (1992).
- [20] E. VLIEG and I.K. ROBINSON, *Two-dimensional crystallography*, in P. COPPENS, editor, *Synchrotron radiation crystallography*, pp. 255–299, London, 1992, Academic Press.
- [21] S.R. ANDREWS and R.A. COWLEY, *Scattering of X-rays from crystal surfaces*, J. Phys. C **18**, 6427–6439 (1985).
- [22] I.K. ROBINSON, *Crystal truncation rods and surface roughness*, Phys. Rev. B **33**, 3830–3836 (1986).
- [23] W.F. EGELHOFF and I. JACOB, *Reflection High-Energy Electron Diffraction (RHEED) oscillations at 77 K*, Phys. Rev. Lett. **62**, 921–924 (1989).

## REFERENCES

- [24] R. KUNKEL, B. POELSEMA, L.K. VERHEIJ, and G. COMSA, *Reentrant layer-by-layer growth during molecular-beam epitaxy of metal-on-metal substrates*, Phys. Rev. Lett. **65**, 733–736 (1990).
- [25] E. BAUER and H. POPPA, *Recent advances in epitaxy*, Thin Solid Films **12**, 167–185 (1972).
- [26] H.L. GAIGHER, N.G. VAN DER BERG, and J.B. MALHERBE, *Effect of residual gas pressure on the epitaxial growth of vacuum-deposited chromium on Cu{111} substrates*, Thin Solid Films **137**, 337–349 (1986).
- [27] B. POELSEMA, R. KUNKEL, N. NAGEL, A.F. BECKER, G. ROSENFELD, L.K. VERHEIJ, and G. COMSA, *New phenomena in homoepitaxial growth of metals*, Appl. Phys. A **53**, 369–376 (1991).
- [28] S. ESCH, M. HOHAGE, TH. MICHELY, and G. COMSA, *Origin of oxygen induced layer-by-layer growth in homoepitaxy on Pt(111)*, Phys. Rev. Lett. **72**, 518–521 (1994).
- [29] H.A. VAN DER VEGT, W.J. HUISMAN, P.B. HOWES, and E. Vlieg, *The effect of Sb on the nucleation and growth of Ag on Ag(100)*, Surf. Sci. **330**, 101–112 (1995).
- [30] H.A. VAN DER VEGT, J. ALVAREZ, X. TORRELLES, S. FERRER, and E. Vlieg, *Indium-induced layer-by-layer growth and suppression of twin formation in the homoepitaxial growth of Cu(111)*, Phys. Rev. B **52**, 17443–17448 (1995).
- [31] S.A. DE VRIES, W.J. HUISMAN, P. GOEDTKINDT, M.J. ZWANENBURG, S.L. BENNETT, and E. Vlieg, *Floating stacking fault during homoepitaxial growth of Ag(111)*, Phys. Rev. Lett. **81**, 381–384 (1998); chapter 3 in this thesis.
- [32] J.A. MEYER, H.A. VAN DER VEGT, J. VRIJMOETH, E. Vlieg, and R.J. BEHM, *Reversible place-exchange during film growth: a mechanism for surfactant transport*, Surf. Sci. **355**, L375–L380 (1996).
- [33] J. VRIJMOETH, H.A. VAN DER VEGT, J.A. MEYER, E. Vlieg, and R.J. BEHM, *Surfactant-induced layer-by-layer growth of Ag on Ag(111): origins and side effects*, Phys. Rev. Lett. **72**, 3843–3846 (1994).
- [34] H.A. VAN DER VEGT, J. VRIJMOETH, R.J. BEHM, and E. Vlieg, *Sb enhanced nucleation in the homoepitaxial growth of Ag(111)*, Phys. Rev. B **57**, 4127–4131 (1998).

## REFERENCES

- [35] S. OPPO, V. FIORENTINI, and M. SCHEFFLER, *Theory of adsorption and surfactant effect of Sb on Ag(111)*, Phys. Rev. Lett. **71**, 2437–2440 (1993).
- [36] T.C.Q. NOAKES, D.A. HUTT, and C.F. MCCONVILLE, *Adsorption of Sb on Ag(111) studied using LEED, AES and XPS*, Surf. Sci. **307-309**, 101–106 (1994).
- [37] T.C.Q. NOAKES, D.A. HUTT, C.F. MCCONVILLE, and D.P. WOODRUFF, *Structural investigation of ordered Sb adsorption phases on Ag(111) using coaxial impact collision ion scattering spectroscopy*, Surf. Sci. **372**, 117–131 (1997).
- [38] H. CRUGUEL, B. LÉPINE, S. ABABOU, F. SOLAL, and G. JÉZÉQUEL, *Photoelectron diffraction evidence for a surface substitutional site of Sb in the Sb-induced smooth growth of Ag on Ag(111)*, Phys. Rev. B **55**, R16061–R16064 (1997).
- [39] H. GIORDANO, O. ALEM, and B. AUFRAY, *Kinetics of surface segregation in Cu(Sb) alloys: determination of the diffusion coefficients*, Scr. Metall. **28**, 257–262 (1993).
- [40] H. GIORDANO and B. AUFRAY, *On a kinetic approach to the study of superficial equilibrium segregation in the Sb-Cu(111) system*, Surf. Sci. **307-309**, 816–820 (1994).
- [41] P. MA and A.J. SLAVIN, *Adsorption of antimony on Au(111) at room temperature*, J. Vac. Sci. Technol. A **11**, 2003–2007 (1993).
- [42] C. NORRIS, M.S. FINNEY, G.F. CLARK, G. BAKER, P.R. MOORE, and R. VAN SILFHOUT, *Design and performance of a focused beam line for surface X-ray diffraction*, Rev. Sci. Instrum. **63**, 1083–1086 (1992).
- [43] E. VLIEG, A. VAN 'T ENT, A.P. DE JONGH, H. NEERINGS, and J.F. VAN DER VEEN, *An ultrahigh-vacuum chamber for surface X-ray diffraction combined with MBE*, Nucl. Instr. Meth. A **262**, 522 (1987).
- [44] M. LOHMEIER and E. VLIEG, *Angle calculations for a six-circle surface X-ray diffractometer*, J. Appl. Cryst. **26**, 706–716 (1993).
- [45] J.S.G. TAYLOR, C. NORRIS, E. VLIEG, M. LOHMEIER, and T.S. TURNER, *An out-of-plane detector for surface x-ray diffraction*, Rev. Sci. Instrum. **67**, 2658–2659 (1996).

## REFERENCES

- [46] E. VLIEG, *Integrated intensities using a six-circle surface X-ray diffractometer*, J. Appl. Cryst. **30**, 532–543 (1997).
- [47] C.H. MACGILLAVRY and G.D. RIECK, editors, *International tables for X-ray crystallography*, volume 3, Reidel, Dordrecht, 1983.
- [48] E. VLIEG, J.F. VAN DER VEEN, S.J. GURMAN, C. NORRIS, and J.E. MACDONALD, *X-ray diffraction from rough, relaxed and reconstructed surfaces*, Surf. Sci. **210**, 301–321 (1989).
- [49] R.J. BAXTER, *Exactly solved models in statistical mechanics*, Academic press, London, 1982.
- [50] F. COMIN, P.H. CITRIN, P. EISENBERGER, and J.E. ROWE, *Unusual chemisorption behavior of Te on Cu{111} versus Cu{100}*, Phys. Rev. B **26**, 7060–7062 (1982).
- [51] S.Å. LINDGREN, L. WALLDÉN, J. RUNDGREN, and P. WESTRIN, *Low-energy electron diffraction from Cu(111): subthreshold effect and energy-dependent inner potential; surface relaxation and metric distances between spectra*, Phys. Rev. B **29**, 576 (1984).
- [52] P. BAILEY, private communication.
- [53] A.W. DENIER VAN DER GON, R.M. TROMP, and M.C. REUTER, *Low energy electron microscopy studies of Ge and Ag growth on Si(111)*, Thin Solid Films **236**, 140–145 (1993).
- [54] K.-H. PARK, J.S. HA, S.-J. PARK, and E.-H. LEE, *Ag growth on Si(111) with an Sb surfactant investigated by scanning tunneling microscopy*, Surf. Sci. **380**, 258–263 (1997).
- [55] T. LEWOWSKI and P. WIECZOREK, *Effect of surfactant and substrate temperature on the growth of Ag films on a sapphire surface*, Surf. Rev. Lett. **4**, 219–222 (1997).
- [56] H.A. VAN DER VEGT, W.J. HUISMAN, P.B. HOWES, T.S. TURNER, and E. VLIEG, *Surfactants used in Ag(111) homoepitaxy: Sb, In, Pt and O<sub>2</sub>*, Surf. Sci. **365**, 205–211 (1996).
- [57] J. CAMARERO, L. SPENDELER, G. SCHMIDT, K. HEINZ, J.J. DE MIGUEL, and R. MIRANDA, *Surfactant-induced suppression of twin formation during growth of fcc Co/Cu superlattices on Cu(111)*, Phys. Rev. Lett. **73**, 2448–2451 (1994).

## REFERENCES

- [58] K. MEINEL, M. KLAUA, and H. BETHGE, *On twin and stacking fault formation during the epitaxial film growth of fcc materials on (111) substrates*, Phys. Stat. Sol. (a) **110**, 189–196 (1988).
- [59] CH. AMMER, T. SCHAEFER, CH. TEICHERT, K. MEINEL, and M. KLAUA, *The multilayer growth mode in the epitaxy of Ag on Ag(111) analysed by SPALEED*, Surf. Sci. **307-309**, 570–575 (1994).
- [60] E.Z. LUO, J. WOLLSCHLÄGER, F. WEGNER, and M. HENZLER, *SPA-LEED studies of growth of Ag on Ag(111) at low temperatures*, Appl. Phys. A **60**, 19–25 (1995).
- [61] C. RATSCH, A.P. SEITSONEN, and M. SCHEFFLER, *Strain dependence of surface diffusion: Ag on Ag(111) and Pt(111)*, Phys. Rev. B **55**, 6750–6753 (1997).
- [62] S.A. DE VRIES, W.J. HUISMAN, P. GOEDTKINDT, M.J. ZWANENBURG, S.L. BENNETT, I.K. ROBINSON, and E. VLIEG, *Surface atomic structure of the  $(\sqrt{3} \times \sqrt{3})R30^\circ$ -Sb reconstructions of Ag(111) and Cu(111)*, Surf. Sci. **414**, 159–169 (1998); chapter 2 in this thesis.
- [63] CH. RATH, J.E. PRIETO, S. MÜLLER, R. MIRANDA, and K. HEINZ, *hcp-to-fcc stacking switch in thin cobalt films induced by Cu capping*, Phys. Rev. B **55**, 10791–10799 (1997).
- [64] E. BAUSER, *Atomic mechanisms in semiconductor liquid phase epitaxy*, in D.T.J. HURLE, editor, *Handbook of crystal growth*, volume 3b, pp. 879–939, Amsterdam, 1994, Elsevier Science Publishers.
- [65] S.K. SINHA, editor, *Ordering in two dimensions*, Elsevier North Holland, New York, 1980.
- [66] J.W.M. FRENKEN and H.M. VAN PINXTEREN, *Surface melting: an experimental overview*, in D.A. KING and D.P. WOODRUFF, editors, *Phase transitions and adsorbate restructuring at metal surfaces*, volume 7 of *The chemical physics of solid surfaces*, pp. 259–290, Amsterdam, 1994, Elsevier.
- [67] P.H. FUOSS, L.J. NORTON, and S. BRENNAN, *X-ray scattering studies of the melting of lead surfaces*, Phys. Rev. Lett. **60**, 2046–2049 (1988).
- [68] H.M. VAN PINXTEREN, S. CHANDAVARKAR, W.J. HUISMAN, J.M. GAY, and E. VLIEG, *Thermal diffuse scattering from surface-melted Pb(110)*, Phys. Rev. B **51**, 14753–14755 (1995).

## REFERENCES

- [69] J.J. MÉTOIS and G. LE LAY, *Complementary data obtained on the metal-semiconductor interface by LEED, AES and SEM: Pb/Ge(111)*, Surf. Sci. **133**, 422–442 (1983).
- [70] T. ICHIKAWA, *Formation of two-dimensional solid and liquid Pb on Ge(111) surfaces*, Solid State Commun. **46**, 827–831 (1983).
- [71] T. ICHIKAWA, *On the structure of monolayer liquid Pb on Ge(111) surfaces*, Solid State Commun. **49**, 59–64 (1984).
- [72] R. FEIDENHANS'L, J.S. PEDERSEN, M. NIELSEN, F. GREY, and R.L. JOHNSON, *Ge(111) $\sqrt{3} \times \sqrt{3}$ -Pb: the atomic geometry*, Surf. Sci. **178**, 927–933 (1986).
- [73] B.P. TONNER, H. LI, M.J. ROBRECHT, Y.C. CHOU, M. ONELLION, and J.L. ERSKINE, *Temperature dependence of photoelectron scattering from a monolayer*, Phys. Rev. B **34**, 4386–4389 (1986).
- [74] J.S. PEDERSEN, R. FEIDENHANS'L, M. NIELSEN, K. KJÆR, F. GREY, and R.L. JOHNSON, *Adsorbate registry and subsurface relaxation of the  $\alpha$ -Ge(111) $\sqrt{3} \times \sqrt{3}$ -Sn/Pb reconstructions*, Surf. Sci. **189-190**, 1047–1054 (1987).
- [75] B.P. TONNER, H. LI, M.J. ROBRECHT, M. ONELLION, and J.L. ERSKINE, *Photoemission study of the valence band of Pb monolayers on Ge(111)*, Phys. Rev. B **36**, 989–997 (1987).
- [76] F. GREY, *The phases of Pb/Ge(111): a surface X-ray diffraction study*, Ph.D. thesis, Copenhagen University, 1988 (unpublished).
- [77] B.N. DEV, F. GREY, R.L. JOHNSON, and G. MATERLIK, *High-temperature X-ray standing-wave study: application to melting of monolayers of Pb on Ge(111) surfaces*, Europhys. Lett. **6**, 311–316 (1988).
- [78] H. LI and B.P. TONNER, *A LEED study of the structure of epitaxial Pb/Ge(111) monolayers and ultra-thin films*, Surf. Sci. **193**, 10–32 (1988).
- [79] H. HUANG, C.M. WEI, H. LI, B.P. TONNER, and S.Y. TONG, *Quantitative structural determination of metallic film growth on a semiconductor crystal: ( $\sqrt{3} \times \sqrt{3}$ )R30°  $\rightarrow$  (1 $\times$ 1) Pb on Ge(111)*, Phys. Rev. Lett. **62**, 559–562 (1989).
- [80] F. GREY, R. FEIDENHANS'L, J. SKOV PEDERSEN, M. NIELSEN, and R.L. JOHNSON, *Pb/Ge(111) 1 $\times$ 1: An anisotropic two-dimensional liquid*, Phys. Rev. B **41**, 9519–9522 (1990).

## REFERENCES

- [81] M. ABRAHAM and G. LE LAY, *Spectroellipsometric study of the growth and phase transitions of a two-dimensional metal: Pb on Ge(111)*, Thin Solid Films **233**, 264–267 (1993).
- [82] F. ANCILOTTO, A. SELONI, and R. CAR,  *$\beta$  phase of Pb on Ge(111): the competing roles of electronic bonding and thermal fluctuations*, Phys. Rev. Lett. **71**, 3685–3688 (1993).
- [83] L. SEEHOFER, G. FALKENBERG, and R.L. JOHNSON, *STM study of the structure and phases of Pb on Ge(111)*, Surf. Sci. **290**, 15–25 (1993).
- [84] I.-S. HWANG and J.A. GOLOVCHENKO, *Tunneling microscope observation of a structural surface phase transition: structure, fluctuations, and local effects*, Phys. Rev. Lett. **71**, 255–258 (1993).
- [85] I.-S. HWANG and J.A. GOLOVCHENKO, *Phase transition of monolayer Pb/Ge(111):  $\beta$ - $(\sqrt{3} \times \sqrt{3})R30^\circ \leftrightarrow 1 \times 1$  at  $\sim 180^\circ\text{C}$* , Phys. Rev. B **50**, 18535–18542 (1994).
- [86] F. ANCILOTTO, A. SELONI, and R. CAR, *Low- and high-temperature phases of a Pb monolayer on Ge(111) from ab initio molecular dynamics*, Phys. Rev. B **50**, 15158–15165 (1994).
- [87] L. SEEHOFER, D. DABOUL, G. FALKENBERG, and R.L. JOHNSON, *STM study of the incommensurate structures of Pb on Ge(111) and Si(111) surfaces*, Surf. Sci. **307-309**, 698–703 (1994).
- [88] L. SEEHOFER, D. DABOUL, G. FALKENBERG, and R.L. JOHNSON, *Reconstructions formed by Pb on Ge(111) surfaces reexamined by STM*, Surf. Sci. **314**, L879–L883 (1994).
- [89] G.E. FRANKLIN, M.J. BEDZYK, J.C. WOICIK, CHIEN LIU, J.R. PATEL, and J.A. GOLOVCHENKO, *Order-to-disorder phase-transition study of Pb on Ge(111)*, Phys. Rev. B **51**, 2440–2445 (1995).
- [90] J.M. CARPINELLI, H.H. WEITERING, E.W. PLUMMER, and R. STUMPF, *Direct observation of a surface charge density wave*, Nature **381**, 398–400 (1996).
- [91] J. AVILA, A. MASCARAQUE, E.G. MICHEL, and M.C. ASENSIO, *Phase transition of submonolayer Pb/Ge(111):  $\alpha$ - $(\sqrt{3} \times \sqrt{3})R30^\circ \leftrightarrow 3 \times 3$  at  $\sim 250\text{ K}$* , Appl. Surf. Sci. **123/124**, 626–630 (1998).

## REFERENCES

- [92] K. WÜRDE, P. KRÜGER, A. MAZUR, and J. POLLMANN, *First-principles investigations of the atomic and electronic structure of Pb, Sn and Ge adsorbed on the Ge(111)-( $\sqrt{3} \times \sqrt{3}$ ) surface*, Surf. Rev. Lett. **5**, 105–110 (1998).
- [93] E. VLIEG, J.F. VAN DER VEEN, J.E. MACDONALD, and M. MILLER, *Angle calculations for a 5-circle diffractometer used for surface X-ray diffraction*, J. Appl. Cryst. **20**, 330 (1987).
- [94] R. FEIDENHANS'L, J.S. PEDERSEN, J. BOHR, and M. NIELSEN, *Surface structure and long-range order of the Ge(111)-c(2×8) reconstruction*, Phys. Rev. B **38**, 9715–9720 (1988).
- [95] R.G. VAN SILFHOUT, J.F. VAN DER VEEN, C. NORRIS, and J.E. MACDONALD, *Structure of the Ge(111)-c(2×8) surface as determined from scattered X-ray intensities along crystal truncation rods*, Faraday Discuss. Chem. Soc. **89**, 169–180 (1990).
- [96] B.W. BATTERMAN and D.R. CHIPMAN, *Vibrational amplitudes in germanium and silicon*, Phys. Rev. **127**, 690–693 (1962).
- [97] B.E. WARREN, *X-ray diffraction*, Addison-Wesley, Reading, MA, 1969.
- [98] B.N. DEV, *Comment on “Quantitative structural determination of metallic film growth on a semiconductor crystal: ( $\sqrt{3} \times \sqrt{3}$ )R30° → (1×1) Pb on Ge(111)”*, Phys. Rev. Lett. **64**, 1182–1183 (1990).
- [99] P. HARTMAN, *Structure and morphology*, in P. HARTMAN, editor, *Crystal growth: an introduction*, pp. 367–402, Amsterdam, 1973, North-Holland.
- [100] P. BENNEMA, *Growth and morphology of crystals: integration of theories of roughening and Hartman-Perdok theory*, in D.T.J. HURLE, editor, *Handbook of crystal growth*, volume 1a, pp. 477–581, Amsterdam, 1993, Elsevier Science Publishers.
- [101] B.R. MCCLAIN, D.D. LEE, B.L. CARVALHO, S.G.J. MOCHRIE, S.H. CHEN, and J.D. LITSTER, *X-ray reflectivity study of an oil-water interface in equilibrium with a middle-phase microemulsion*, Phys. Rev. Lett. **72**, 246–249 (1994).
- [102] B.M. OCKO, *Smectic-layer growth at solid interfaces*, Phys. Rev. Lett. **64**, 2160–2163 (1990).



## REFERENCES

- [103] B.M. OCKO, J. WANG, A. DAVENPORT, and H. ISAACS, *In situ X-ray reflectivity and diffraction studies of the Au(001) reconstruction in an electrochemical cell*, Phys. Rev. Lett. **65**, 1466–1469 (1990).
- [104] M.F. TONEY, J.N. HOWARD, J. RICHER, G.L. BORGES, J.G. GORDON, O.R. MELROY, D.G. WIESLER, D. YEE, and L.B. SORESENSEN, *Voltage-dependent ordering of water molecules at an electrode-electrolyte interface*, Nature **368**, 444–446 (1994).
- [105] R.P. CHIARELLO and N.C. STURCHIO, *The calcite ( $10\bar{1}4$ ) cleavage surface in water: early results of a crystal truncation rod study*, Geochim. Cosmochim. Acta **59**, 4557–4561 (1995).
- [106] D. GIDALEVITZ, R. FEIDENHANS’L, S. MATLIS, D.-M. SMILGIES, M.J. CHRISTENSEN, and L. LEISEROWITZ, *Monitoring in situ growth and dissolution of molecular crystals: towards determination of the growth units*, Angew. Chem. Int. Ed. Engl. **36**, 955–959 (1997).
- [107] L.N. RASHKOVICH, *KDP-family single crystals*, The Adam Hilger series on optics and optoelectronics, IOP Publishing Ltd, Bristol, 1991.
- [108] P. HARTMAN, *The morphology of zircon and potassium dihydrogen phosphate in relation to the crystal structure*, Acta Cryst. **9**, 721–727 (1956).
- [109] B. DAM, P. BENNEMA, and W.J.P. VAN ENCKEVORT, *The mechanism of tapering on KDP-type crystals*, J. Crystal Growth **74**, 118–128 (1986).
- [110] W.J.P. VAN ENCKEVORT, R. JANSSEN-VAN ROSMALEN, and W.H. VAN DER LINDEN, *Evidence for spiral growth on the pyramidal faces of KDP and ADP single crystals*, J. Crystal Growth **49**, 502–514 (1980).
- [111] J.J. DE YOREO, T.A. LAND, and B. DAIR, *Growth morphology of vicinal hillocks on the  $\{101\}$  face of  $KH_2PO_4$ : from step-flow to layer-by-layer growth*, Phys. Rev. Lett. **73**, 838–841 (1994).
- [112] R.J. NELMES, Z. TUN, and W.F. KUHS, *A compilation of accurate structural parameters for KDP and DKDP, and a users’ guide to their crystal structures*, Ferroelectrics **71**, 125–141 (1987).
- [113] G. GRÜBEL, J. ALS-NIELSEN, and A.K. FREUND, *The TROIKA beamline at ESRF*, J. de Physique IV **4**, C9–27–C9–34 (1994).

## REFERENCES

- [114] B. DAM and W.J.P. VAN ENCKEVORT, *In situ observation of surface phenomena on {100} and {101} potassium dihydrogen phosphate crystals*, *J. Crystal Growth* **69**, 306–311 (1984).
- [115] B. DAM, E. POLMAN, and W.J.P. VAN ENCKEVORT, *In situ observation of surface phenomena on {100} KDP related to growth kinetics and impurity action*, in S.J. JANČIĆ and E.J. DE JONG, editors, *Industrial crystallization 84*, p. 97, Amsterdam, 1984, Elsevier Science Publishers.
- [116] C. BELOUET, E. DUNIA, and J.F. PÉTROFF, *X-ray topographic study of defects in  $KH_2PO_4$  single crystals and their relation with impurity segregation*, *J. Crystal Growth* **23**, 243–252 (1974).
- [117] LU TAIJING, R.B. YALLEE, C.K. ONG, and I. SUNAGAWA, *Formation mechanism of tapering of crystals: a comparative study between potassium dihydrogen phosphate crystals and natural quartz crystals*, *J. Crystal Growth* **151**, 342–347 (1995).
- [118] J. PAQUETTE and R.J. REEDER, *Relationship between surface structure, growth mechanism, and trace element incorporation in calcite*, *Geochim. Cosmochim. Acta* **59**, 735–749 (1995).
- [119] A.A. CHERNOV, *Modern Crystallography III, Crystal Growth*, volume 36 of *Springer series in solid-state sciences*, Springer-Verlag, Berlin, 1984.
- [120] M.F. TONEY, J.G. GORDON, M.G. SAMANT, G.L. BORGES, O.R. MELROY, D. YEE, and L.B. SORENSEN, *Underpotentially deposited thallium on silver (111) by in situ surface x-ray scattering*, *Phys. Rev. B* **45**, 9362–9374 (1992).
- [121] S.A. DE VRIES, P. GOEDTKINDT, S.L. BENNETT, W.J. HUISMAN, M.J. ZWANENBURG, D.-M. SMILGIES, J.J. DE YOREO, W.J.P. VAN ENCKEVORT, P. BENNEMA, and E. Vlieg, *Surface atomic structure of KDP crystals in aqueous solution: an explanation of the growth shape*, *Phys. Rev. Lett.* **80**, 2229–2232 (1998); chapter 5 in this thesis.
- [122] W. DRUBE, H. SCHULTE-SCHREPPING, H.-G. SCHMIDT, R. TREUSCH, and G. MATERLIK, *Design and performance of the high-flux/high-brightness x-ray wiggler beamline BW2 at HASYLAB*, *Rev. Sci. Instrum.* **66**, 1668–1670 (1995).
- [123] J.W. MULLIN and A. AMATAVIVADHANA, *Growth kinetics of ammonium- and potassium-dihydrogen phosphate crystals*, *J. Appl. Chem.* **17**, 151–156 (1967).

## REFERENCES

- [124] Glen Spectra Reference Materials, Stanmore Middlesex, England.
- [125] M. REEDIJK, M. DEVILLERS, and E. VLIEG, unpublished.

## Summary

The quality of crystals is to a large extent determined by the surface structure and dynamics during growth. The growth of many crystals is strongly influenced by the presence of impurities, defects, surface reconstructions or adsorption layers. This thesis describes X-ray scattering experiments in which the structure of crystal interfaces is determined in order to get an atomic-scale understanding of the kinetic and thermodynamic processes involved in growth. The first part of this thesis is concerned with crystals and their growth in an ultra-high vacuum (UHV) environment, where the conditions of the surface can be controlled very well. In the last two chapters we describe experiments on a crystal in its growth solution.

In homoepitaxial growth of Ag(111) it is known that by adding a surfactant like Sb the growth mode can be changed from three dimensional (rough) to layer-by-layer (smooth). The equilibrium surface structure of an Sb-covered Ag(111) surface depends on the Sb coverage. For coverages below 1/3 monolayer, the Sb atoms substitute for Ag atoms at normal fcc positions in the top surface layer. There is no lateral ordering of the Sb atoms. At a coverage of 1/3 monolayer a  $(\sqrt{3}\times\sqrt{3})R30^\circ$  reconstruction is formed. We have determined the atomic structure of this reconstruction for the Ag(111)-Sb as well as for the similar Cu(111)-Sb surfaces (chapter 2). Contrary to previous reports we found that all top layer atoms reside at stacking fault positions. Each  $(\sqrt{3}\times\sqrt{3})R30^\circ$  surface unit cell contains one substitutional Sb atom. We determined the out-of-plane relaxations of the top layer atoms and the in-plane distortions in the second layer. When Ag is deposited on this surface at 100°C, the Sb segregates and the Ag atoms return to the correct fcc stacking, while the new Ag atoms in the top layer again have the hcp stacking. This thus effectively leads to a floating stacking fault. Because of kinetic limitations, the same effect occurs for Sb coverages below 1/3 monolayer. For growth above 100°C, all lower lying Ag layers return to the correct stacking, and no twin crystallites are formed.

In chapter 4 we study a model solid-liquid interface. We present a structural analysis of the  $\beta$ -Ge(111) $(\sqrt{3}\times\sqrt{3})R30^\circ$ -Pb  $\rightarrow$   $1\times 1$  phase transition at  $\sim 180^\circ\text{C}$  for a Pb coverage of 1.25 monolayer. Below the phase transition the  $\beta$  phase has a saturation coverage of 4/3 monolayer. Our atomic structure model for this phase, consisting of three Pb atoms on off-centered  $T_1$  sites and one on a  $H_3$

## SUMMARY

site in the unit cell, is consistent with other studies reported for this system. We find that above the phase transition the single layer of Pb gives rise to a ring of diffuse scattering indicative of a two-dimensional liquid. However, of all the Pb geometries considered, an ordered layer with large in-plane thermal vibration amplitude is found to provide the best agreement between calculated and measured structure factors. The Pb atoms appear to rapidly diffuse over the surface, but spend a significant fraction at the lattice sites that are occupied at the low temperature  $\beta$ -phase. The Pb layer has thus both liquid and solid properties.

Although most crystals are grown from the liquid phase, the atomic structure of the growing interface is hardly studied because of a lack of suitable techniques. Most surface science techniques need a UHV environment and cannot be applied to surfaces in a fluid. X-ray diffraction using the latest synchrotron radiation facilities make these studies feasible for the first time. We have studied the interface atomic structure of the inorganic crystal KDP. KDP crystals are grown from an aqueous solution. *Ex situ* measurements were performed in vacuum and in air. In order to be able to do *in situ* measurements, where the crystal is in contact with its growth solution, we have designed and built a crystal growth chamber which is compatible with X-ray diffraction experiments (chapter 6). The surface atomic structure has been determined of the two natural existing faces, the prismatic  $\{100\}$  and pyramidal  $\{101\}$  faces. We found that the  $\{101\}$  faces are terminated by a layer of  $K^+$  ions and not by  $H_2PO_4^-$  groups, resolving a long-standing issue that could not be predicted by theory (chapter 5). From our measurements we cannot find clear differences between the surface structure in air, vacuum or in solution. However, the quality of the surface, also as function of time, is better controlled *in situ*.

It is known that when trivalent metal ion impurities like  $Fe^{3+}$  or  $Cr^{3+}$  are present in the growth solution the macroscopic crystal habit is elongated in the direction of the pyramidal faces. From the atomic structure of the two different faces in solution, we can explain this phenomenon. With only  $K^+$  ions on the  $\{101\}$  face of the crystal, impurity ions will experience a large barrier for adsorption onto the positively charged face. The  $\{100\}$  face has both the positive  $K^+$  ions and the negative  $H_2PO_4^-$  at the interface. On these faces cations can adsorb easily, and small amounts of these ions will already block the growth. When Fe impurities are added to the saturated KDP solution, no evidence was found for an ordered Fe layer on the prismatic face. However, the surface becomes significantly more rough. The impurities locally pin the moving steps, which causes an increased meandering of the steps leading to a rougher surface.

## Samenvatting

Dit proefschrift heeft als titel '*grenslaag structuur van groeiende kristallen*'. In deze samenvatting zal ik aan niet-specialisten proberen uit te leggen waar het over gaat.

### **Kristalgroei**

De interesse voor kristallen bestaat al sinds mensenheugenis en wordt gevoed door het bestaan van prachtige natuurkristallen zoals diamanten en andere edelstenen. In de natuur komen stoffen in verschillende toestanden voor. In een vloeistof of gas nemen de kleinste deeltjes, de atomen of moleculen, willekeurige posities in. In deze ongeordende toestand bewegen de deeltjes kriskras door elkaar. In de meeste vaste stoffen zitten de deeltjes zeer dicht opeengepakt, typisch minder dan één-miljoenste millimeter van elkaar, vast in een rooster. Dit wordt de kristallijne toestand genoemd. Deze ordening kun je met het blote oog of met een gewone microscoop niet zien, omdat zichtbaar licht een golflengte heeft die ongeveer duizend maal groter is dan deze afstand. Toch ontstaan de regelmatige oppervlakken en scherpe hoeken in kristallen doordat de onzichtbare deeltjes zo regelmatig zijn gerangschikt.

Kristallen kunnen op veel verschillende manieren groeien. Diamanten ontstaan diep in de aarde bij een zeer hoge temperatuur en druk, terwijl sneeuw kristallen zo in de lucht uit water dat befrist ontstaan. Kristalgroei vanuit een oplossing is een belangrijk proces dat wordt gebruikt voor het maken van ontelbare vaste stoffen. Niet alleen bekende producten zoals suiker en zout, maar ook veel medicijnen worden op deze manier gemaakt. Het is al eeuwenlang bekend dat keukenzout gewonnen kan worden uit zeewater door het te laten verdampen. Er kan maar een beperkte hoeveelheid zout in water oplossen. Als de hoeveelheid water vermindert, raakt de oplossing oververzadigd en zullen er kristallen ontstaan. Een zoutmolecuul beweegt eerst kriskras door de oplossing maar sluit zich dan aan op een regelmatige plek in het groeiende zoutkristal. Ook met de temperatuur van de oplossing verandert de hoeveelheid zout die opgelost kan worden. Een mooi voorbeeld hiervan is de Dode Zee in Israël die helemaal met zout verzadigd is. In de winter ontstaan spontaan zoutkristallen doordat bij lagere temperatuur minder zout in het

## SAMENVATTING

water opgelost kan worden en de zee dus oververzadigd raakt. In de zomer lossen deze kristallen vervolgens weer op.

Kristallisatie is tegenwoordig ook van groot technologisch belang. Een heel belangrijk voorbeeld is het groeien van silicium dat wordt gebruikt als basismateriaal in computerchips. De vorm en zuiverheid van stoffen hangt sterk af van het kristallisatieproces. Dit is vooral ook belangrijk bij de productie van medicijnen.

In dit proefschrift richt het onderzoek zich op de onderlinge samenhang van de atomen — de atomaire structuur — van de grenslaag tussen het kristal en de omgeving waaruit het kristal groeit. Aan deze grenslaag vindt de eigenlijke groei plaats. Doordat aan het oppervlak van het kristal de atomen niet aan alle kanten omringd zijn door andere atomen zoals in de lagen dieper in het kristal (de *bulk* van het kristal), kunnen de fysische eigenschappen van het oppervlak anders zijn. De eenvoudigste verandering in structuur is *relaxatie*, waarbij de afstand tussen de eerste paar atoomlagen aan het oppervlak groter (of kleiner) is dan de corresponderende afstand in de bulk. Een grotere verstoring treedt op wanneer de oppervlakte-atomen zich herschikken in een regelmaat die anders is dan die van de bulk. Dit wordt *reconstructie* genoemd. Een reconstructie verandert alle structuurgevoelige eigenschappen van het oppervlak zoals de atoomvibraties, het chemisch, optisch, en elektrisch gedrag. Het is interessant om naar reconstructies te kijken omdat aan oppervlakken veel verschillende processen optreden die van groot fundamenteel en technologisch belang zijn, niet alleen voor kristalgroei, maar ook bijvoorbeeld voor chemische reacties, katalyse en elektrische processen in halfgeleiderovergangen. Hieronder wordt een methode beschreven waarmee we de structuur van het oppervlak kunnen ontrafelen.

### **Röntgenverstrooiing**

Ruim honderd jaar geleden ontdekte Wilhelm Röntgen onzichtbare stralen die dwars door lucht, hout en zelfs de hand van zijn vrouw heen gingen. Dit laatste was tevens de eerste medische toepassing van deze röntgenstraling. Iets later bleek ook dat met behulp van röntgenstraling de structuur van de materie op de allerkleinste schaal, die van de atomen en moleculen, kon worden blootgelegd. Röntgenstraling behoort, net als zichtbaar licht, tot het spectrum van elektromagnetische straling. Elektromagnetische straling plant zich voort in golven. Het enige verschil tussen de verschillende soorten elektromagnetische straling is de lengte van de golven. De golflengte van röntgenstraling is duizend keer kleiner dan die van zichtbaar licht en bedraagt slechts ongeveer één tien-miljoenste millimeter.

Als een röntgenbundel op een kristal wordt gericht, ontstaat een regelmatig patroon van uitkomende röntgenstralen. Dit patroon ontstaat doordat de röntgen-

## SAMENVATTING

golven door de atomen in het kristal verstrooid worden. In bepaalde richtingen vallen de posities van alle verstrooide pieken van de golven precies samen, waardoor ze elkaar versterken. Uit dit patroon kan de ordening en de afstand tussen de atomen bepaald worden. In de afgelopen eeuw is de bulkstructuur van veel kristallen al heel nauwkeurig bepaald. Wij willen echter de atomaire structuur aan het oppervlak van het kristal met deze methode bepalen. Het doordringende vermogen van röntgenstralen is zeer nuttig bij het bestuderen van kristalgroei uit de oplossing, omdat we de grenslaag tussen een vloeistof en een vaste stof kunnen bestuderen. De röntgenstraling kan door de vloeistof heendringen en bovendien informatie opleveren op de atomaire schaal. Echter, doordat het laagje waarin we geïnteresseerd zijn slechts een dikte heeft van ongeveer één-miljoenste millimeter, is het signaal vanuit dit laagje uiterst zwak. Het veel sterkere signaal van het hele kristal is gelukkig alleen aanwezig in zeer specifieke richtingen van invallende hoek en uitgaande hoek van de röntgenstralen. In andere richtingen zijn er nog genoeg mogelijkheden het signaal te detecteren dat alleen van de buitenste laag afkomstig is. Het signaal is echter zo zwak dat het alleen zichtbaar kan worden gemaakt met een extreem felle röntgenlamp.

Oppervlakteröntgenverstrooiing is daarom nog een vrij recente techniek voor structuuronderzoek, omdat deze pas goed mogelijk werd met de komst van zogenaamde *synchrotron*röntgenbronnen zo'n 15 jaar geleden. Een van de grootste en nieuwste synchrotrons van de wereld is de Europese synchrotronstralingsfaciliteit ESRF ('European Synchrotron Radiation Facility') in Grenoble, aan de voet van de Franse Alpen. In het synchrotron wordt een minuscule bundel geladen deeltjes, elektronen, rondgeslingerd in een cirkelvormige, luchtledige buis met een omtrek van 850 meter. De snelheid waarmee de elektronen bewegen is gigantisch; elke seconde maken ze zo'n 350.000 rondjes. Op tientallen plaatsen rondom de ring staan magneten die de rondrazende elektronen in hun baan houden. Overal waar de elektronen worden afgebogen wordt extreem heldere röntgenstraling opgewekt.

### **Het proefschrift**

Dit proefschrift beschrijft röntgenverstrooiingsexperimenten waarin de structuur van het grensvlak van kristallen wordt bepaald om begrip te krijgen van het kristalgroeiproces op atomaire schaal. Het eerste gedeelte behandelt kristallen en hun groei in vacuüm. Deze experimenten zijn uitgevoerd bij het synchrotron in Daresbury, in Engeland. Het kristaloppervlak moet hier geprepareerd worden in vacuüm, omdat het anders vervuilt. De vacuümpstelling met het kristal erin wordt neergezet aan het eind van een pijp waar röntgenstralen uitkomen. De röntgenbundel schijnt door een 'venster' gemaakt van beryllium de opstelling binnen en belicht zo het



## SAMENVATTING

oppervlak van het kristal. Uit het patroon van de verstrooide röntgengolven kunnen wij de afstanden tussen de atomen aan het oppervlak berekenen.

Van de groei van een zilverkristal in een vacuümomgeving is een interessant verschijnsel bekend. Het kristal groeit hier met behulp van een methode die moleculaire bundelepitaxie heet. Vanuit een heet ‘oventje’ verdampt zilver dat neerslaat op een al bestaand schoon kristal. Deze depositie blijkt te resulteren in een groei waarbij het oppervlak steeds ruwer wordt. Door het oppervlak eerst opzettelijk ‘vies’ te maken door er een heel klein beetje antimoon op te dampen (uit een ander oventje) gaat het zilver daarna plotseling netjes atoomlaag voor atoomlaag groeien en blijft het oppervlak dus glad.

Uit de experimenten beschreven in hoofdstuk 2 en hoofdstuk 3 van dit proefschrift blijkt nu dat de *evenwichtsstructuur* (wanneer geen groei plaatsvindt) van het oppervlak afhangt van de hoeveelheid antimoon die zich aan het oppervlak bevindt. Als we naar de atoomlagen in het kristal parallel aan het oppervlak kijken, kunnen we drie verschillende laagjes onderscheiden, die we voor het gemak A, B en C noemen. Als we moeten aangeven hoe het kristal er uit ziet in deze laagjes, kunnen we dat dus aangeven met ABCABC...etc. Het blijkt dat wanneer we nu zilver laten groeien er soms zogenaamde ‘stapelfouten’ optreden, waarbij het kristal verder groeit met het ‘verkeerde’ laagje: ABCABCb! De evenwichtsstructuur heeft deze fouten echter niet, ook niet wanneer een heel klein beetje antimoon wordt toegevoegd. Maar wanneer de hoeveelheid antimoon in de bovenste laag nu zo is, dat er voor elke twee zilver atomen één antimoon atoom aanwezig is, verandert de structuur opeens en ontstaat er een reconstructie waarbij alle atomen in de buitenste laag verkeerd gestapeld zijn. We hebben ook de relaxaties van deze reconstructie bepaald, en we weten nu de exacte posities van de atomen aan een dergelijk oppervlak.

Wanneer nu bij een temperatuur van 100 graden Celsius meer zilver op dit oppervlak wordt gedampt, ‘zwemt’ het antimoon naar boven en keren de zilberatomen terug naar de juiste stapeling. Na één gegroeide laag hebben we dus ABCABCb, maar na twee lagen hebben we ABCABCac. De ‘b-laag’ is veranderd in een correcte ‘a-laag’, maar de bovenste laag heeft weer de verkeerde stapeling (in dit geval ‘c’). Effectief hebben we dus tijdens groei een ‘drijvende’ stapelfout.

In hoofdstuk 4 hebben we een systeem bestudeerd dat kan worden gezien als een model voor een vaste stof in contact met een vloeistof; alleen bestaat de vloeistof hier maar uit één laag atomen. Het kristal dat we hier gebruikt hebben bestaat uit germanium, en daar hebben we een laag lood opgedampt met dezelfde techniek als hierboven beschreven. Bij lage temperatuur ontstaat er weer een reconstructie waarvan we de precieze structuur hebben bepaald. Wanneer nu het kristal verwarmd wordt tot boven 180 graden Celsius ‘smelt’ deze reconstructie. Het blijkt dat het

## SAMENVATTING

loodlaagje eigenschappen vertoont van een vloeistof, maar dat, door de strakke ordening van de germaniumatomen daaronder, er toch nog een zekere ordening in het lood blijft bestaan. Het lijkt er op dat de loodatomen heel hard vibreren en snel over het oppervlak bewegen, maar zich toch nog een significant deel van de tijd op vaste posities op het oppervlak bevinden. Deze posities hebben een voorkeur vanwege de atomaire structuur van het onderliggende germaniumkristal.

In de hoofdstukken vijf en zes worden röntgenverstrooiingsmetingen beschreven waarmee de oppervlaktestructuur van een kristal in een oplossing is bepaald. Röntgenverstrooiing is moeilijker toepasbaar als alleen de ordening van de zeer dunne grenslaag in een vloeistof wordt onderzocht. De röntgenbundel moet eerst door de vloeistof heendringen om het kristaloppervlak te bereiken. Tot voor kort was geen enkele röntgenbron fel genoeg om een dergelijk experiment te doen. De intense bundel die door de ESRF in Grenoble wordt opgewekt, heeft in deze situatie verandering gebracht. Het kristal dat voor deze metingen is gebruikt, is KDP (chemische formule  $\text{KH}_2\text{PO}_4$ , kalium-di-waterstof-fosfaat) en de gebruikte oplossing is water. KDP wordt veel gebruikt in lasertoepassingen en zeer grote kristallen (tot wel 40 bij 40 bij 100 cm!) van zeer hoge kwaliteit laat men daarvoor in laboratoria groeien. Bij het groeien van KDP-kristallen doet zich een verschijnsel voor dat ook bij veel andere systemen optreedt. De vorm van het kristal hangt namelijk sterk af van de zuiverheid van de groeioplossing. Is deze heel schoon, dan ontstaan min of meer vierkante kristallen. Bevat de oplossing onzuiverheden, dan worden de kristallen veel langwerpiger. Tijdens de groei ontstaan er twee verschillende groeivlakken, de zogenaamde prisma- en piramidevlakken (zie figuur 5.1(a) in hoofdstuk 5). Het is al lang bekend dat de prismavlakken niet meer groeien in aanwezigheid van uiterst kleine hoeveelheden verontreinigingen, zoals  $\text{Fe}^{3+}$  (ijzer). Vandaar dat de kristallen dan een langwerpige vorm krijgen. In zeer zuivere oplossingen groeien de verschillende vlakken ongeveer even snel, waardoor het kristal dus ongeveer vierkant wordt.

Hiervoor kan nu een verklaring gegeven worden. Met behulp van röntgenverstrooiing hebben wij de oppervlaktestructuur van de twee verschillende vlakken bepaald. Het blijkt dat bij de piramidevlakken de positieve  $\text{K}^+$ -ionen aan de buitenkant zitten, terwijl de prismavlakken zowel  $\text{K}^+$ -ionen als negatief geladen  $\text{H}_2\text{PO}_4^-$ -groepen aan de buitenkant hebben. Op deze vlakken hechten positief geladen verontreinigingen dus gemakkelijk en kunnen ze verdere groei blokkeren. Voor de piramidevlakken is dit veel moeilijker vanwege de positieve lading van het oppervlak (positieve ladingen stoten elkaar immers af). Vandaar dat deze vlakken gewoon doorgroeien, zelfs als de oplossing een beetje verontreinigd is. Uit de structuur op het allerkleinste niveau, dat van losse atomen, kunnen we dus begrijpen hoe de vorm van een groot gegroeid kristal eruit komt te zien!



## Dank

Bedankt Elias Vlieg, Friso van der Veen, Willem Jan Huisman, Erik van der Vegt, Martin Lohmeier, Jan ter Beek, Richard Loos, Johan Derks, Hans Zeijlemaker, René Koper, Herman Ficke, Illiya Cerjak, Joop van Dorsselaer, Dick Glastra van Loon, Henk Sodenkamp, Ed Kruller, Jan van Elst, Paul van Deenen, Henk Dekker, Ben Okhuysen, Dennis Driessen, Wim Barsingerhorn, Wim Brouwer, Jan van der Linden, Henk Neerings, Ruud Boddenberg, Christiaan Pen, Aart Kleyn, Jan Commandeur, Jan van der Elsken, Joost Frenken, Daan Frenkel, Wim de Jeu, Michael Gleeson, Marileen Dogterom, Piet Bennema, Willem van Enckevort, Jim De Yoreo, Robert Feidenhans'l, Andreas Stierle, Detlef Smilgies, Wim Bras, Ian Robinson, Salvador Ferrer, Jesus Alvarez, Peter Goedtkindt, Steve Bennett, Paul Steadman, Tracy Turner, Mark James, Chris Nicklin, Marc Langelaar, Mark Klik, Mischa Hoogeman, Peter Zagwijn, Alfons Molenbroek, Michel Zwanenburg, Bart Berenbak, Stefania Acco, Frans Giskes, Martin Jak, Marcel Janson, Jacob Hoogenboom, Kobus Kuipers, Marcel Lankhuizen, Liesbeth Mol, Joost Peters, Hélène van Pinxteren, Marcel Rost, Gerard van Rooij, Paul Schuddeboom, Rutger Schlatmann, Rutger Vrijen, Coert Oosterom, Ellen Mettes, Guda van der Lee, Hans Renssen, Preeti Gholap, Robert Engels, Jan, Jenny, Coen en Bas!



## **Curriculum Vitae**

Op 28 augustus 1970 ben ik geboren in Hoorn. Na het behalen van het VWO-diploma aan de scholengemeenschap Werenfridus aldaar in 1988, begon ik mijn studie natuurkunde aan de Universiteit van Amsterdam. In oktober 1989 legde ik het propaedeutisch examen af. In de doctoraalfase heb ik gedurende een jaar een afstudeeronderzoek gedaan in de groep synchrotronstraling van het FOM-Instituut voor Atoom- en Molecuulfysica (AMOLF) in Amsterdam. Onder begeleiding van Martin Lohmeier en Dr. E. Vlieg heb ik onderzoek gedaan aan de structuur van Ge(100) oppervlakken met behulp van röntgenverstrooiing. In mei 1993 behaalde ik het doctoraalexamen experimentele natuurkunde bij Prof. dr. A.W. Kleyn.

Daarna heb ik mijn doctoraalstudie Filosofie en Artificiële Intelligentie, waaraan ik in september 1990 aan de Universiteit van Amsterdam was begonnen, afgemaakt. Mijn afstudeerscriptie heb ik geschreven onder begeleiding van Prof. dr. R.I. Bartsch. Het onderwerp was het probleem van intentionaliteit zoals dat behandeld wordt in de traditionele cognitieve wetenschap en in het connectionisme. Het doctoraalexamen heb ik behaald in augustus 1994.

In september van datzelfde jaar ben ik als onderzoeker in opleiding (OIO) in dienst getreden bij de stichting voor Fundamenteel Onderzoek der Materie (FOM). Op AMOLF heb ik onder begeleiding van Prof. dr. E. Vlieg met behulp van röntgenverstrooiing ordeningsverschijnselen bestudeerd aan grensvlakken van groeiende kristallen. In totaal werd gedurende 9 maanden onderzoek verricht in verscheidene onderzoekscentra in Europa (HASYLAB, Hamburg, Duitsland; Synchrotron Radiation Source, Daresbury, Engeland; European Synchrotron Radiation Facility, Grenoble, Frankrijk). De resultaten van het onderzoek hebben tot dit proefschrift geleid.